

Cy.Z

APR 1 1977
JUN 3 1977
JUN 22 1982



LASER VELOCIMETER MEASUREMENTS IN MODERATELY HEATED JET FLOWS

ENGINE TEST FACILITY
ARNOLD ENGINEERING DEVELOPMENT CENTER
AIR FORCE SYSTEMS COMMAND
ARNOLD AIR FORCE STATION, TENNESSEE 37389

April 1977

Final Report for Period July 1975 — June 1976

Approved for public release; distribution unlimited.

Property of U. S. Air Force
AEDC TR-76-156
F49600-76-8-0001

Prepared for

DIRECTORATE OF TECHNOLOGY (DY)
ARNOLD ENGINEERING DEVELOPMENT CENTER
ARNOLD AIR FORCE STATION, TENNESSEE 37389

NOTICES

When U. S. Government drawings specifications, or other data are used for any purpose other than a definitely related Government procurement operation, the Government thereby incurs no responsibility nor any obligation whatsoever, and the fact that the Government may have formulated, furnished, or in any way supplied the said drawings, specifications, or other data, is not to be regarded by implication or otherwise, or in any manner licensing the holder or any other person or corporation, or conveying any rights or permission to manufacture, use, or sell any patented invention that may in any way be related thereto.

Qualified users may obtain copies of this report from the Defense Documentation Center.

References to named commercial products in this report are not to be considered in any sense as an endorsement of the product by the United States Air Force or the Government.

This report has been reviewed by the Information Office (OI) and is releasable to the National Technical Information Service (NTIS). At NTIS, it will be available to the general public, including foreign nations.

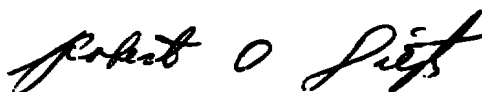
APPROVAL STATEMENT

This technical report has been reviewed and is approved for publication.

FOR THE COMMANDER



MARSHALL K. KINGERY
Research & Development
Division
Directorate of Technology



ROBERT O. DIETZ
Director of Technology

UNCLASSIFIED

REPORT DOCUMENTATION PAGE		READ INSTRUCTIONS BEFORE COMPLETING FORM
1 REPORT NUMBER AEDC-TR-76-156	2 GOVT ACCESSION NO.	3 RECIPIENT'S CATALOG NUMBER
4 TITLE (and Subtitle) LASER VELOCIMETER MEASUREMENTS IN MODERATELY HEATED JET FLOWS	5 TYPE OF REPORT & PERIOD COVERED Final Report - July 1975 June 1976	
	6 PERFORMING ORG REPORT NUMBER	
7 AUTHOR(s) D. O. Barnett and T. V. Giel, Jr. ARO, Inc.	8 CONTRACT OR GRANT NUMBER(s)	
9 PERFORMING ORGANIZATION NAME AND ADDRESS Arnold Engineering Development Center (DY) Air Force Systems Command Arnold Air Force Station, Tennessee 37389	10 PROGRAM ELEMENT, PROJECT, TASK AREA & WORK UNIT NUMBERS Program Element 65807F	
11 CONTROLLING OFFICE NAME AND ADDRESS Arnold Engineering Development Center (DYFS) Arnold Air Force Station Tennessee 37389	12 REPORT DATE April 1977	
	13 NUMBER OF PAGES 105	
14 MONITORING AGENCY NAME & ADDRESS (if different from Controlling Office)	15 SECURITY CLASS. (of this report) UNCLASSIFIED	
	15a DECLASSIFICATION/DOWNGRADING SCHEDULE N/A	
16 DISTRIBUTION STATEMENT (of this Report) Approved for public release; distribution unlimited.		
17. DISTRIBUTION STATEMENT (of the abstract entered in Block 20, if different from Report)		
18 SUPPLEMENTARY NOTES Available in DDC		
19 KEY WORDS (Continue on reverse side if necessary and identify by block number) laser velocimeters velocity measurements jets turbulence effects particle dynamics		
20. ABSTRACT (Continue on reverse side if necessary and identify by block number) Laser velocimeter (LV) measurements are presented for the developing velocity field of a subsonic jet and an underexpanded jet into quiescent air at nominal stagnation temperatures of 500 and 1,000°R. For the subsonic jet, the mean axial and radial veloci- ties; axial, radial, and tangential turbulence intensities; Reynolds stresses; and velocity probability distributions are presented for axial locations up to 20 nozzle diameters downstream of the nozzle		

UNCLASSIFIED

UNCLASSIFIED

20. ABSTRACT (Continued)

exit. Severe particle lag effects were encountered in the under-expanded jet so that data presentation is limited to the center-line mean axial velocity and probability distributions for exit-to-ambient static pressure ratios of 2 and 4 at axial stations up to 5 nozzle diameters downstream of the nozzle exit. Data were obtained with a two-component, Bragg-diffracted, individual realization system operated in a backscatter mode. Since the flow was unseeded, the measurements relied on naturally occurring flow contaminants to serve as scatter centers for the LV. Particle dynamics calculations for the two flows are used in conjunction with an analysis of the detection characteristics of the system to develop a theoretical limit for the minimum level of turbulence detectable by an LV.

UNCLASSIFIED

PREFACE

The work reported herein was conducted by Headquarters, Arnold Engineering Development Center (AEDC), Air Force Systems Command (AFSC), under Program Element 65807F. The results were obtained by ARO, Inc., AEDC Division (a Sverdrup Corporation Company), operating contractor for AEDC, AFSC, Arnold Air Force Station, Tennessee. The work was done under ARO Project No. R32S. The authors of this report were D. O. Barnett and T. V. Giel, Jr., ARO, Inc. The manuscript (ARO Control No. ARO-ETF-TR-76-119) was submitted for publication on October 12, 1976.

Appreciation and acknowledgment is extended to Dr. Barclay Jones, Nuclear Engineering Laboratory, University of Illinois, who served as a consultant on the particle dynamics computations, and Mr. B. W. Bomar for his help in analyzing the accuracy of the Model 8 Data Processors.

CONTENTS

	<u>Page</u>
1.0 INTRODUCTION	7
1.1 Background	7
1.2 Scope of the Investigation	8
2.0 EXPERIMENTAL APPARATUS AND PROCEDURE	8
2.1 Jet Test Installation	8
2.2 Laser Velocimeter System	10
2.3 LV Data Acquisition System	13
2.4 Supporting Instrumentation	14
2.5 Instrumentation Uncertainty	14
2.6 Test Procedures	16
2.7 Data Reduction Techniques	17
3.0 PARTICLE DYNAMIC LIMITATIONS ON TURBULENCE MEASUREMENTS	22
3.1 Particle Dynamics Relations	22
3.2 Probability Distribution Functions	25
3.3 Minimum Turbulence Levels	33
3.4 Seeding Nonuniformities	35
4.0 SUBSONIC JET RESULTS	39
4.1 Centerline Variation of Flow Parameters	39
4.2 Mean Velocity Measurements	44
4.3 Turbulence Intensity Measurements	51
4.4 Shear Stress	54
4.5 Velocity Probability Histograms	69
5.0 UNDEREXPANDED JET RESULTS	73
5.1 Mean Axial Velocity	73
5.2 Velocity Probability Distributions	77
6.0 CONCLUSIONS	84
REFERENCES	86

ILLUSTRATIONS

Figure

1. Test Nozzle Contour	9
2. Laser Velocimeter System	11
3. Signal Separation Electronics and Data Multiplexer	13
4. Effect of Particle Density on Velocity Lag in the Subsonic Jet	23
5. Effect of Particle Diameter on Velocity Lag in the Underexpanded Jet	24

<u>Figure</u>	<u>Page</u>
6. Influence of Particle Size on LV Detection Probabilities	29
7. Distribution of Particle Sizes in the Air Supply	31
8. Effect of Trigger Level on the Joint Probability Distribution	32
9. Particle Density Distribution Functions	32
10. Velocity Probability Distribution in the Near Field of the Subsonic Jet	33
11. Velocity Probability Distributions in the Near Field of the Underexpanded Jet	34
12. Effect of Seeding Nonuniformity on Mean and RMS Velocity Measurements	38
13. Pitot Measurements of Centerline Velocity Decay	39
14. LV Measurements of Centerline Velocity Decay	40
15. Centerline Axial Turbulence Intensity Distribution in Unheated Jet	42
16. Centerline Axial Turbulence Intensity Distribution in Heated Jet	42
17. Centerline Radial Turbulence Intensity Distribution in Unheated Jet	43
18. Centerline Radial Turbulence Intensity Distribution in Heated Jet	43
19. Axial Velocity Distributions at $X/D = 2$	45
20. Axial Velocity Distributions at $X/D = 5$	46
21. Axial Velocity Distributions at $X/D = 10$	47
22. Axial Velocity Distributions at $X/D = 20$	48
23. Radial Velocity Distribution in the Unheated Jet at $X/D = 2$	49
24. Radial Velocity Distribution in the Unheated Jet at $X/D = 5$	50
25. Radial Velocity Distribution in the Unheated Jet at $X/D = 10$	50
26. Radial Velocity Distribution in the Unheated Jet at $X/D = 20$	51
27. Axial Intensity Distributions at $X/D = 2$	52
28. Axial Intensity Distributions at $X/D = 5$	53
29. Axial Intensity Distributions at $X/D = 10$	55
30. Axial Intensity Distributions at $X/D = 20$	56
31. Radial Intensity Distributions at $X/D = 2$	57
32. Radial Intensity Distributions at $X/D = 5$	58
33. Radial Intensity Distributions at $X/D = 10$	59
34. Radial Intensity Distributions at $X/D = 20$	60
35. Tangential Intensity Distributions at $X/D = 2$ (Unheated)	61
36. Tangential Intensity Distributions at $X/D = 5$	62
37. Tangential Intensity Distributions at $X/D = 10$	63
38. Tangential Intensity Distributions at $X/D = 20$	64
39. Shear Stress Distribution at $X/D = 2$ (Unheated)	65

<u>Figure</u>	<u>Page</u>
40. Shear Stress Distributions at $X/D = 5$	66
41. Shear Stress Distributions at $X/D = 10$	67
42. Shear Stress Distributions at $X/D = 20$	68
43. Velocity Probability Distributions at $X/D = 2$ (Axial Component)	69
44. Velocity Probability Distributions at $X/D = 2$ (Vertical Components)	70
45. Shadowgraph of Underexpanded Jet, $P_e/P_\infty = 2$	71
46. Shadowgraph of Underexpanded Jet, $P_e/P_\infty = 4$	72
47. Centerline Axial Velocity Variation, $P_e/P_\infty = 2$	74
48. Centerline Axial Velocity Variation, $P_e/P_\infty = 4$	75
49. Velocity Histograms in the Unheated Flow, $P_e/P_\infty = 2$	78
50. Velocity Histograms in the Heated Flow, $P_e/P_\infty = 2$	79
51. Velocity Histograms in the Unheated Flow, $P_e/P_\infty = 4$	80
52. Velocity Histograms in the Heated Flow, $P_e/P_\infty = 4$	81

TABLES

1. Test Parameters	10
2. Uncertainty in Pitot Velocity Measurements	16
3. Relations for the Evaluation of Simultaneously Acquired Data	19
4. Mach Disc Locations	72

APPENDIXES

A. LIMITS ON THE ACCURACY OF THE MODEL 8 DATA PROCESSOR	90
B. MULTIPLE PARTICLE SIGNAL ANALYSIS	99
NOMENCLATURE	102

1.0 INTRODUCTION

Detailed knowledge of the spatial and temporal variation of velocity in the various components of aerospace propulsion systems would lead to increased understanding of the operational characteristics of such units. The often complex geometries, chemical reactions, high temperatures, velocities, and turbulence levels encountered in typical systems, however, preclude the accurate determination of flow characteristics by analytical methods. Clearly, there exists a need for instrumentation capable of measuring mean and fluctuating velocities in propulsive flows.

Conventional instruments such as hot-wire anemometers or pitot probes are not capable of fulfilling this need since they are subject to damage by impact or thermal loadings, induce local flow disturbances, and are inaccurate in many types of flows characteristic of propulsion systems (Ref. 1). During the past decade, however, it has become increasingly apparent that optical velocity measuring devices such as the laser velocimeter (LV) avoid the above mechanical limitations and can, under controlled circumstances, obtain the requisite data with reasonable accuracy (Refs. 2 through 5).

1.1 BACKGROUND

An LV measures fluid velocities indirectly by determining the velocity of particles contained in the fluid medium. If the particles are small (and/or of low density) accurate measurements of gas velocity are obtained. Since particle dynamic effects may seriously compromise the accuracy of LV measurements, many investigators have relied on seeding gas flows with particles of a small enough size that particle lag effects are unimportant. For many potential LV applications, however, it is not feasible or desirable to seed a flow since the introduction of foreign matter into the fluid system may result in damage to its components or compromise other test objectives. Because of this constraint, which is typical of many test activities at AEDC, efforts have been underway to develop equipment, test methodology, and data interpretation techniques that will allow accurate LV measurement of gas velocities by employing naturally occurring particulates and aerosols as the seed material.

The development of interference (or fringe) LV optical systems (Refs. 6 and 7) and burst data processors (Refs. 8 and 9) made the realization of individual particle velocities possible so that LV utilization at low seed concentration was feasible. Operation of such individual realization velocimeters in highly turbulent or recirculating flows became possible with the introduction of ultrasonic diffraction (Bragg) cells to impart a frequency shift to the input beams (Ref. 10). Bragg-diffracted, individual realization LV's, moreover, have distinct advantages for high-speed flows since the fringe system associated with a given optical arrangement may be given a motion opposite to that of the flow so that a particle traversing the probe volume crosses more fringes than in a conventional LV.

The use of a forward-scatter Bragg-diffracted LV to measure a subsonic isothermal jet flow field is described in Refs. 11 and 12. It was found that, in addition to particle lag effects, errors may be introduced in the results by electronic noise, improper setting of trigger levels, or misalignment of the fringe system with the flow axes. When these factors were properly controlled, measurements of mean velocity and turbulence levels were obtained that are comparable in accuracy to hot-wire results. It was shown, moreover, that concurrent measurement of shear stress and turbulence intensity was possible if both the axial and radial velocities of the ensemble of particles were measured simultaneously.

1.2 SCOPE OF THE INVESTIGATION

Several problems of importance in application of laser velocimeters to propulsion system flows were not addressed in Refs. 11 and 12. These included operation of the LV system in a back-scatter mode in a flow having elevated temperatures and velocities comparable to those found in engine exhaust flows.

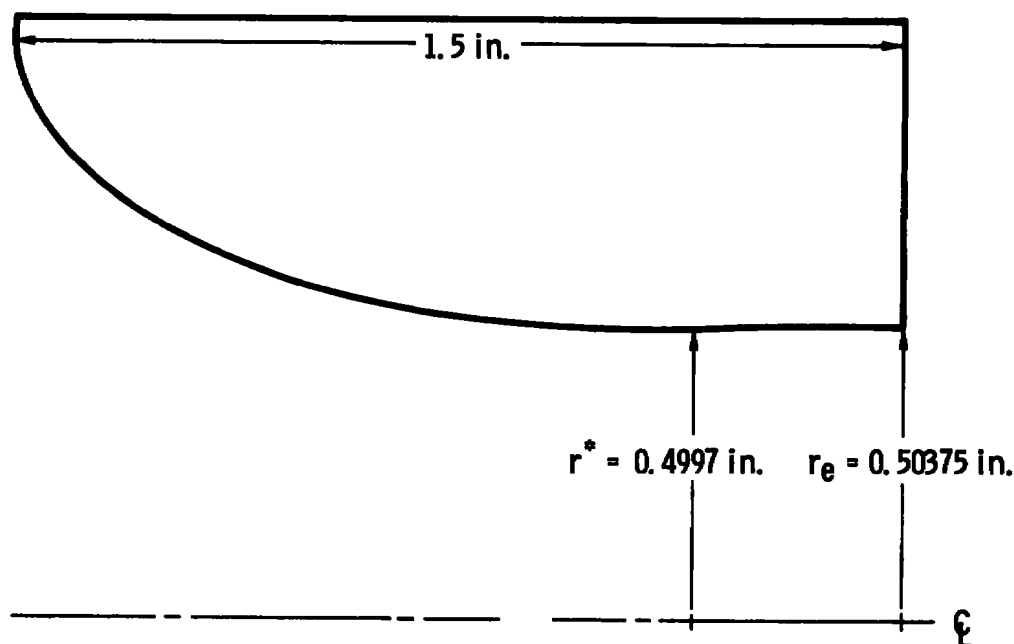
The present study was performed to further test the suitability of laser velocimetry for making detailed measurements of the velocity field in flows having turbulence structures similar to those found in propulsion system exhausts. Specifically, a Bragg-diffracted, individual realization LV was used in a back-scatter mode to determine the mean velocity and turbulence characteristics of a subsonic and an underexpanded jet exhausting into still air. Measurements were made at both ambient and elevated jet temperatures to determine LV performance with flows having stagnation temperatures approaching 1,000°R. For the underexpanded jet tests, the two-component LV was modified to allow its operation as a one-component unit capable of measuring velocities up to 3,500 ft/sec. The LV measurements are presented for axial locations up to 30 nozzle diameters downstream of the exit plane of the subsonic jet. The data consist of the mean axial and radial velocities, turbulence intensities, shear stress, and velocity probability distribution. These data are compared to mean axial velocities obtained from Pitot pressure measurements and, where available, published hot-wire data. Centerline axial velocities and probability distributions are presented for the underexpanded jet operating at exit-to-ambient static pressure ratios of 2.0 and 4.0 for axial stations up to 5 nozzle diameters downstream of the nozzle exit plane. The data are also compared to velocities derived from Pitot pressure results and theoretical calculations of the flow field.

2.0 EXPERIMENTAL APPARATUS AND PROCEDURE

2.1 JET TEST INSTALLATION

Tests were conducted using a free-jet test installation located in Propulsion Research Cell (R-1A-1) of the Engine Test Facility. The air jet emerged from an axisymmetric,

1-in. diam nozzle. The nozzle, illustrated in Fig. 1, was designed to have an elliptical, converging contour, but because of machining inaccuracies, the nozzle actually diverged slightly having an exit-to-throat area ratio (A/A^*) of 1.016.



Nozzle Measurements - Diverging Section

<u>Axial Location, in. from Throat</u>	<u>Radial Measurement, in.</u>
0	0.49970
0.05	0.49985
0.10	0.50055
0.15	0.50140
0.20	0.50205
0.25	0.50210
0.30	0.50210
0.35	0.50375

Figure 1. Test nozzle contour.

Measurements were made in a subsonic jet having a nominal exit velocity of 400 ft/sec and in underexpanded jets having nozzle exit-to-ambient pressure ratios (P_e/P_∞) of 2, 3, 4, and 5. Data were obtained in both heated and unheated flows. In the former case, an indirect-fired propane heater capable of delivering up to 5 lbm/sec of heated air at 150 psig and 1,000°R was used.

A summary of the nominal values of the test parameters is given in Table 1.

Table 1. Test Parameters

Flow	T_o , °R	$Re_D^a \times 10^{-5}$	M_e^b
1. Cold Subsonic	490	2.5	0.37
2. Hot Subsonic	866	0.9	0.28
3. Cold Supersonic			
a. $P_e/P_\infty = 2$	490	16.6	1.145
b. $P_e/P_\infty = 4$	488	33.3	1.145
4. Hot Supersonic			
a. $P_e/P_\infty = 2$	1,000	6.8	1.145
b. $P_e/P_\infty = 4$	997	13.5	1.145

a. Based on nozzle exit diameter

b. Assuming one-dimensional isentropic flow from the geometric throat

2.2 LASER VELOCIMETER SYSTEM

Optical velocity measurements were made with the two-component, Bragg-diffracted laser velocimeter shown in Fig. 2. An argon-ion laser capable of producing an optical power of 2 watts in the 514.5-nm wavelength line was the light source. Radiation emanating from the laser is directed by mirrors to pass through a beam reducer onto a two-component Bragg cell, which ultrasonically diffracts the light into several beams. Each diffracted beam differs in frequency from the incident beam by an amount (nf_o) where $n = 0, 1, 2, \dots, k$ and f_o is the frequency of the crystal oscillator which produces standing ultrasonic waves in each leg of the cell. The two lower order beams for the horizontal and vertical diffraction orders are of nearly equal intensity and are allowed to pass through a collimating lens and a beam expander. The light is then redirected by two mirrors and focused to form two orthogonal sets of fringes in the probe volume.

Because of the frequency shifts imparted by the Bragg cell, a moving fringe system is established in the probe volume, and velocities are determined with respect to a reference velocity ($U^* = K_U f_o$) where, for example, K_U is the horizontal fringe spacing. Since the frequency of the signal to be processed is lower when the fringes move in the flow direction, a fringe travel inverter was used in the subsonic jet tests to improve the accuracy of the LV measurements. The inverter was removed in the supersonic tests so

that the fringe travel was in opposition to the flow direction. Although this required the processing of higher frequency signals, it helped to ensure that sufficient fringes were present to give a processable signal. For the optical system described, the nominal horizontal fringe spacing is $39\text{ }\mu\text{m}$, so that with $f_0 = 15\text{ MHz}$, the fringe reference velocity (U^*) was 1,800 ft/sec. The vertical fringe spacing was $13\text{ }\mu\text{m}$, and the driver frequency was 45 MHz.

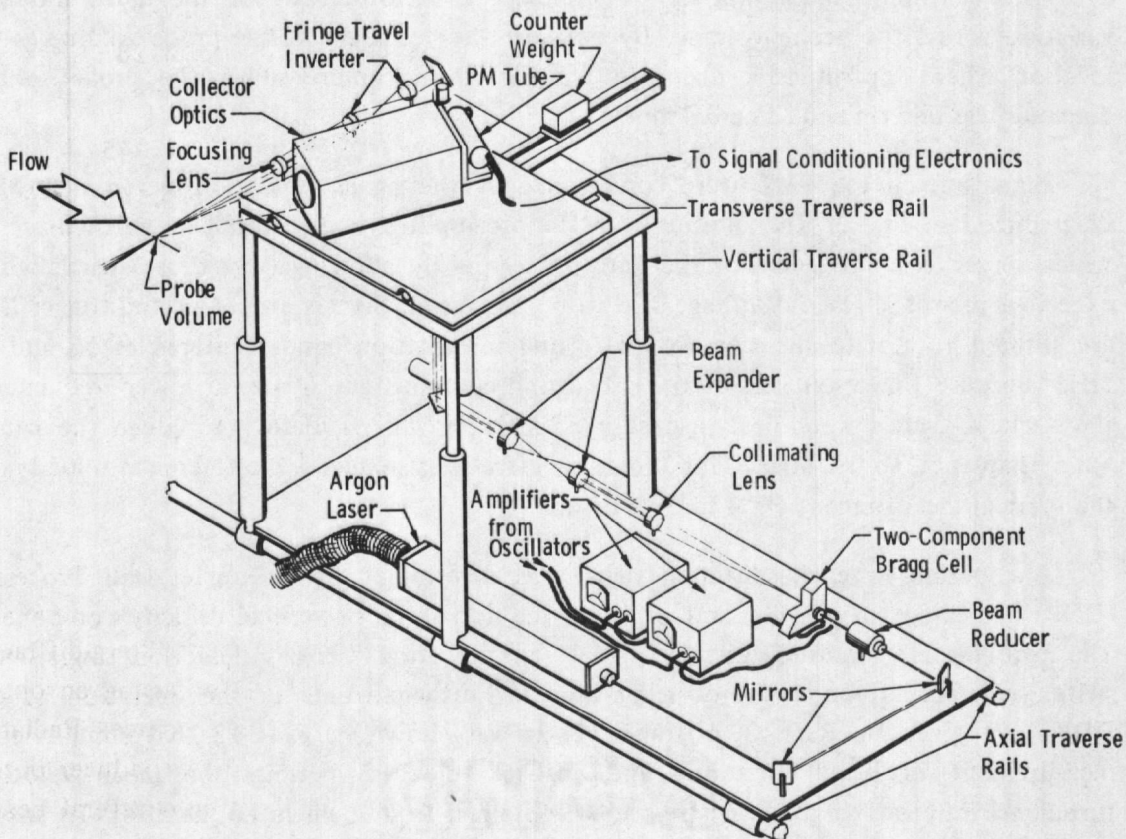


Figure 2. Laser velocimeter system.

The laser velocimeter was mounted on a traverse system which allowed movement of the probe volume along any of three mutually orthogonal axes. By traversing the flow along its vertical axis, the measured vertical velocity corresponds to the radial velocity (V) in the jet. In traverses of the jet along the horizontal flow axis, the vertical component corresponds to the tangential velocity (W) of the flow. In either case, the horizontal fringes provide the axial velocity component (U) so that, because of axisymmetry, traversing the jet in two directions allows the two-component system to provide information on all three components (U , V , W) of the velocity vector at any radial location. The geometrical considerations involved in using a two-component system in this fashion are discussed in Ref. 12.

Light scattered by a particle passing through the probe volume is collected by the collector optics and focused on a photomultiplier tube (PMT). By viewing the probe volume through a 500- μm circular aperture at an off-axis collection angle of 12.5 deg, the length of the LV probe volume in the laser propagation direction was less than 1.2 mm. The spatial resolution in the other directions was measured by traversing the probe volume with a glass encapsulated photo cell mounted behind a 100- μm -diam pin hole. This probe volume measuring device produces a measurement of the mean intensity variation across the probe volume. By defining the boundary of the probe volume as the location where the intensity drops to $1/e^2$ of its maximum values, the probe volume diameter was determined to be 0.3 mm.

Signals from the PMT were conditioned by the signal separation electronics (SSE) diagrammed in Fig. 3. The output from the preamplifier is monitored by an oscilloscope which serves as a "trigger" for the data processors by allowing only those signals which exceed a pre-set threshold voltage rise to be processed. Signals exceeding the trigger level are filtered to isolate the two Doppler burst information bands centered at 15 and 45 MHz. Because the resolution of the processing equipment is greater at lower frequencies, the vertical signals were beat against a 32-MHz crystal oscillator to reduce the center band frequency to 13 MHz. This provision effectively reduced the reference velocity for the vertical measurement (V^*) to 520 ft/sec.

The period of each separated signal was determined by a Doppler Data Processor (DDP) dedicated to measurement of either the horizontal or vertical velocity component. The processors feature variable signal amplification, error detection logic, and switch-selectable frequency processing ranges. Further details of the operation of the DDP's are given in Refs. 8, 10, and 12. It was shown in Ref. 12 that simultaneous measurement of both horizontal and vertical velocities permits the mean velocity, turbulence intensity, and shear stress to be obtained from a single LV data set. To ensure simultaneous data acquisition, a data multiplexer was used which suppressed the processing of further signals by either DDP until a pre-set time (generally 250 μsec) had elapsed. At the conclusion of this interval, data were recorded only if both processors had measured non-zero values of the signal period. If either processor had failed to process the Doppler burst frequency, the multiplexer reset both instruments to allow another sample to be taken.

For the above system, two components of velocity can be measured over an axial velocity range $-250 \leq U \leq 700$ ft/sec and a vertical velocity range $-250 \leq V \leq 250$ ft/sec. To extend the velocity range for the supersonic jet studies, the system was only operated as a one-component system. For high-speed operation, therefore, only one leg of the Bragg cell was driven (15 MHz), the fringe inverter was removed, and the signal separation electronics were bypassed. This configuration allowed the measurement of axial velocities over the range $-250 \leq U \leq 3,500$ ft/sec.

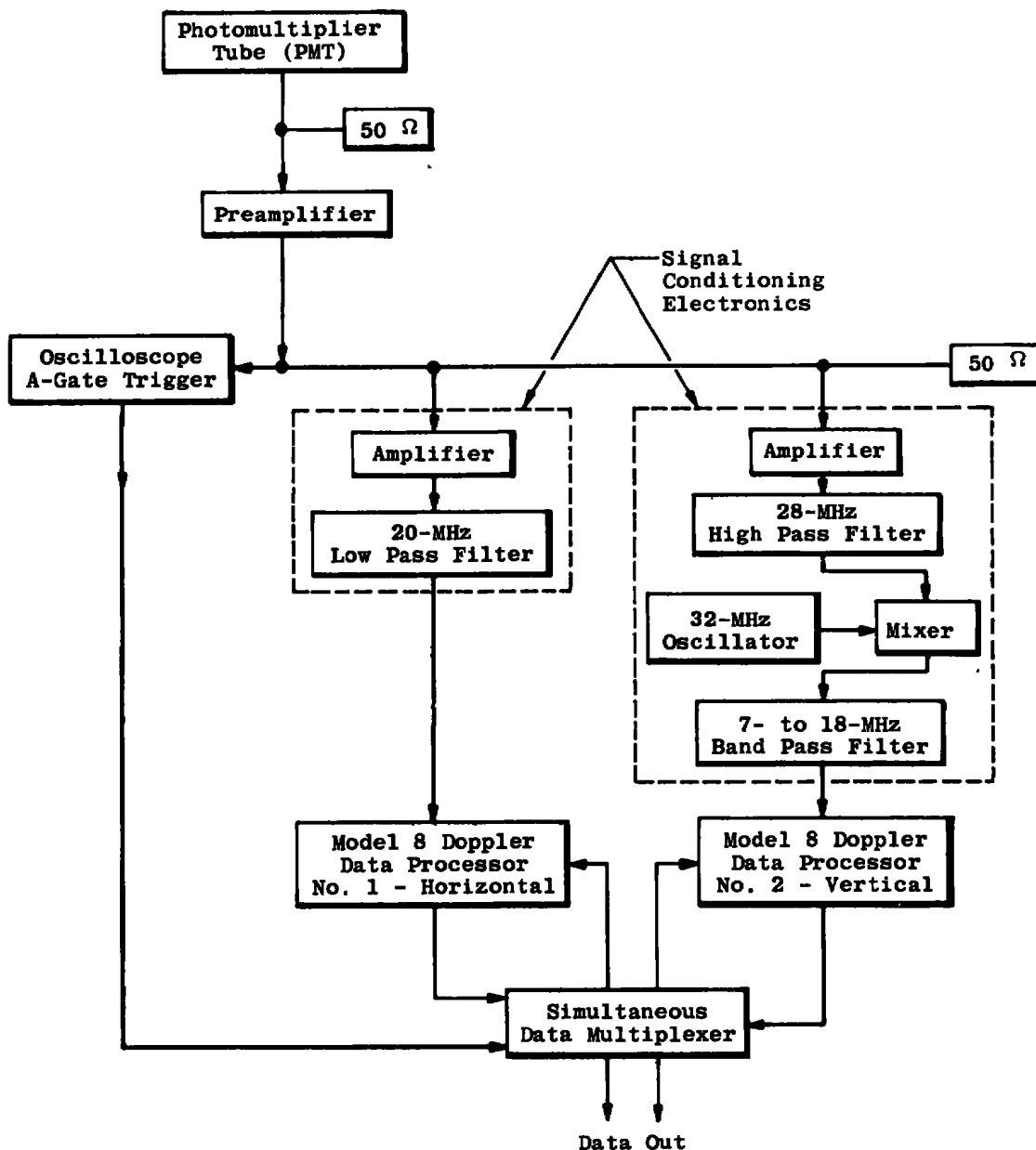


Figure 3. Signal separation electronics and data multiplexer.

2.3 LV DATA ACQUISITION SYSTEM

A high-speed minicomputer data acquisition system (DAS) was used to acquire data in the LV tests. This system had the ability to store over 1,000 simultaneous data samples

per second, which generally exceeded the observed data rates in the subsonic jet. The minicomputer, which functioned as both a logic control unit and a high-speed data buffer storage unit, was programmed to store data sets consisting of 500 LV measurements from each DDP. The first 50 samples from each data set were displayed on an alphanumeric display unit for instantaneous monitoring. Any number of data sets could be recorded at each flow-field location, but because of limits imposed by data acquisition and data reduction times, the total data matrix usually consisted of 1,500 samples.

2.4 SUPPORTING INSTRUMENTATION

In addition to the LV measurements, pressure and temperature data were taken in the stilling chamber and jet plumes. Chamber conditions were monitored with a static pressure orifice and a bare-wire thermocouple. A pitot pressure probe constructed from 0.25-cm-diam stainless steel tubing with a 0.16-cm inside diameter was mounted on a sting attached to the LV traverse system. Total temperature measurements were made by aspirated bare-wire thermocouples supported by a 0.05-cm-diam sheath suspended within the probe. All jet pressures were measured using strain-gage pressure transducers while temperature was determined by Chromel®-Alumel® thermocouples. Atmospheric pressures and temperatures were measured with a Bourdon-tube pressure gage and mercury thermometer, respectively. A parallel light shadowgraph system was used to obtain photographs of the shock structure in the underexpanded jet.

Probe pressure transducer, thermocouple, and position data were recorded with an X/Y plotter. The probe position relative to the jet centerline was evaluated at each axial station from the symmetry of the total pressure profiles. Stilling chamber and ambient pressures and temperatures were continuously monitored throughout the tests to ensure the constancy of the desired jet exit conditions.

2.5 INSTRUMENTATION UNCERTAINTY

The instrument uncertainty of a Bragg-diffracted laser velocimeter is dependent on the accuracy to which the fringe spacing can be determined, the stability of the crystal oscillator used to drive the Bragg-cell, and the precision to which the DDP can determine the signal period. From Refs. 11 and 12, the uncertainty in measuring an individual velocity realization (U_i) is

$$\Delta U_i = \alpha + \beta U_i + \gamma U_i^2 \quad (1)$$

The coefficients of Eq. (1) are given by

$$\alpha = K_t f^* \left(\frac{\Delta t^*}{t^*} + f^* \Delta \tau_i \right) \quad (2)$$

$$\beta = \frac{\Delta K_U}{K_U} - 2f^* \Delta \tau_i \quad (3)$$

$$\gamma = \frac{\Delta \tau_i}{K_U} \quad (4)$$

where K_U is the fringe spacing, f^* a reference frequency given by the difference of the Bragg cell driver frequency (f_0) and any oscillator used to downshift the signal, and τ_i the period of the Doppler burst.

From the repeatability of measurements of the fringe spacing in the present LV, it is estimated that the uncertainty in the fringe spacing ($\Delta K_U/K_U$) is ± 0.025 for the horizontal component measurements and ± 0.010 for the vertical. Tests of the stability of the crystal oscillators used in these experiments indicate that the errors in reference frequency ($\Delta f^*/f^*$) are $\pm 6.660 \times 10^{-4}$ and 7.69×10^{-4} for the horizontal and vertical measurements, respectively. A detailed study of DDP accuracy, outlined in Appendix A, showed that the processor used to measure axial velocities had an accuracy ($\Delta \tau_i$) of ± 0.005 ns, while the DDP used for vertical velocities was accurate to within ± 0.05 ns. For these values, the uncertainty in the axial velocity measurements varies from ± 1.3 ft/sec at $U_i = 0$ to ± 2.4 ft/sec at $U_i = 3,500$ ft/sec, while the vertical velocity measurement uncertainty ranges from ± 0.7 ft/sec at $V_i = 0$ to ± 3.7 ft/sec at $V_i = 250$ ft/sec.

In using an individual realization LV, it is attempted to reproduce the statistical behavior of a random variable (velocity) by a finite number of measurements. The results obtained for the mean or standard deviation of the velocity are, therefore, only approximations to the true value of these parameters. This conclusion holds even in the absence of instrument uncertainty. It is shown in Refs. 12 and 13 that the confidence interval for the mean velocity depends on the sample size and turbulence intensity while the confidence interval for the measured intensity depends, additionally, on the kurtosis of the velocity distribution. For a data set of 1,500 samples and a 95-percent confidence level, the confidence interval for the mean velocity in the subsonic jet was less than 5 percent in all cases, while the confidence interval for the turbulence intensity was 6.5 percent. Along the centerline of the underexpanded jet, these values are reduced to 0.25 and 2.5 percent, respectively, because of the low values of turbulence intensity.

Mean axial velocities were also obtained from the pressure and temperature measurements of the jet. The accuracy of the various instruments used in obtaining the measurements was estimated from comparisons to laboratory standard instrumentation. The instrument uncertainties were then used to determine the uncertainty in axial

velocities obtained from pitot traverses by the methods of Ref. 14. The results of the analysis are summarized in Table 2.

Table 2. Uncertainty in Pitot Velocity Measurements

Subsonic Jet				
Velocity, ft/sec	Cold Jet		Hot Jet	
	Uncertainty, ft/sec	Percent Uncertainty	Uncertainty, ft/sec	Percent Uncertainty
50	11.0	22.0	19.3	38.5
100	6.1	6.1	9.9	9.9
300	3.5	2.8	8.4	2.8
400	10.9	2.7	10.5	2.6
Supersonic Jet				
Mach Number	Cold Jet		Hot Jet	
	Jet Velocity, ft/sec	Percent Uncertainty	Jet Velocity, ft/sec	Percent Uncertainty
1.64	1,450	2.97	2,050	2.76
2.10	1,680	1.85	2,370	1.51
2.60	1,860	1.64	2,630	1.26
3.61	2,080	1.73	2,950	1.37

2.6 TEST PROCEDURES

Several hours prior to each test the LV equipment was turned on to allow it to stabilize, while the potentiometers, which indicate probe location relative to the nozzle centerline, and the supporting instrumentation were calibrated. Once the beam split from the Bragg cell had stabilized, the laser was adjusted to obtain maximum power in the 514.5-nm spectral line, and the Bragg drivers and Bragg cell were balanced to obtain equal beam intensities from the four unblocked beams.

After the adjustments were completed, the fringe spacing and orientation with respect to the jet axis were determined. For a Bragg-diffracted LV, this information is

determined from the geometry of the intersecting light beams since direct observation of the moving fringes is not feasible. A detailed discussion of this procedure is presented in Ref. 12. The LV pretest procedures were completed by focusing the collector optics to obtain the maximum Doppler signal amplitudes from a small calibration jet flowing across the probe volume.

Test operations were begun when the stilling chamber pressure and temperature stabilized at the values desired for a particular test. Preliminary pitot traverses were made at each axial station to determine the centerline of the jet and thus establish the origin of the jet coordinate system. When the centerline had been located, total pressures and temperatures were recorded for use in determining the mean axial velocity. Prior to the unheated runs, the probe was positioned so that the LV sensing volume was coincident with the tip of the pitot tube, thus giving a direct correspondence between the locations at which the two types of measurements were obtained. Since this alignment was performed in the jet, personnel safety considerations precluded its use in the underexpanded and heated jet tests. In those cases, the centerline was taken to be the geometrical centerline of the nozzle under non-flowing conditions.

Before each LV data point was taken, the laser power, photomultiplier tube voltage, and the trigger level could be adjusted. It was found that, for laser power in excess of 700 mw, the maximum signal amplitudes were essentially independent of the light intensity. However, data were generally taken with laser powers in the 1.0- to 1.5-w range in an effort to detect a larger fraction of smaller particles than would be possible at a lower illuminating intensity. The photomultiplier tube voltage was usually set at the manufacturer's specified value although other voltages were used occasionally in an effort to increase signal amplitudes or decrease system noise. The trigger was set at the lowest level that was consistent with the attainment of high data processing rates.

Upon completion of the above adjustments at each flow field position, LV data acquisition was initiated and continued until, nominally, 1,500 velocity samples were obtained to complete each data point. The data acquisition rate was found to be a function of location in the jet as well as flow velocity. Typically, a data point was obtained in 1 to 5 min in the subsonic jet tests and less than 1 min in the underexpanded jet.

2.7 DATA REDUCTION TECHNIQUES

The LV data were reduced using computer codes written for the IBM 370/165 computer program. Each raw data tape was read by the digital computer, and the number

of axial or vertical velocity samples lying in discrete bands were computed from a relation of the form

$$P(U) = \frac{m}{M} \quad (5)$$

where m is the number of samples found in the interval $(U \pm \Delta U/2)$ and M is the total number of samples in the data set. The velocity interval (ΔU) used was generally one-third of the standard deviation of the velocity at the point being studied, but smaller velocity bands $(\Delta U = 12 \text{ ft/sec})$ were used in several instances. By inspecting each data histogram, upper and lower limits of a bandpass filter were identified. These limits were purposely kept broad enough that only samples resulting from system-induced noise were excluded. The histogram data to be presented in Section 5.2 were not filtered, however, since the behavior of the histogram near the limits was of interest.

The velocity corresponding to each valid period sample was computed from

$$U_i = K_U \left(f_U^* - \frac{1}{\tau_{U_i}} \right) \quad (6)$$

and

$$V_i = -K_V \left(f_V^* - \frac{1}{\tau_{V_i}} \right) \quad (7)$$

where U_i and V_i are the horizontal and vertical velocity components for the i^{th} particle, τ_{U_i} and τ_{V_i} are the corresponding periods, and f_U^* and f_V^* are reference frequencies for the horizontal and vertical fringe systems, respectively. The fringe spacing or calibration constants (K_U or K_V) were computed, for example, from the relation

$$K_U = \frac{\lambda}{2n \sin\left(\frac{\theta_U}{2}\right)} \quad (8)$$

where λ is the wavelength of the incident radiation, θ_U is the convergence angle for the beams forming the horizontal fringe system, and n is the index of refraction of the fluid medium. For the temperatures and pressures of the experiments, the index of refraction was essentially unity.

The desired statistical parameters of the flow were obtained from the arithmetically averaged moments of the individual measurements as shown in Table 3. The relations

shown are applicable to simultaneously acquired data for a fringe system arbitrarily rotated with respect to the flow axes (Ref. 12). In the present case, the probe volume orientation angles (ψ and ϕ) were, respectively, 0 and $\pi/2$ radians in all cases. The use of arithmetic averages in the data reduction procedure neglects the possible contribution of statistical bias (Ref. 15) to the results. Previous experiments in naturally seeded jet flows (Refs. 11 and 12) have shown that bias of the data was negligible so that the use of arithmetic averages was considered satisfactory.

Table 3. Relations for the Evaluation of Simultaneously Acquired Data

Parameter	Formulation
1. Mean Axial Velocity	$u = \frac{1}{\sin(\phi + \psi)} [u_m \sin \phi - v_m \sin \psi]$
2. Mean Vertical Velocity	$v = \frac{1}{\sin(\phi + \psi)} [u_m \cos \phi - v_m \cos \psi]$
3. Mean Flow Angularity	$\phi = \arctan (v/u)$
4. Mean Square Axial Velocity	$\overline{u^2} = \frac{1}{\sin^2(\phi + \psi)} [\overline{u_m^2} \sin^2 \phi - 2\overline{u_m v_m} \sin \phi \sin \psi + \overline{v_m^2} \sin^2 \psi]$
5. Mean Square Vertical Velocity	$\overline{v^2} = \frac{1}{\sin^2(\phi + \psi)} [\overline{u_m^2} \cos^2 \phi - 2\overline{u_m v_m} \cos \phi \cos \psi + \overline{v_m^2} \cos^2 \psi]$
6. Cross Correlation	$\overline{uv} = -\frac{1}{\sin^2(\phi + \psi)} \left[\frac{1}{2} (\overline{u_m^2} \sin 2\phi + \overline{v_m^2} \sin 2\psi) - \overline{u_m v_m} \sin(\phi + \psi) \right]$
7. Axial Turbulent Intensity	$\sigma_u = \sqrt{\frac{M}{M-1}} (\overline{u^2} - u^2) / u$
8. Vertical Turbulent Intensity	$\sigma_v = \sqrt{\frac{M}{M-1}} (\overline{v^2} - v^2) / v$
9. Reynolds Stress	$\tau = -\rho(\overline{uv} - uv)$
With	$\overline{u_m^n} = \frac{1}{M} \sum_{i=1}^M u_{m_i}^n$ $\overline{v_m^n} = \frac{1}{M} \sum_{i=1}^M v_{m_i}^n$ $\overline{u_m v_m} = \frac{1}{M} \sum_{i=1}^M u_{m_i} v_{m_i}$

Mean axial velocities were also determined from the supporting pressure and temperature instrumentation. For the subsonic jet studies, the velocities were calculated from

$$u^2 = 2gJc_p T_o \left[1 - \left(\frac{P_o}{P_\infty} \right)^{\frac{1-\gamma}{\gamma}} \right] \quad (9)$$

In the supersonic jet studies, an iteration method was used to calculate velocities from the energy equation

$$u = M \sqrt{\gamma R T_o \left(1 + \frac{\gamma-1}{2} M^2 \right)} \quad (10)$$

and the Rayleigh-Pitot formula

$$\frac{P_{o2}}{P_{o1}} = \frac{\left(\frac{\gamma+1}{2} M^2 \right)^{\gamma/(\gamma-1)}}{\left(\frac{2\gamma}{\gamma-1} M^2 - \frac{\gamma-1}{2} \right)^{1/(\gamma-1)} \left(1 + \frac{\gamma-1}{2} M^2 \right)^{\gamma/(\gamma-1)}} \quad (11)$$

Shock locations and structure were directly measured from the shadowgraph pictures of the underexpanded jet.

3.0 PARTICLE DYNAMIC LIMITATIONS ON TURBULENCE MEASUREMENTS

A laser velocimeter obtains information on fluid velocity and turbulence characteristics by measuring the motion of particles contained in the medium. If the flow field possesses velocity gradients and/or if the fluid motion is turbulent, the particles will lag the fluid motion by an amount proportional to the particle diameter and density. For example, the equation of motion of a Stokesian particle (Ref. 16) subjected to a change in velocity is

p. 354, 357

$$\frac{\partial u_p}{\partial t} + \gamma u_p = \gamma U \quad (12)$$

where

$$\gamma = \frac{4\nu}{d_p^2 \rho_p} \quad 18 \mu \quad (13)$$

For the initial condition,

$$U_p(t = 0) = U(t = 0) = U_0 \quad (14)$$

and a flow field prescribed by

$$U(t > 0) = U_1 \quad (15)$$

the particle velocity at any time is

$$U_p = U_1 + (U_0 - U_1) e^{-\gamma t} \quad (16)$$

The function (γ) defined by Eq. (13) may, therefore, be regarded as a response parameter for the particle in question since it characterizes the particle lag at any time.

Many studies of LV characteristics (Refs. 17 through 20) have considered the response of particles to fluid transients in an effort to determine the particle size that will respond adequately to a specified flow field. If all particles in a given flow were of a single size and type, these studies would be sufficient to define the effect of particle lags on LV measurements. In practice, however, a data set will generally contain measurements that arise from many different types of particles. If the scatter material consists of natural particulates contained in an air supply it is obvious that a range of particle sizes will be present because of the wide size variation of particles contained in the atmosphere (Refs. 21 and 22). By artificially seeding a flow, one attempts to control the results by introducing particles of known characteristics in sufficient number to bias the data set to a desired type of particle. This procedure can be made more effective by filtering the supply air to remove most of the natural seed materials, but one must still recognize that most seeding devices produce a range of particle sizes rather than a single type of particle.

It is apparent, then, that most sets of LV data contain information from particles of different sizes and densities. For the simple example cited above, it follows from a Taylor series expansion of Eq. (16) that the spread in velocities resulting from variation in the response parameter (γ) is (for constant ν)

$$\delta U_p = (U_p - U_1) \gamma t [\delta(\ell_n d_p^2) + \delta(\ell_n \rho_p)] \quad (17)$$

Although Eq. (17) expresses the variation of velocities in a Lagrangian reference frame, transformation to an Eulerian coordinate system does not alter the basic premise that a range of velocities dependent on the physical characteristics of the particle rather than a local manifestation of turbulence will be measured by an LV. It is postulated, therefore, that apart from any instrumental broadening (Refs. 11 and 12), an LV will indicate the

presence of turbulence even in a laminar flow. The magnitude of this minimum indicated turbulence intensity is determined by (1) the velocity lags of the particles passing through the probe volume, (2) the ability of the LV to obtain data from particles of a given size, and (3) the size and density distribution of the particles comprising a data set.

3.1 PARTICLE DYNAMICS RELATIONS

If the preceding hypothesis is to be quantitatively evaluated, it is necessary to consider the motion of particles in some detail. For the assumptions that (1) the particles contained in the fluid are spherical, have a much greater density than the fluid, and are sufficiently low in concentration (number/volume) so that neither the fluid nor particle motion is disturbed by other particles; (2) heat and mass transfer between the fluid and particles is negligible; and (3) the dominant force acting on the particles is viscous drag, the particle velocity may be obtained from

$$\frac{\delta \vec{V}_p}{\delta t} = \frac{3}{4} \frac{\rho}{\rho_p} \frac{|\vec{V} - \vec{V}_p|}{d_p} (\vec{V} - \vec{V}_p) C_D \quad (18)$$

while its position is given by

$$\frac{\delta \vec{r}}{\delta t} = \vec{V}_p \quad (19)$$

These equations, subject to the initial conditions

$$\begin{aligned} \vec{V}_p(\vec{r} = \vec{r}_0, t) &= \vec{V}(\vec{r} = \vec{r}_0, t) \\ \vec{r}(t = 0) &= \vec{r}_0 \end{aligned} \quad (20)$$

are solved by the fourth-order Runge-Kutta integration of Ref. 20 for a modified Stokes drag law of the form (Ref. 23)

$$C_D = \frac{24}{Re_p} f(Re_p) \quad (21)$$

with

$$f(Re_p) = 1 + 0.197 Re_p^{0.63} + 0.00026 Re_p^{1.38} \quad (22)$$

where

$$Re_p = \frac{\rho d_p |\vec{V} - \vec{V}_p|}{\mu} \quad (23)$$

When the mean fluid velocity and temperature gradients are known throughout a flow field, the system of Eqs. (18) through (23) can be solved to give the particle velocity at any point. For the subsonic jet to be discussed in Section 4.0, this information is available from previous experiments (Refs. 12, 24, and 25). The underexpanded jet of Section 5.0 was analyzed by the method of characteristics and the theory of Ref. 26 to give its flow field through the reacceleration downstream of the first Mach disc.

Figure 4 presents the mean centerline axial velocity distribution for the subsonic jet along with the velocity difference ($U_p - u$) for 5- μm -diam particles having densities of 1.0 and 3.0 grams per cubic centimeter (g/cc). In both cases, it was assumed that the particle and fluid were traveling at the same velocity in the stilling chamber. The lighter particle is seen to have reached the gas velocity within two diameters of the nozzle exit plane but fails to follow the fluid deceleration following the end of the potential core. This behavior is much more severe in the case of the heavier particle which fails to reach the fluid velocity by the end of the core then overshoots the local gas velocity by approximately 5 percent near $X/D = 9$. It will be seen in Section 3.2.2 that a 5- μm -diam

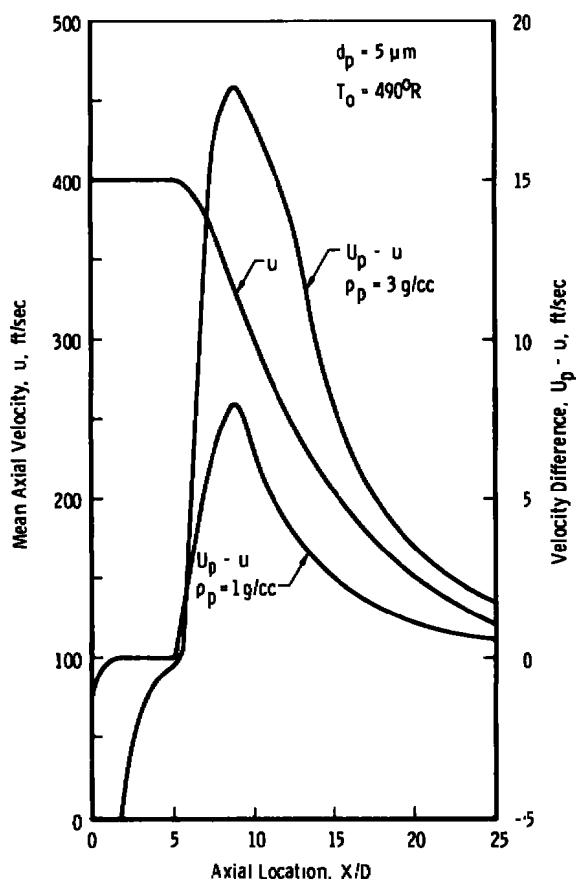


Figure 4. Effect of particle density on velocity lag in the subsonic jet.

particle has a relatively low probability of occurring in the present flows. Nevertheless, Fig. 4 illustrates that particle density differences can change the basic lag of a particle of fixed diameter.

In Fig. 5, the theoretical gas velocity field is shown for a sonic nozzle exhausting at an exit-to-ambient static pressure ratio of 4.0. Also shown are the velocity differences for particles having a specific gravity of 1.0 and diameters of 1 and 2 μm . The predicted lags for both particle sizes are, as expected, much larger than in the preceding example. Upstream of the shock wave, the larger particle lags the flow by over 100 ft/sec. Immediately downstream of the shock, both particles are traveling several hundred feet per second faster than the gas, but for either case the particle velocity has decayed to within 5 percent of the gas velocity within 0.25 in. of the shock. The preceding results emphasize that particle velocities will differ significantly from that of the gas at some locations in either flow field being studied. Consequently, it is expected, in at least the underexpanded jet, that turbulence effects will be obscured by the spread in velocity due to particle dynamic effects. To evaluate the magnitude of the rms velocity deviation caused by particle lags, however, the magnitude of several probability distribution functions must be considered.

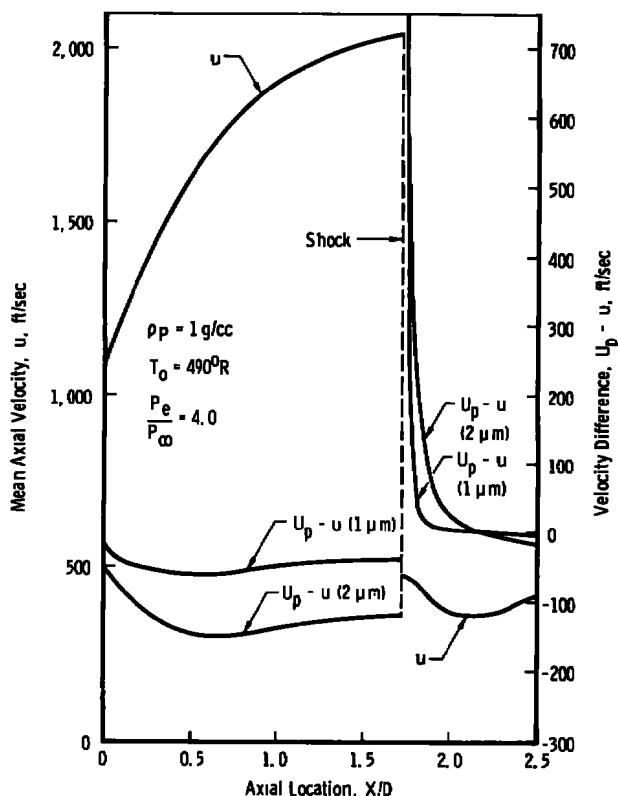


Figure 5. Effect of particle diameter on velocity lag in the underexpanded jet.

3.2 PROBABILITY DISTRIBUTION FUNCTIONS

The distribution of velocities at a point in a one-dimensional flow field is conveniently characterized by a probability density function ($f(U)$), which has the property that the mean and central moments of velocity are given by

$$u = \int_{-\infty}^{\infty} U f(U) dU \quad (24)$$

and

$$\overline{u'^n} = \int_{-\infty}^{\infty} (U - u)^n f(U) dU \quad (25)$$

where

$$\int_{-\infty}^{\infty} f(U) dU = 1 \quad (26)$$

For a laminar flow having the velocity U_1 at the point under consideration, the probability density function (p.d.f.) becomes a Dirac delta function (Ref. 27) so that $f(U) = 1$ for $U = U_1$ and $f(U) = 0$ if $U \neq U_1$. In laminar flows, then, the mean velocity is given by $u = U$ and the central moments are $\overline{u'^n} = 0$.

It is not convenient to use the p.d.f. in analyzing experimental data, however, since its accurate estimation requires more samples than can be conveniently taken with an individual realization LV system. Accordingly, one may define a probability distribution function (P.D.F.) which is related to the p.d.f. by

$$P(U_k) = \int_{U_k - \frac{\Delta U}{2}}^{U_k + \frac{\Delta U}{2}} f(U) dU \quad (27)$$

where $P(U_k)$ is the fraction of a total data set which lies in an interval (ΔU), centered around a velocity (U_k), and may be obtained directly from a histogram of the data set. The mean velocity is obtained from the P.D.F. by

$$u = \sum_{k=1}^M U_k P(U_k) \quad (28)$$

while the central moments are given by

$$\overline{u'^n} = \sum_{k=1}^M (U_k - u)^n P(U_k) \quad (29)$$

As in the case of the p.d.f., Eq. (29) may be used to judge whether a flow is laminar or turbulent.

For a steady, laminar flow, the P.D.F. measured by an LV is, in view of Eq. (17), a measure of the number of members of the data set having a response parameter that will allow them to arrive at the measurement point with a velocity (U_k). In a flow having a range of particle sizes and densities, the probability distribution will exhibit a spread, which from Eq. (29) appears to be turbulence. By replacing the flow under consideration with a laminar flow having identical mean velocity gradients, the minimum spread in velocities measured by the LV can be calculated if the shape of the P.D.F. can be estimated. The rms value ($\sqrt{u'^2}$) of the resulting histogram is then a measure of the minimum turbulence level that will be measured when a particular LV system is applied to a specific flow.

The probability distribution function is dependent on the joint probability that a given particle is of a size which allows its detection by the LV system, has a diameter ($d_p \pm \Delta d_p/2$), and a density ($\rho_p \pm \Delta \rho_p/2$) so that its velocity lies in the range ($U_k \pm \Delta U_k/2$). If such a function exists for the data set under consideration, the P.D.F. may be written functionally as

$$P(U_k) = \frac{\sum_i \sum_j P_{U_k}(d_{p_i}, \rho_{p_j})}{\sum_i \sum_j \sum_k P_{U_k}(d_{p_i}, \rho_{p_j})} \quad (30)$$

It is assumed, further, that the ability of an LV to detect a particle is independent of the response characteristics of the particle, and that particle size and diameter are statistically independent. The joint probability function may then be defined as the product of individual probabilities so that

$$P_{U_k}(d_{p_i}, \rho_{p_j}) = P_D(d_{p_i}) P_N(d_{p_i}) P(\rho_{p_j}) \quad (31)$$

where $P_D(d_{p_i})$ is the probability that the LV system can detect a particle of diameter (d_{p_i}) traveling at velocity (U_k); $P_N(d_{p_i})$ is the probability that a particle will have a diameter (d_{p_i}); and $P(\rho_{p_j})$ is the probability that a detected particle will have a density (ρ_{p_j}). Approximate relations for these individual probabilities are developed in the sections to follow.

3.2.1 LV Detection Characteristics

The ability of an LV to detect a particle traveling at a specified velocity is determined by the signal-to-noise (S/N) ratio of the Doppler burst signal generated by a particle traversing the fringe system established in the probe volume. Consequently, the probability of detecting a particle of given size is related to the light scattered by the particle, the collection efficiency of the optical system and the signal gains due to the PMT, and any amplifiers used in the system. From the work of Farmer and Brayton (Refs. 28 through 30), the S/N ratio of a signal may be expressed as

$$(S/N)_i = \left[\frac{\pi^2 \eta G}{16h} \right] \left[\frac{(\Delta\theta)^4 P_L}{\theta} \right] \frac{\sigma_i(\phi)}{U_{pi}} V_i^2 \quad (32)$$

where the first term is a function of the system electronics, the second depends on its optical properties, $\sigma_i(\phi)$ is the scattering cross section of the particle, U_{pi} is its velocity, and V_i is the visibility function for the particle.

A simplified analysis of the Mie scattering process (Ref. 31) suggests that, for a single scatter center in the probe volume, the scattering cross section may be written as

$$\sigma_i(\phi) = \frac{\pi d_{pi}^2}{4} g(\phi, \chi_i, n) Q(\chi_i, n) \quad (33)$$

where $g(\phi, \chi_i, n) = g_i$ is a Mie scattering function and $Q(\chi_i, n) = Q_i$ is the scattering efficiency. From Ref. 30, the visibility function for near paraxial viewing of a spherical particle is

$$V_i = \frac{J_1\left(\frac{\pi d_{pi}}{\delta}\right)}{\left(\frac{\pi d_{pi}}{\delta}\right)} \quad (34)$$

where $J_1(\pi d_{pi}/\delta)$ is a Bessel function of the first kind of order one and δ is the fringe spacing. Substituting Eqs. (33) and (34) in Eq. (32), one may express the S/N ratio as

$$(S/N)_i = \left(\frac{\pi^2 \eta G}{64h} \right) \left(\frac{P_L (\Delta\theta)^4 \delta^2}{\theta} \right) \left(\frac{g_i Q_i}{U_{pi}} \right) J_1^2 \left(\frac{\pi d_{pi}}{\delta} \right) \quad (35)$$

The probability that a particle will be detected by the LV may be defined as

$$P_D(d_{p_i}) = \frac{\int_{d_{p_i} - \frac{\Delta d}{2}}^{d_{p_i} + \frac{\Delta d}{2}} (S/N)_i \delta d_{p_i}}{\int_{d_{p_{\min}}}^{d_{p_{\max}}} (S/N)_i \delta d_{p_i}} \quad (36)$$

where the minimum and maximum particle diameters are assumed known from the particle size distribution or by the upper and lower values of the various threshold detectors employed in the system. Introducing Eq. (35) in (36), one obtains

$$P_D(d_{p_i}) = \frac{\int_{d_{p_i} - \frac{\Delta d}{2}}^{d_{p_i} + \frac{\Delta d}{2}} \frac{g_i Q_i}{U_{p_i}} J_1^2\left(\frac{\pi d_{p_i}}{\delta}\right) \delta d_{p_i}}{\int_{d_{p_{\min}}}^{d_{p_{\max}}} \frac{g_i Q_i}{U_{p_i}} J_1^2\left(\frac{\pi d_{p_i}}{\delta}\right) \delta d_{p_i}} \quad (37)$$

For wavelengths near 500 nm, particles greater than 0.5 μm and a single index of refraction, g_i increases with increasing values of χ_i , while Q_i decreases so that their product is nearly constant. The term U_i is a weak function of d_{p_i} if the flow possesses slight velocity gradients or if the particle size range is small. It is, moreover, a requirement of Eq. (31) that U_i be independent of d_{p_i} in Eq. (37) if the probability of detection is to be statistically independent of the particle size distribution. Accordingly, it is assumed that the quantity $(g_i Q_i / U_{p_i})$ is constant so that Eq. (37) reduces to

$$P_D(d_{p_i}) = \frac{\int_{d_{p_i} - \frac{\Delta d}{2}}^{d_{p_i} + \frac{\Delta d}{2}} J_1^2\left(\frac{\pi d_{p_i}}{\delta}\right) \delta\left(\frac{\pi d_{p_i}}{\delta}\right)}{\int_{d_{p_{\min}}}^{d_{p_{\max}}} J_1^2\left(\frac{\pi d_{p_i}}{\delta}\right) \delta\left(\frac{\pi d_{p_i}}{\delta}\right)} \quad (38)$$

Figure 6 presents the probability of detection and the cumulative distribution function (C.D.F.) defined as

$$C_D(d_{p_i}) = \int_{d_{p_{\min}}}^{d_{p_i}} P_D(d_{p_i}) \delta d_{p_i} \quad (39)$$

for an LV having a fringe spacing of $\delta = 30 \mu\text{m}$ with $d_{p_{\min}} = 0$ and $d_{p_{\max}} = 50 \mu\text{m}$. This fringe spacing approximates that of the axial component of the LV described in Section 2.2. It is interesting to note that the probability of detecting a particle is a maximum at $d_{p_i} = 0.583 \delta$ and is low ($P_D < 0.001$) for particles having diameters less than $1.5 \mu\text{m}$. This suggests that the present LV is not ideal for use in highly accelerated flows since it is more apt to detect signals arising from (relatively) large particles.

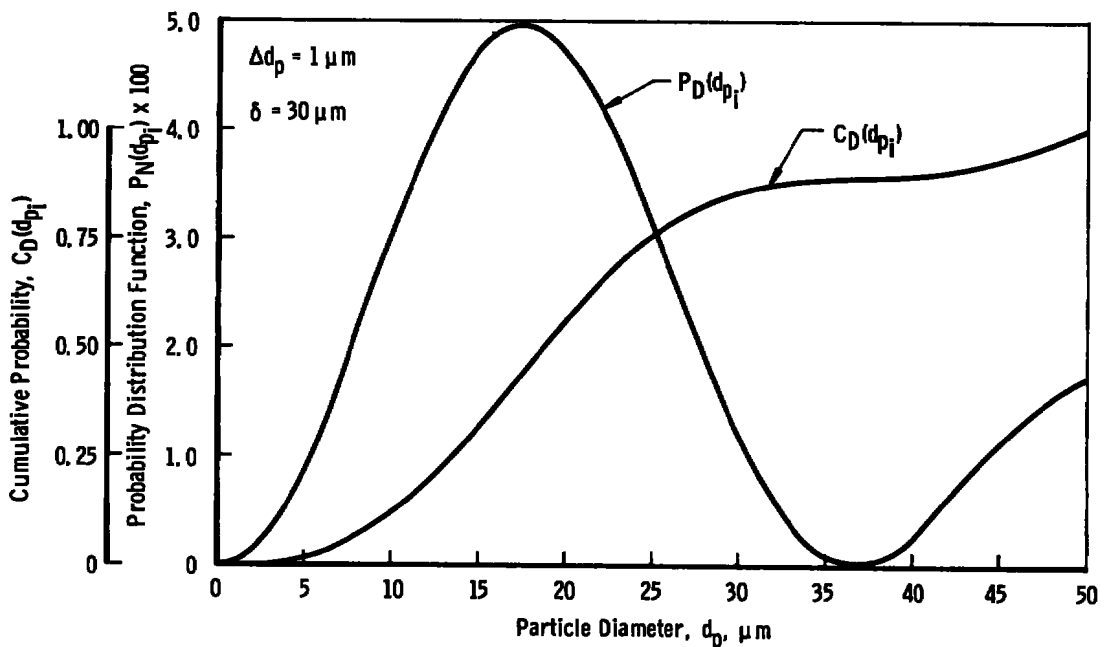


Figure 6. Influence of particle size on LV detection probabilities.

3.2.2 Particle Size Distributions

The distribution of particle sizes in an air supply or the atmosphere is an area of great uncertainty. Most surveys of atmospheric pollutants (e.g. Ref. 21) suggest that particle concentration is a monotonically decreasing function of size although some recent studies (Ref. 22) suggest that the distribution is actually bimodal with an increase in particle concentration between 5 and $10 \mu\text{m}$. In an air supply system, moreover,

additional contaminants, such as oil, condensation, and rust or other solid particles, may be present. Recent studies of the ETF air supply system (Ref. 32) indicate that particle concentration also varies with location in the supply system or with the valving arrangement supplying air to a test unit.

For particle sizes above $5 \mu\text{m}$, representative values of particle concentration in the present air supply are available from Ref. 32. If it is assumed that the concentration of submicron particles is similar to that found in a typical urban atmosphere (e.g., Ref. 33), it is possible to match the two sets of data by allowing the concentration to decay monotonically in accordance with the power law

$$N = A d_p^{-m} \quad (40)$$

A reasonable approximation to the referenced data is obtained for $A = 30.78$ and $m = 3.3$. The fraction of samples lying in an interval is then

$$P_N(d_{p_i}) = \frac{\int_{d_{p_i} - \frac{\Delta d}{2}}^{d_{p_i} + \frac{\Delta d}{2}} N \delta d_{p_i}}{\int_{d_{p_{\min}}}^{d_{p_{\max}}} N \delta d_{p_i}} \quad (41)$$

In evaluating Eq. (41), it is convenient to take $d_{p_{\min}}$ as the smallest particle that can be seen with the LV system. It would be more proper to assign this restriction to Eq. (38) since it is an LV characteristic; but, whereas the Bessel function $J_1(\pi d_{p_i}/\delta)$ is well-behaved near $d_{p_i} = 0$, the concentration predicted by Eq. (40) becomes unbounded as $d_{p_i} \rightarrow 0$. The minimum observable particle size is dictated by LV system noise, PMT gains, laser power, velocity, and trigger level settings. Equation (41) was evaluated for $d_{p_{\min}} = 0.5$ and $1.0 \mu\text{m}$ which are significantly above the $0.2\text{-}\mu\text{m}$ limit commonly assumed for individual realization systems. These results are shown in Fig. 7 along with the corresponding C.D.F.'s. It is seen for the above threshold values that the probability that a detected particle is less than $5 \mu\text{m}$ is at least 90 percent which partially counteracts the relatively large fringe spacing of the present LV and helps to minimize particle lag effects in the data set.

This may be seen more clearly, however, if one computes the joint probability that a particle of a given size will occur and that the LV will be able to detect it. Such a joint probability is defined by

$$P_{ND}(d_{p_i}) = P_N(d_{p_i}) P_D(d_{p_i}) \quad (42)$$

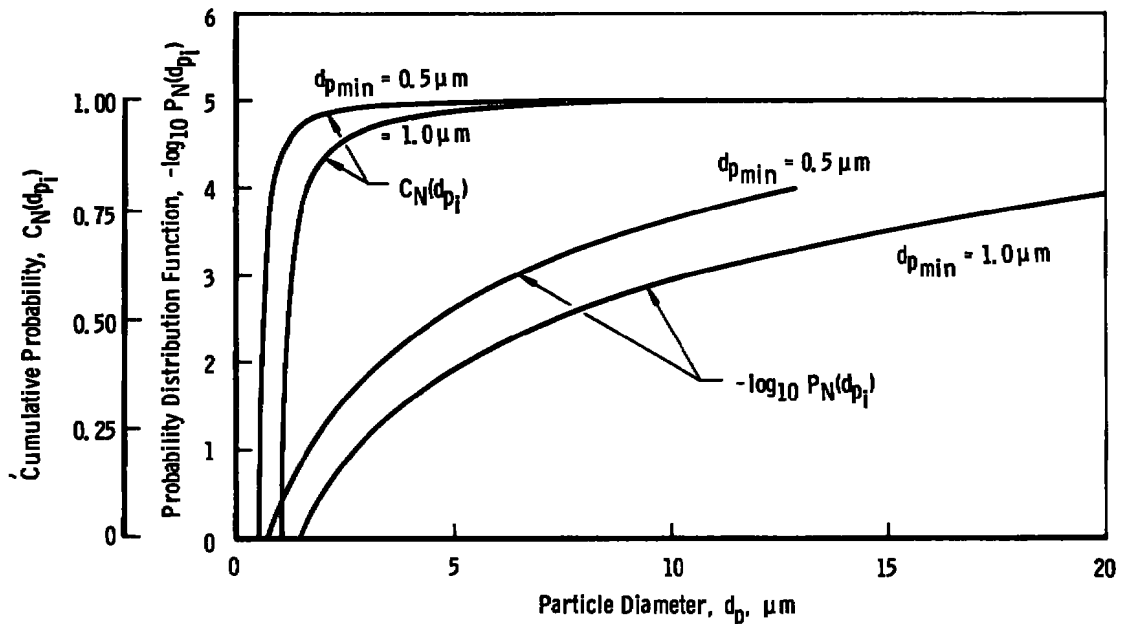


Figure 7. Distribution of particle sizes in the air supply.

The joint probability distribution, re-normalized over the observable particle size range, is shown in Fig. 8 for a 30- μm fringe system with 0.5- and 1- μm threshold values. The results clearly indicate that an increased detection threshold increases the probability that individual measurements in a data set will be obtained from larger particles. It has been observed previously (Refs. 11 and 12) that improper setting of trigger levels can lead to serious errors in experimental results. The present analysis shows, additionally, that control of the detection threshold is not solely a function of the LV electronics.

3.2.3 Particle Density Distributions

From Eq. (17), it is evident that, barring the existence of strongly bimodal density distributions, particle mass density has a secondary effect on the spread of velocities measured by an LV. Data on the density of particles comprising a data set are, moreover, generally unknown in applications where natural seed materials are used. For these reasons, several representative particle density distributions ($P(\rho_p)$) were used to estimate the effect of density on the particle dynamics of the data set.

In Fig. 9, three hypothetical cumulative density distributions are shown. While these C.D.F.'s are arbitrarily chosen, the range of values was taken from the study reported in

Ref. 32 for the ETF air supply where it was found that the composition of particulates consisted of 10- to 20-percent metals and metallic oxides. When it is considered that all but the heaviest metals have mass densities of approximately 8 g/cc or less while non-metals tend to range from 0.1 to 3 g/cc, the range of densities selected is realistic. The C.D.F., labeled as negatively skewed, is weighted to the heavier particles in the air supply while the positively skewed function assumes that non-metallic particles are dominant.

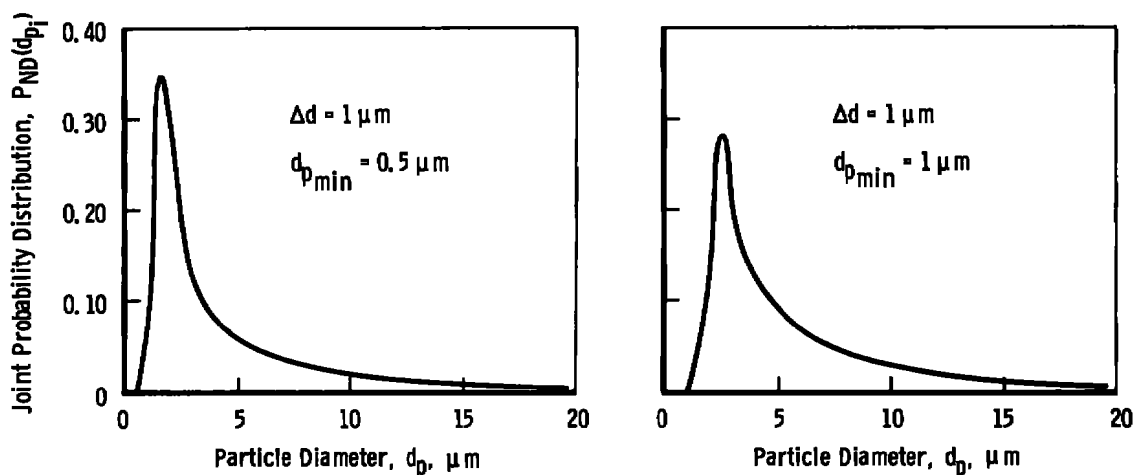


Figure 8. Effect of trigger level on the joint probability distribution.

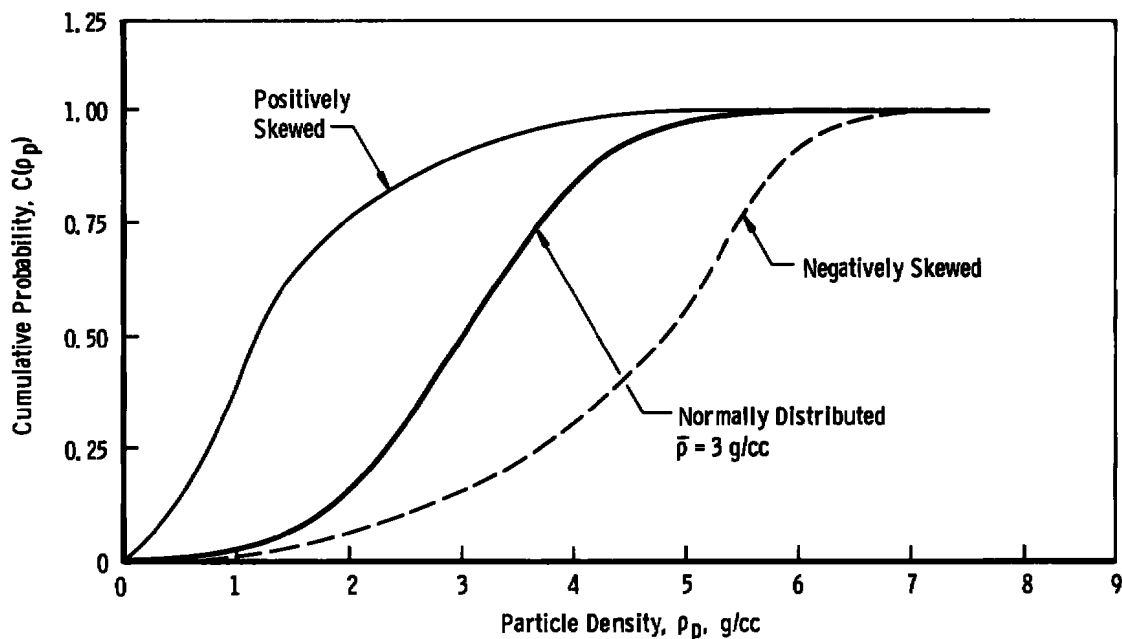


Figure 9. Particle density distribution functions.

3.3 MINIMUM TURBULENCE LEVELS

Using the probabilities determined in the preceding sections, one may evaluate Eq. (31) for a particular particle diameter and density range. This probability may then be assigned a location in velocity space through the particle dynamics calculations of Section 3.1. Repeating this procedure for the entire range of densities and diameters, then, allows one to evaluate Eq. (30) and determine the total probability of a particle lying in the interval $(U_k \pm \Delta U/2)$. The mean and apparent rms velocities may then be determined from Eqs. (28) and (29).

This procedure has been applied to the subsonic jet flow at $X/D = 2$ and $X/D = 10$, and the resulting histograms are presented in Fig. 10 for a particle detection threshold of $0.5 \mu\text{m}$. Near the jet exit, the velocity probability distribution is negatively skewed as would be expected for an accelerating flow. At the downstream station, this trend is reversed since the flow is decelerating. The calculated apparent turbulence intensities range from 1.4 percent for the positively skewed density distribution at $X/D = 2$ to 4.0 percent for the negatively skewed density distribution at $X/D = 10$. The actual apparent turbulence level should be less than the calculated values because the data were obtained from simultaneous measurements of the axial and vertical velocities. Since the vertical measurements were obtained from a $10\text{-}\mu\text{m}$ fringe system, the joint detection probability $(P_{U_k}(d_{p_i}, \rho_{p_j}))$ for the two-component LV system used in the subsonic jet studies would, accordingly, be weighted to smaller particles than predicted by a one-dimensional analysis.

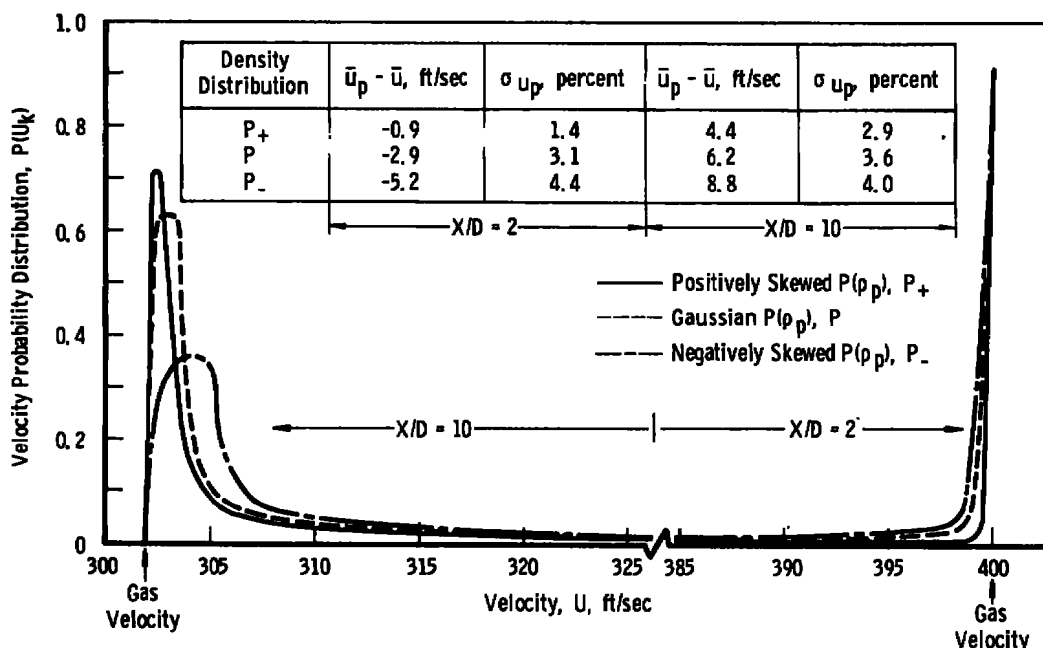


Figure 10. Velocity probability distribution in the near field of the subsonic jet.

The spread in the probability distribution ($P(U_k)$) for the underexpanded jet is shown in Fig. 11. Because of the higher flow velocities and increased noise levels that would be expected near the base plate, the joint probability function corresponding to a $1\text{-}\mu\text{m}$ threshold detection limit was used in the calculation of these histograms. The predicted spread in velocities ranges from 800 ft/sec at $X/D = 0.25$ to 1,300 ft/sec just upstream of the predicted Mach disc location ($X/D = 1.73$). While different density assumptions change the value of the mean and mode of the velocity distributions, the spread in velocities is affected only slightly for any of the density distributions. Since the standard deviation of the velocity distribution is obviously large, it is clear that accurate turbulence information cannot be obtained from measurements of the underexpanded jet with the present LV system.

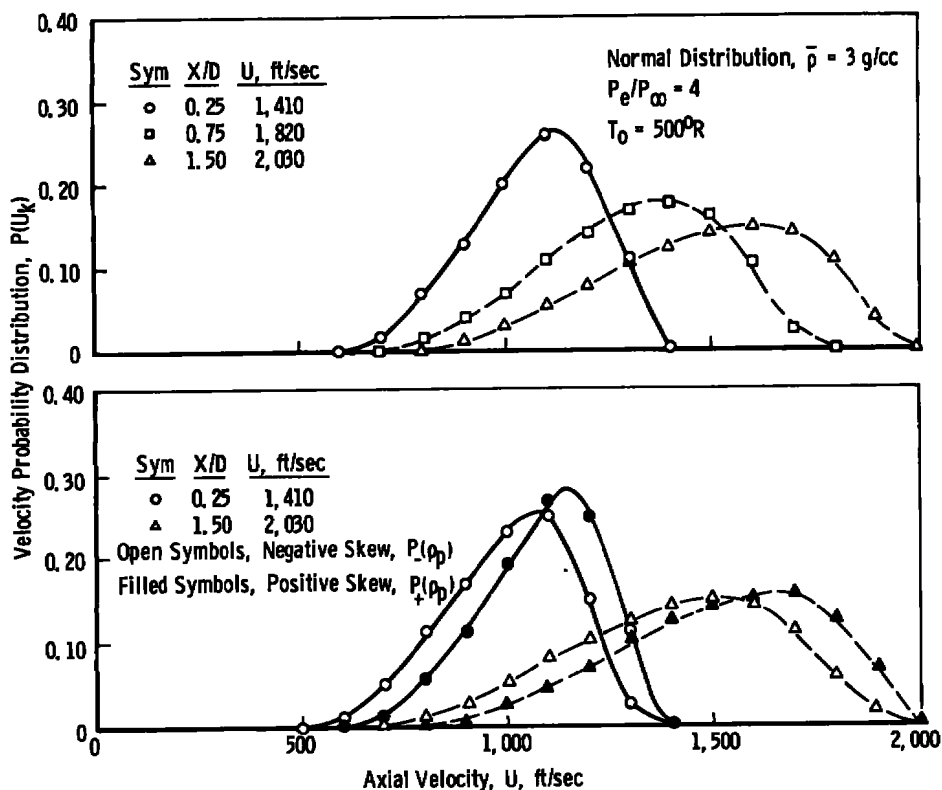


Figure 11. Velocity probability distributions in the near field of the underexpanded jet.

An interesting sidelight of the probability distribution analysis is that it allows one to test the hypothesis of Lo (Ref. 34) and Cline and Lo (Ref. 35) that in accelerating or decelerating flows the mode of the probability distribution is a better indicator of fluid velocity than the mean. The preceding results substantiate the hypothesis provided the flow is laminar and has unimodal distributions of particle size and density. The improvement to be gained using the mode as a velocity criterion, moreover, is slight in

the calculated examples. Indeed, it will be seen in Section 5.2 that a much better estimate of gas velocity is obtained by considering the velocity measured in the limiting case where the particle diameter goes to zero. This information is provided by the "tails" of the velocity histograms measured by an LV system.

Although the analysis given is approximate and contains many arguable assumptions, it shows clearly that an LV is limited in its ability to measure turbulence because of particle dynamic effects. If the flow is naturally seeded and the accelerations are large, there is little hope that accurate turbulence measurements can be made without recourse to improved electronics such as the upper threshold detector proposed by Pfeifer (Ref. 36) or use of particle sizing interferometers (Ref. 37) to simultaneously measure particle size and velocity. In seeded flows, moreover, care must be taken to control the distribution of particle sizes which implies that natural particulates of diameters or densities differing greatly from the seed material must be removed from the air supply. Finally, it is noted that, in a well-defined flow, the procedure presented could be inverted to allow the distribution of particle response parameters to be determined for the flow. In that event careful attention to the LV design and its detection threshold would be required.

3.4 SEEDING NONUNIFORMITIES

It has been shown experimentally (Refs. 11 and 12) and may be inferred from other investigations (Refs. 4, 5, and 38) that significant errors may be introduced in LV measurements of shear flows if the seeding material is nonuniformly distributed across a mixing layer. The errors introduced in such cases result from a biasing of the measurements to an inner or outer stream value rather than the particle lag effects considered earlier.

Consider two co-flowing streams which are initially separated by a slip line. The mean axial velocity of the eddies comprising the outer stream is u_1 while that of the inner stream is u_2 . The mean gas velocity along the slip line is then

$$\langle u \rangle = \frac{u_2}{2} (1 - \eta) \quad (43)$$

where the velocity ratio is

$$\eta = \frac{u_1}{u_2} \quad (44)$$

Although the mean gas velocity is assumed to be axial, local transverse fluctuations will cause mixing to occur along the slip line. Accordingly, an LV whose probe volume is

located along the line will obtain measurements from particles which, neglecting particle lags, are moving at the inner or outer stream velocity. If the particle concentration of the outer flow is N_1 and that of the inner stream is N_2 , the mean velocity measured by the LV would be

$$\bar{u} = \frac{N_1 P(N_1) u_1 + N_2 P(N_2) u_2}{N_1 P(N_1) + N_2 P(N_2)} \quad (45)$$

where $P(N_1)$ or $P(N_2)$ is the probability that a measurement will be obtained from particles initially contained in the outer or inner flow, respectively. The value of the probability at any location would depend on several factors, including the turbulent structure and velocity gradients in both streams, but the influence of nonuniform seeding can be illustrated by assuming $P(N_1) = P(N_2)$ so that Eq. (45) reduces to

$$\bar{u} = u_2 \frac{1 + \xi\eta}{1 + \xi} \quad (46)$$

where the particle concentration ratio is

$$\xi = \frac{N_1}{N_2} \quad (47)$$

The ratio of the measured-to-actual velocity is then

$$\frac{\bar{u}}{\langle u \rangle} = \frac{2(1 + \xi\eta)}{(1 - \xi)(1 + \eta)} \quad (48)$$

It is noted that, if $\xi = 1$, the measured and actual velocities are identical for any velocity ratio. For other concentration ratios, it is readily shown, from the limiting cases $\eta = 0$ and $\eta \rightarrow \infty$, that the measured velocities fall in the range

$$\frac{2}{\xi + 1} \leq \frac{\bar{u}}{\langle u \rangle} \leq \frac{2\xi}{\xi + 1} \quad (49)$$

so that large errors may be introduced because of seed concentration differences.

For the process described, there also exists an "apparent" turbulence intensity along the slip line that is independent of the actual velocity fluctuations occurring in the inner and outer flows. Defining the mean-square velocity for the gas as

$$\langle u^2 \rangle = \frac{u_1^2 + u_2^2}{2} \quad (50)$$

and noting that

$$\langle u'^2 \rangle = \langle u^2 \rangle - \langle u \rangle^2 \quad (51)$$

the rms velocity along the slip line is

$$\langle u'^2 \rangle^{1/2} = \frac{u_2}{2} \left| (\eta - 1) \right| \quad (52)$$

The "apparent" turbulence intensity is then

$$\sigma_{\langle u \rangle} = \frac{\langle u'^2 \rangle^{1/2}}{\langle u \rangle} = \frac{\left| \eta - 1 \right|}{\eta + 1} \quad (53)$$

One may similarly define a mean square velocity for the LV measurements of particle velocities as

$$\bar{u}^2 = \frac{N_1 u_1^2 P(N_1) + N_2 u_2^2 P(N_2)}{N_1 P(N_1) + N_2 P(N_2)} \quad (54)$$

where it has again been assumed that the particles do not lag the flow. From Eqs. (45), (51), and (54), with $P(N_1) = P(N_2)$, the measured rms velocity is

$$\sqrt{\bar{u}'^2} = \frac{u_2 \sqrt{\xi} \left| (\eta - 1) \right|}{\xi + 1} \quad (55)$$

so that the apparent intensity "seen" by the LV is

$$\sigma_{\bar{u}} = \frac{\sqrt{\xi} \left| (\eta - 1) \right|}{1 + \xi \eta} \quad (56)$$

The ratio of the measured-to-actual intensities is, from Eqs. (53) and (56),

$$\frac{\sigma_{\bar{u}}}{\sigma_{\langle u \rangle}} = \frac{\sqrt{\xi} (\eta + 1)}{1 - \xi \eta} \quad (57)$$

It is seen from Eq. (57) that, as in the case of the mean velocity, for $\xi = 1$ the measured and actual intensities are identical for all velocity ratios. The effect of the seed concentration ratio on the measured mean velocity and turbulence intensities is shown in Fig. 12. For $\eta = 2$, the LV measurements will indicate a lower velocity than exists for $\xi < 1$ and will yield a higher velocity than exists for $\xi > 1$. The apparent turbulence

intensity indicated by the instrument will be a maximum at $\xi = 0.5$ and is equal to the true value only at $\xi = 0.25$ and 1.0. Therefore, it may be inferred that the LV will yield only the correct mean velocity and turbulence intensity in a shear flow if the inner and outer streams are uniformly seeded.

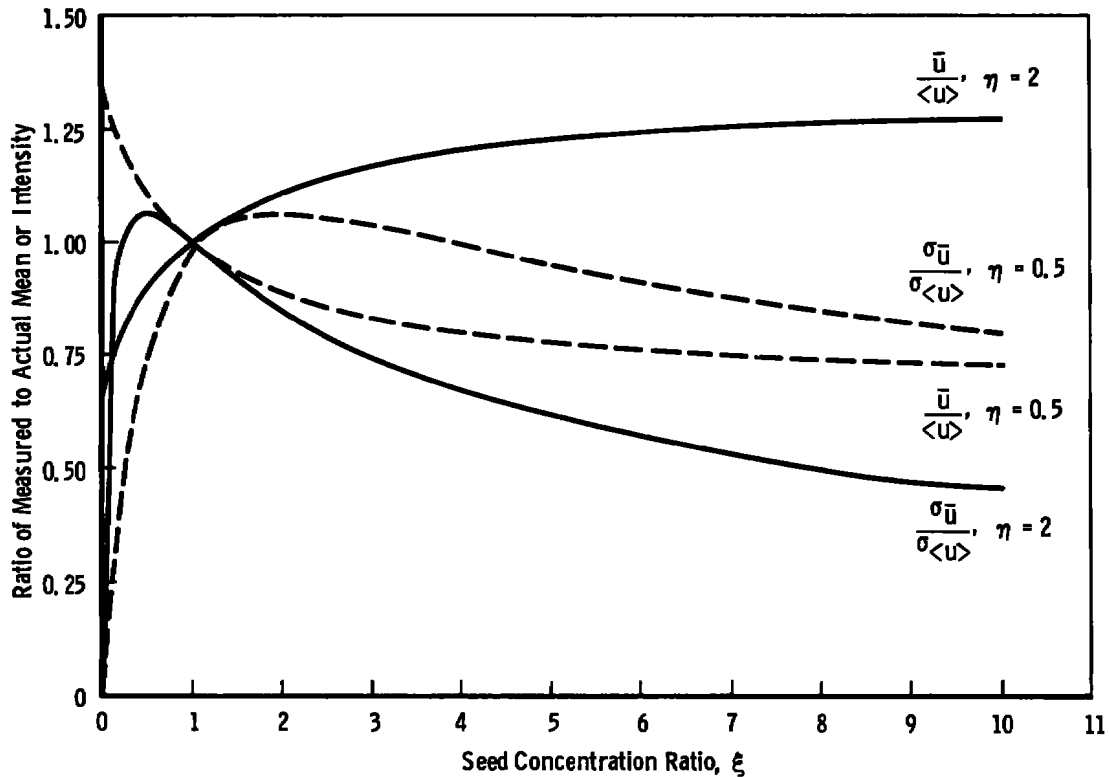


Figure 12. Effect of seeding nonuniformity on mean and RMS velocity measurements.

4.0 SUBSONIC JET RESULTS

Laser velocimeter measurements are presented for the mean velocities, turbulence intensities, Reynolds stresses, and velocity probability distributions for the flow field of a subsonic jet exhausting into still air. Data were obtained for a jet nominally (1) in thermal equilibrium with its surroundings and (2) having an initial temperature 350°R above that of the surrounding medium. Detailed measurements were made of the radial variation of the velocity field at axial stations of 2, 5, 10, and 20 nozzle diameters downstream of the nozzle exit plane. Additional measurements were made on the jet centerline for axial stations up to $X/D = 30$. In several cases, multiple test runs were made at a given station or condition to verify the repeatability of the results or to correct experimental deficiencies.

Total pressures and temperatures were measured at each station to provide data for direct comparison to the mean axial velocities determined by the LV. Additionally, hot-wire measurements of an isothermal jet with the present nozzle configuration (Refs. 11 and 12) are compared to the LV turbulence data. In the presentation which follows, the results have been normalized with the jet exit velocity (U_e), which varied between tests from 386.3 to 402.7 ft/sec.

4.1 CENTERLINE VARIATION OF FLOW PARAMETERS

The mean axial velocity decay, as determined from the total pressure and temperature probe data, is shown in Fig. 13 for both the unheated and heated flows. A potential core length of $X/D = 5.0$ is observed in the cold jet, while the centerline velocity decays in accordance with an inverse power law relation for $X/D > 10$. The heated jet centerline velocity decays faster than the unheated flow, with the end of the core potential reached near $X/D = 3.25$. In the heated jet far field, moreover, the centerline velocity continues to "roll-off" faster as shown by the exponents of the power law indicated in the figure. These results will be used in certain empirical expressions to be introduced in Section 4.2.

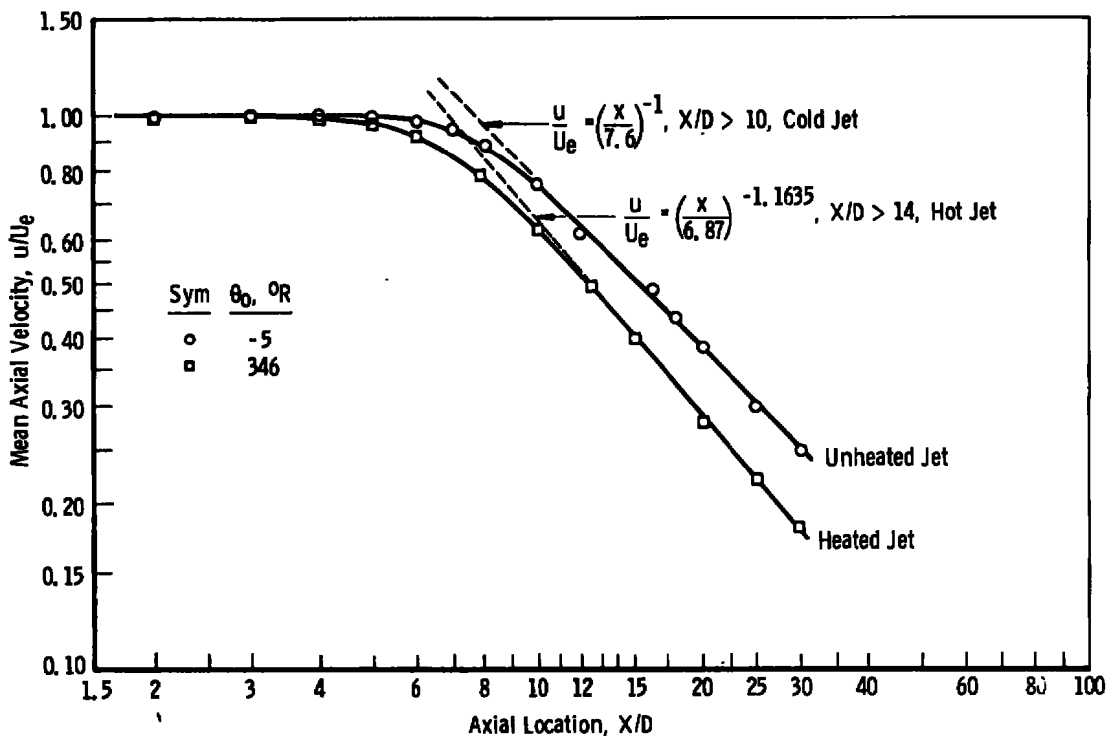
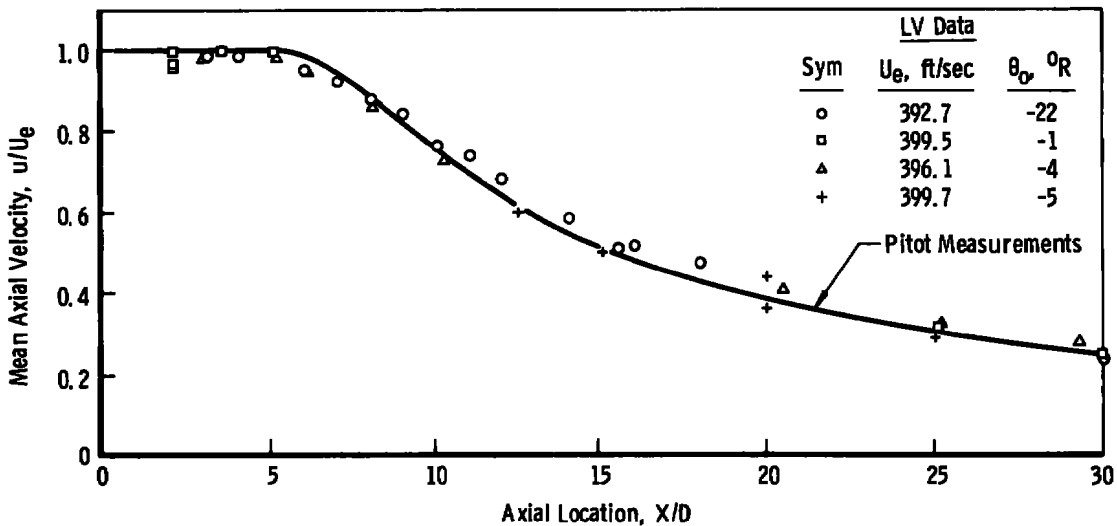
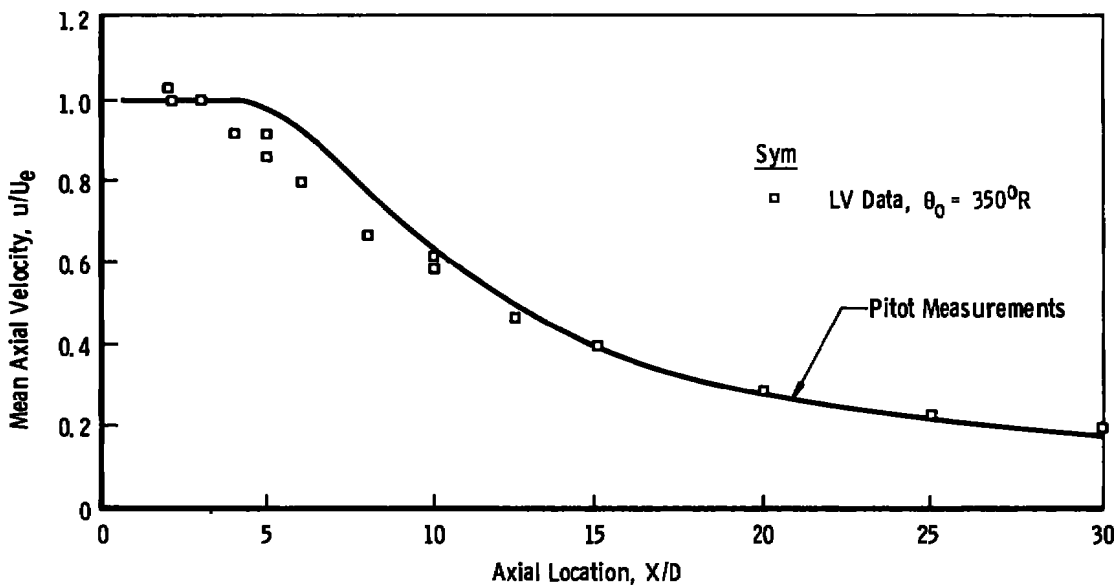


Figure 13. Pitot measurements of centerline velocity decay.

A comparison of the pitot and LV measurements of the centerline velocity decay is presented in Fig. 14. For the unheated jet (Fig. 14a), the two types of measurements are in good agreement with most of the LV results lying within 3 percent of the pitot data. In the heated jet (Fig. 14b), the LV data decay much faster than the pitot measurements with good agreement attained only for $X/D > 10$. The same trend is seen in the unheated flow for $5 < X/D < 8$ although the magnitude of the velocity difference is considerably less than the heated case.



a. Velocity decay along centerline of unheated jet



b. Velocity decay along centerline of heated jet
Figure 14. LV measurements of centerline velocity decay.

It is believed that the disagreement between the LV and pitot data is a result of a misalignment of the LV probe volume with the jet centerline. Since "on-line" data reduction was not available for the LV, it was necessary to determine the centerline location with the pitot tube after having positioned the LV probe volume so that it was coincident with the open end of the tube. This could be done accurately in the unheated flows so that only small errors in centerline alignment ($\Delta r \ll 0.05$ in.) resulted. In the heated flow, however, the high temperatures in the jet near field required that alignment be performed under non-flowing conditions (see Section 2.6). Expansion of the air supply ducting tended to raise the true centerline of the flow above the apparent centerline used for the LV traverses. This implies that horizontal traverses of the hot flow, which provide information on tangential velocities, are in error. Additionally, the apparent nozzle centerline was displaced horizontally possibly due to refraction effects in the heated flow. The data indicate that, for the heated flows, these displacements are, approximately, $\Delta r \approx 0.15$ in. for the horizontal axis and $\Delta r \approx 0.05$ in. for the vertical axis. Both displacements are sufficient to cause differences between measurements of the (small) tangential and radial velocity components in heated flows. Since turbulence results are obtained, statistically, from the individual velocity measurements, it will be seen in Section 4.3 that misalignment also affects the near-field measurements of the turbulence intensities.

The centerline distribution of the axial turbulence intensity is presented in Fig. 15 for the unheated jet and in Fig. 16 for the heated case. In Fig. 15, the LV data are compared to the hot-wire results of several investigations (Refs. 12, 24 and 39). It is seen that the LV data indicate a higher turbulence level than the hot wire. Such a result was predicted on the basis of particle dynamic considerations in Section 3.3 and may be regarded as qualitative affirmation of the concept set forth there.

Figure 16 compares the LV axial turbulence intensity measurements for the heated jet to the hot-wire data of Corrsin and Uberoi (Ref. 40). The maximum centerline turbulence intensity is higher and occurs farther upstream in the heated than in the unheated jet. While the LV data from the heated jet agree with the trend of the hot-wire results, they are uniformly higher than the hot-wire measurements. The effect of probe volume misalignment estimated from the radial traverse data of Section 4.3 are shown in Fig. 16 and indicate that the near-field ($X/D < 10$) axial intensities are high by 2 to 4 percent because of misalignment. Whether the remaining differences are due to particle dynamic broadening or experimental differences is uncertain.

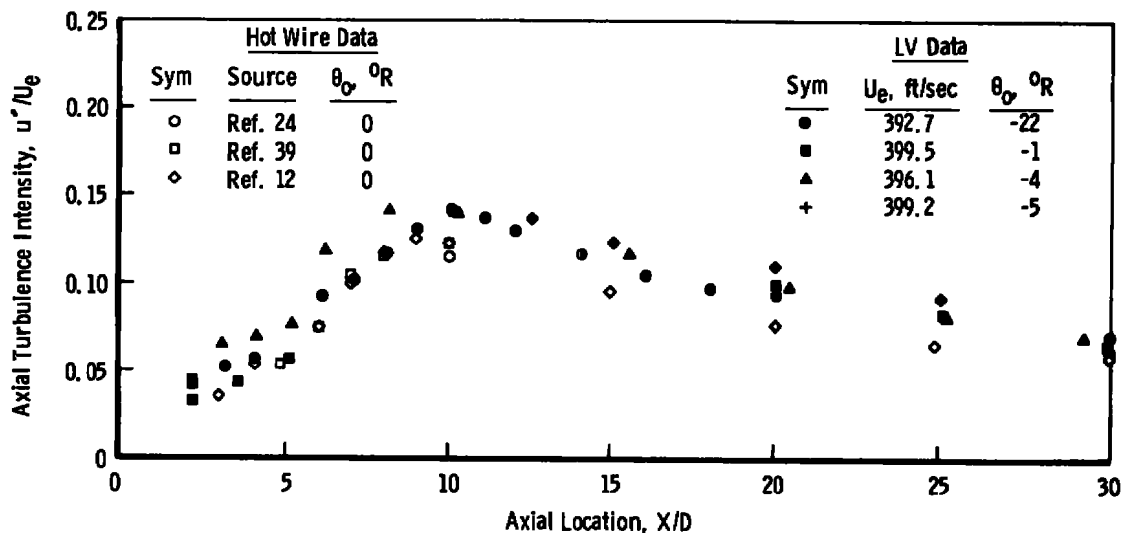


Figure 15. Centerline axial turbulence intensity distribution in unheated jet.

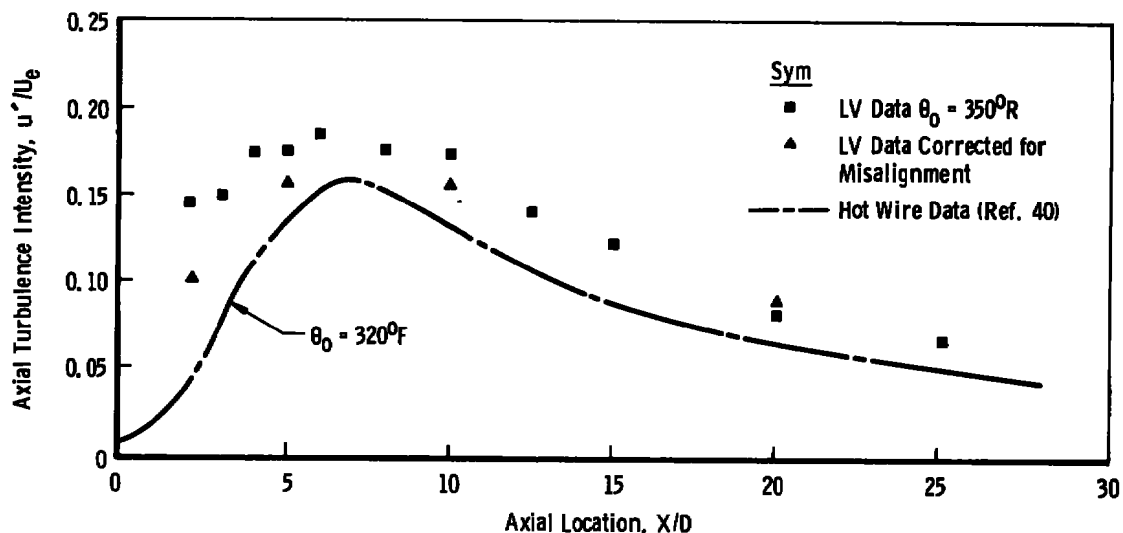


Figure 16. Centerline axial turbulence intensity distribution in heated jet.

In Fig. 17, LV measurements of the radial turbulence intensity in the unheated jet are compared to several sets of hot-wire data. The agreement is good over the entire axial range of the measurements. It will be seen in Section 4.2 that radial velocity gradients in the unheated flow are slight, and because the $10\text{ }\mu\text{m}$ fringe spacing for the LV vertical component increases the probability that only data from small particles will be processed, no significant broadening of the results is expected.

In Fig. 18, the radial intensities for the heated jet are compared to the unheated values. The effect of probe volume misalignment is again estimated from the data to be presented in Section 4.3. Even allowing for misalignment it is seen that, as with the axial component, higher intensities are obtained in heated flows and the maximum value occurs farther upstream. It has been noted (Ref. 24) that the ratio of the radial-to-axial turbulent intensity in an unheated flow ranges from 0.50 to 0.75. The present data indicate that this statement is also valid for moderately heated subsonic jets. Finally, it is noted that for the present LV system there is no distinction between radial and tangential velocities at the jet centerline (Section 2.2) so that the results of Figs. 17 and 18 may also be interpreted as the centerline tangential turbulence intensities.

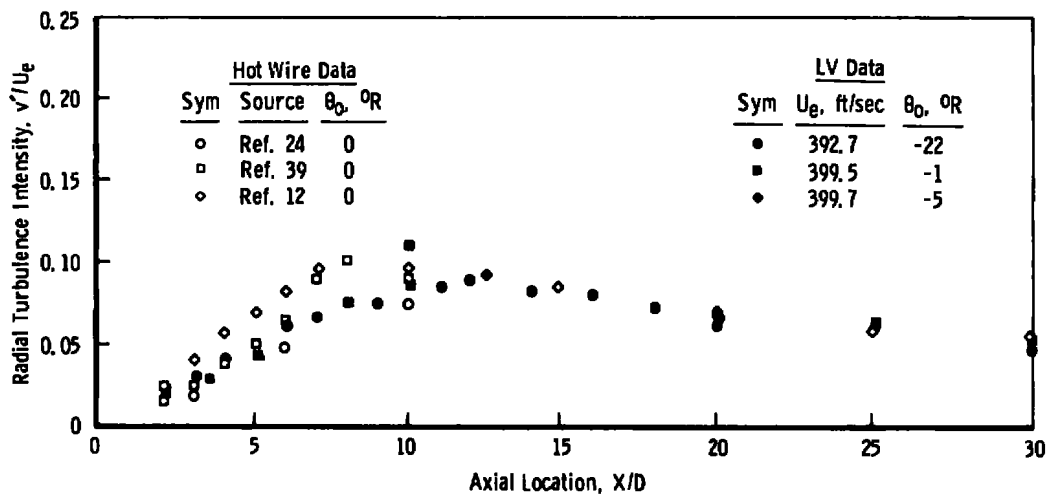


Figure 17. Centerline radial turbulence intensity distribution in unheated jet.

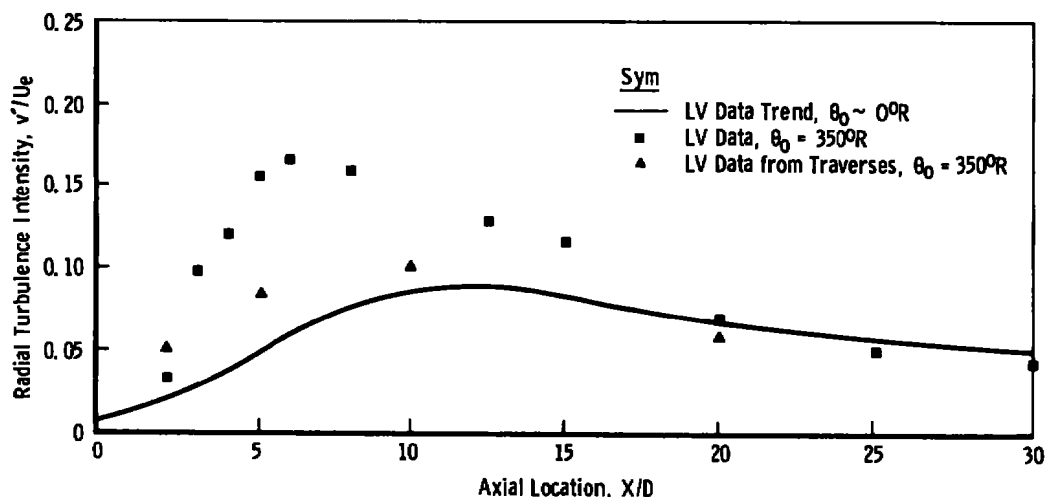


Figure 18. Centerline radial turbulence intensity distribution in heated jet.

4.2 MEAN VELOCITY MEASUREMENTS

The radial distribution of the mean axial velocity measured by the LV and pitot system at $X/D = 2$ is shown in Fig. 19. In Fig. 19b as in several other figures throughout this section, data are shown only for the positive half-plane. For these cases, insufficient data were obtained to adequately define the flow across the entire jet. The results are compared to a semi-empirical distribution for axial velocities in isothermal jets (Ref. 12),

$$\frac{u}{u_e} = \frac{u_c}{u_e} \exp(-\Lambda^2 \eta^2) \quad (58)$$

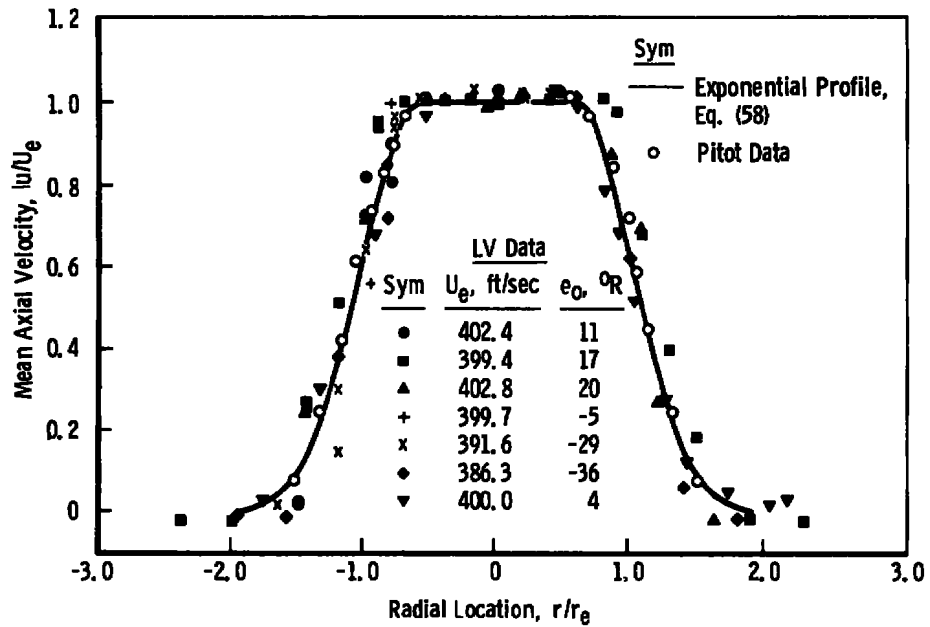
where Λ is a constant and η is a dimensionless location in the shear layer. It is seen that this expression provides a reasonable fit to both sets of jet data, and it will be used throughout this section to compare the heated and unheated data. While the LV and pitot measurements are in good agreement, the LV data indicate a less rapid growth of the shear layer than the pitot measurements. Furthermore, the Bragg-diffracted LV measured slightly negative values for the axial velocity at the edge of the unheated jet, which implies that a weak recirculation zone may exist at the periphery of that flow. A recirculation zone is not observed for the heated jet, which at $X/D = 2$, appears slightly broader than the unheated flow although the half-velocity widths of the two jets are essentially the same.

The mean axial velocities for $X/D = 5$ are shown in Fig. 20. As in the preceding case, the LV and pitot measurements are in good agreement across the jet for both heated and unheated flows. Despite the obvious depression in the centerline velocity for the heated jet, its half-velocity width is almost the same as the unheated flow so that differences between these two flows appears to be largely confined to the region within the half-velocity radius of the jet. Similar agreement of the LV and pitot measurements and the spreading characteristics of the jet are obtained at $X/D = 10$ (Fig. 21) and $X/D = 20$ (Fig. 22).

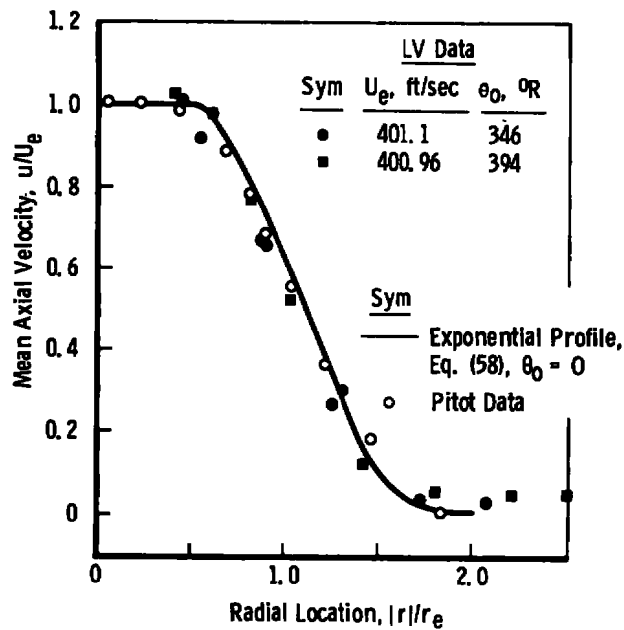
It is useful in analyzing the radial mean velocity results to compare the measured values to a theoretical prediction. For an axisymmetric, isothermal flow the continuity equation may be integrated to give

$$r v = - \int_0^r \frac{\partial u}{\partial x} r \, dr \quad (59)$$

Equation (59) has been evaluated for both the near- and far-field of isothermal jets in Ref. 12 and will be used in the remainder of this section for data comparisons.



a. Unheated jet



b. Heated jet

Figure 19. Axial velocity distributions at $X/D = 2$.

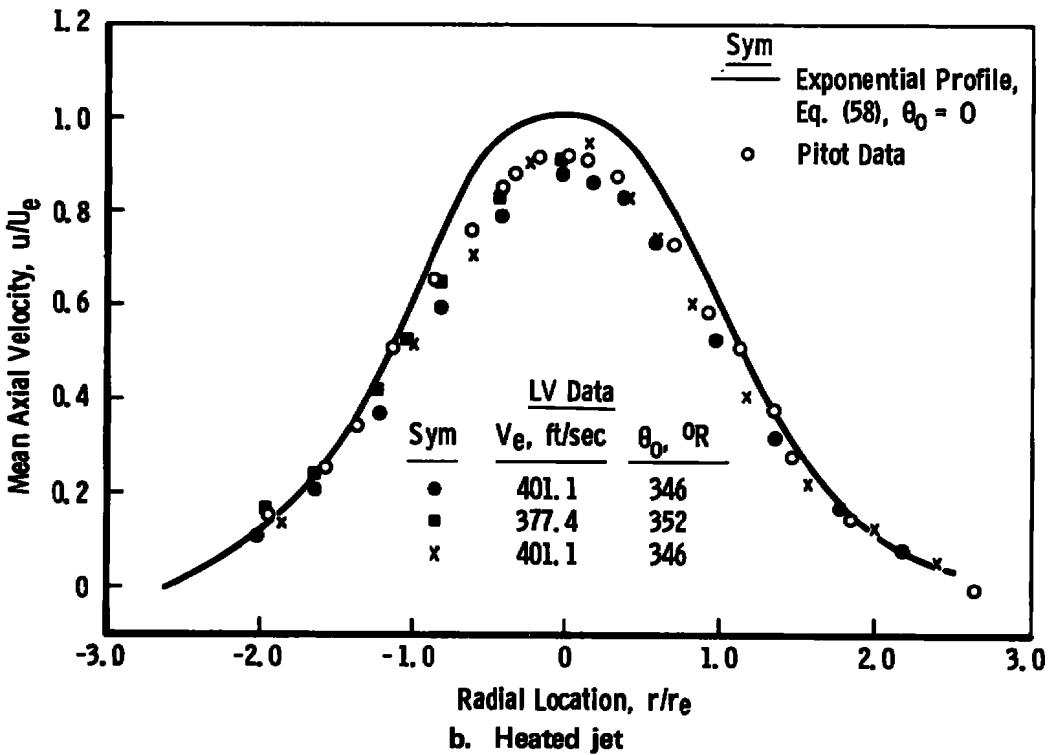
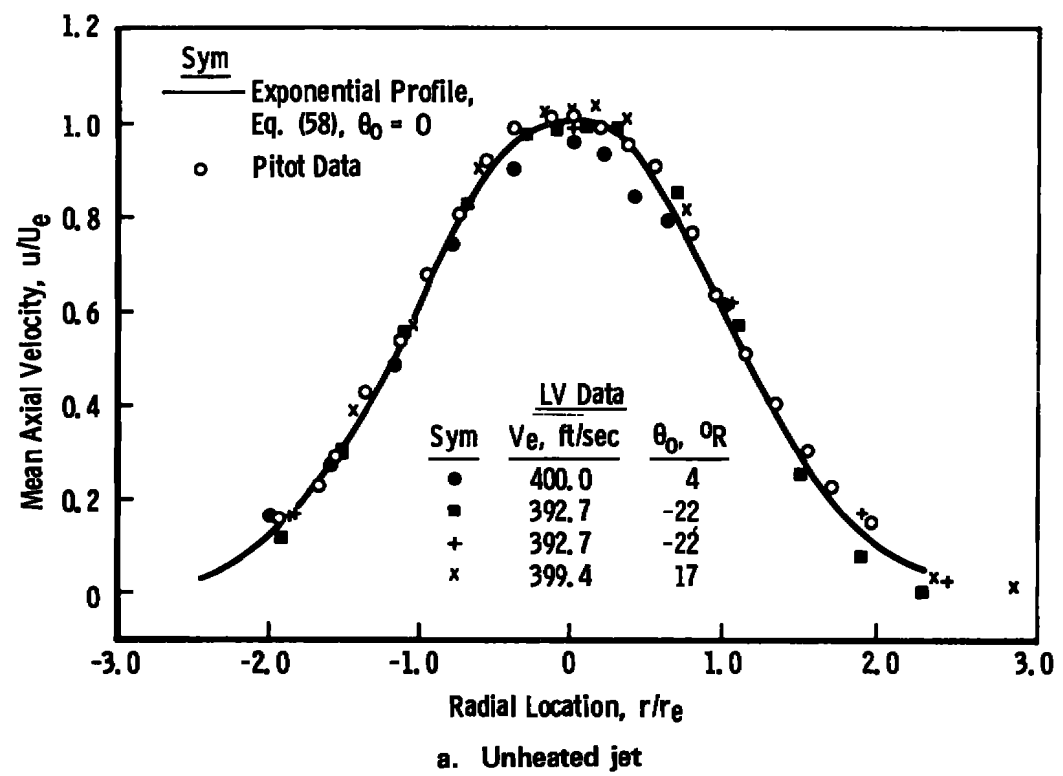
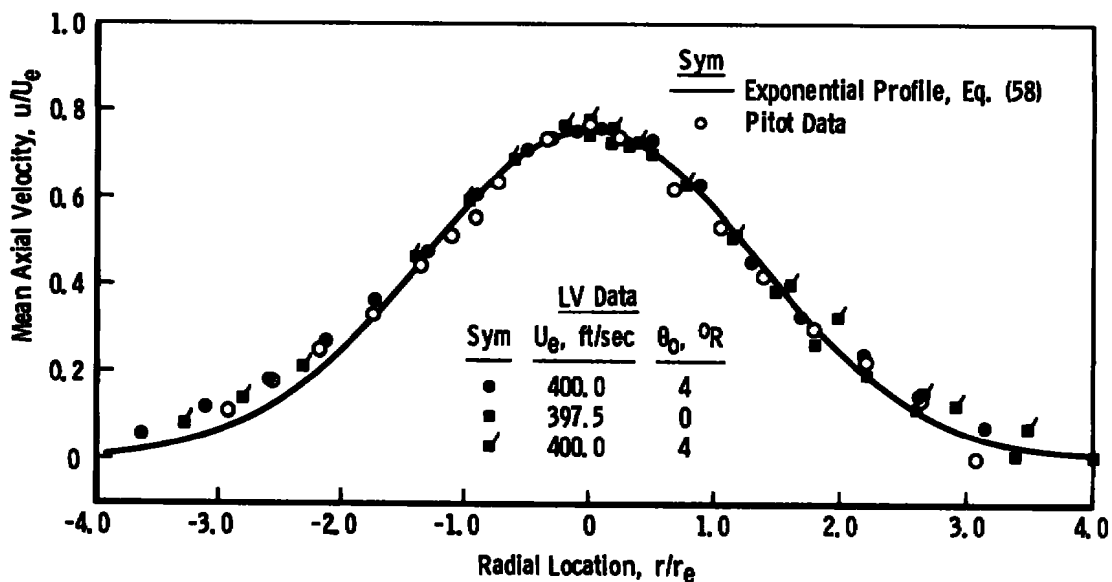
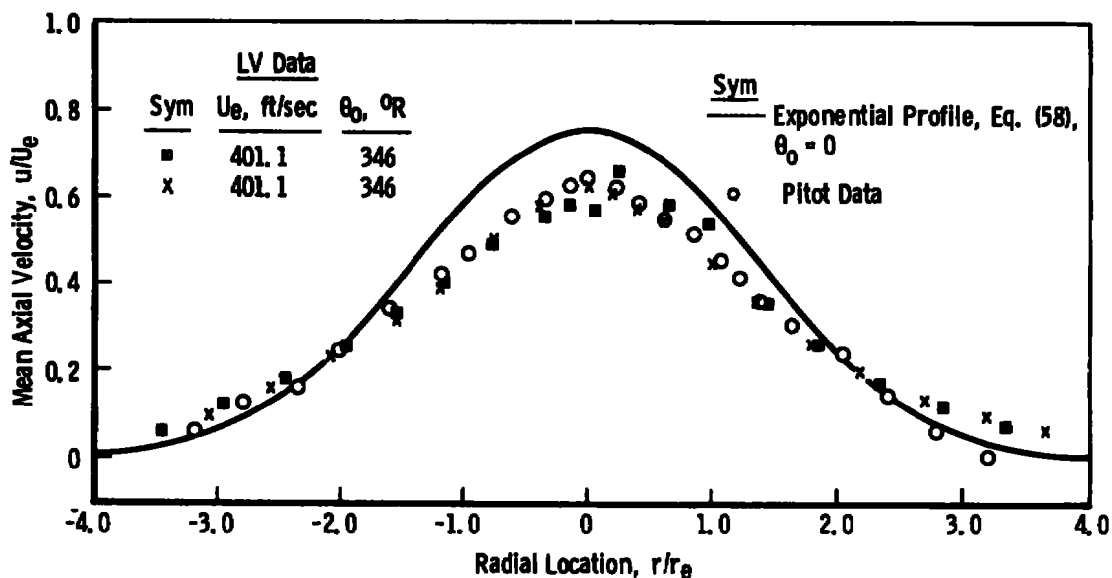


Figure 20. Axial velocity distributions at $X/D = 5$.

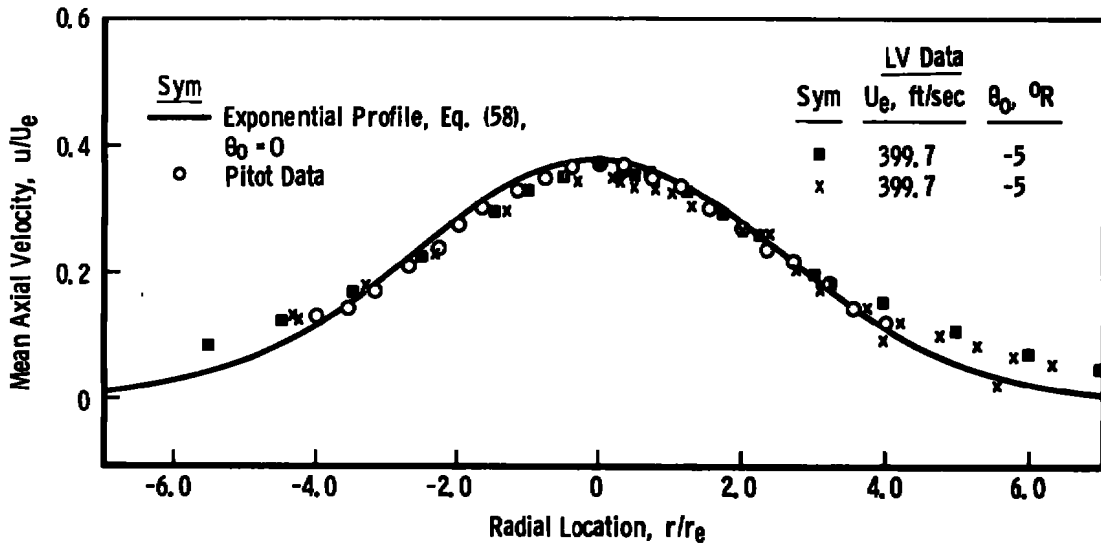


a. Unheated jet

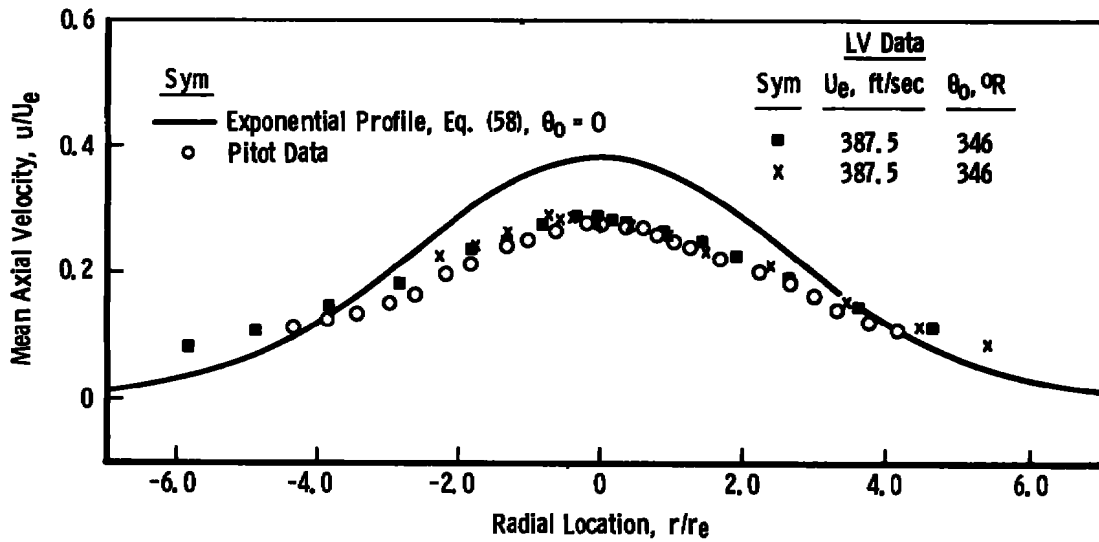


b. Heated jet

Figure 21. Axial velocity distributions at $X/D = 10$.



a. Unheated jet



b. Heated jet

Figure 22. Axial velocity distributions at $X/D = 20$.

The radial mean velocity across the unheated jet at $X/D = 2$ is shown in Fig. 23. From the uniform agreement of several sets of data in the core of the jet ($r/r_e \leq 0.5$), it is clear that the measurement of velocities near zero is not a problem for the LV system. Since the outflow from the interior of the jet is indicated by $v > 0$, the higher-than-theoretical velocities measured by the LV indicate a more rapid spreading of the jet than predicted from Eqs. (58) and (59). This same trend has been noted for hot-wire measurements of radial velocities (Ref. 41). Of particular interest is the qualitative agreement of the radial velocity measurements with Eq. (59). This implies that the present jet is more uniformly seeded than the jet of Ref. 12, where it was shown that

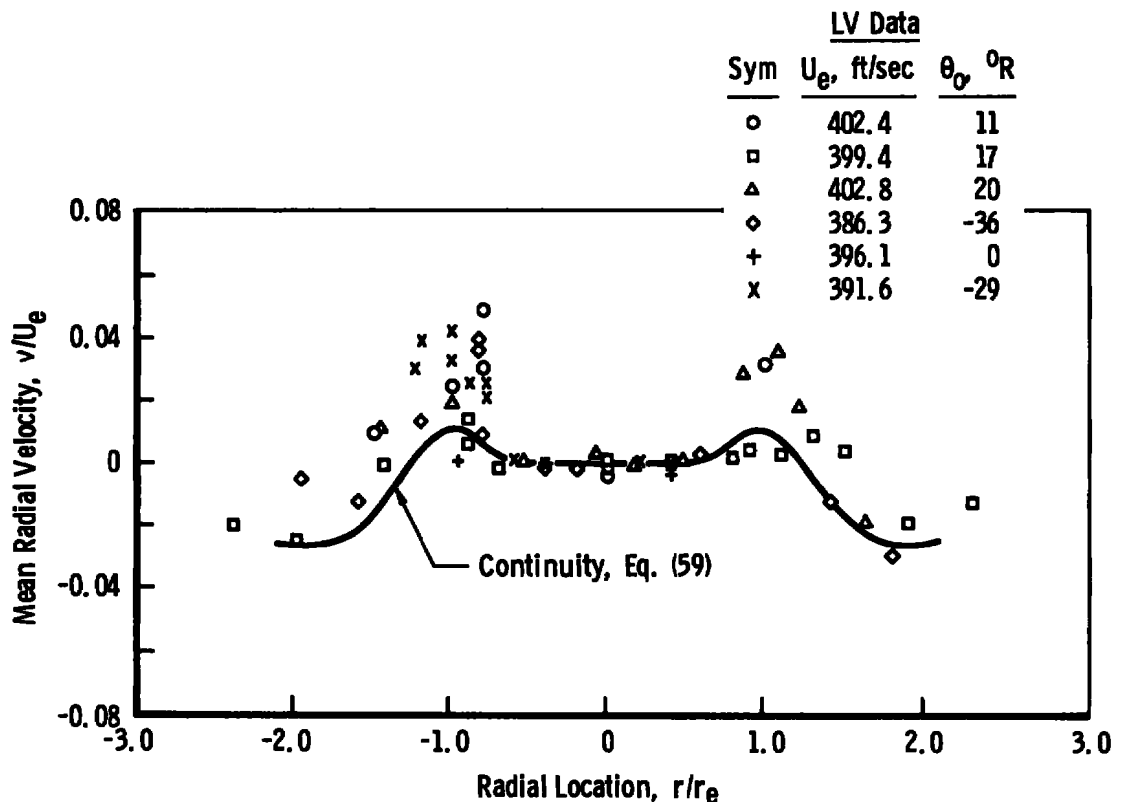


Figure 23. Radial velocity distribution in the unheated jet at $X/D = 2$.

LV measurements of an externally seeded jet will always exhibit negative radial velocities. The radial mean velocity measurements for $X/D = 5$, 10, and 20 are shown in Figs. 24, 25, and 26, respectively. It is seen that the amount by which the outflow velocities exceed the theoretical value diminishes at the downstream locations. Consequently, it appears possible that the seed concentration in the jet was initially higher near the centerline and the differences in concentration across the jet have been minimized because of the mixing between the jet and surroundings.

Tangential mean velocities for the unheated jet were measured but indicated the absence of swirl ($\omega \approx 0$) at all stations and are not presented. Neither radial nor tangential mean velocities are presented for the heated jet because of the misalignment problem discussed above.

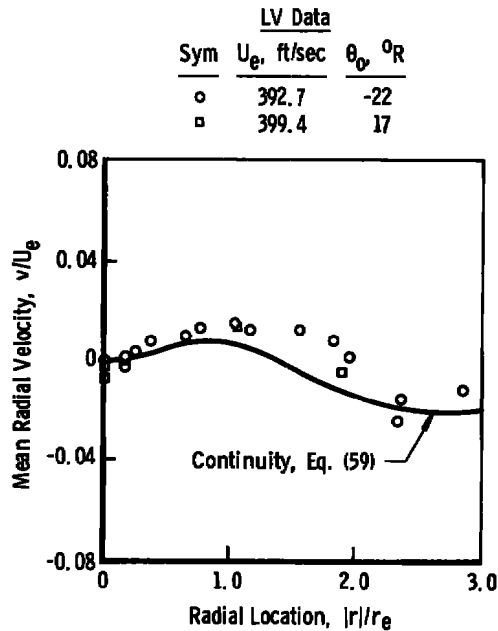


Figure 24. Radial velocity distribution in the unheated jet at $X/D = 5$.

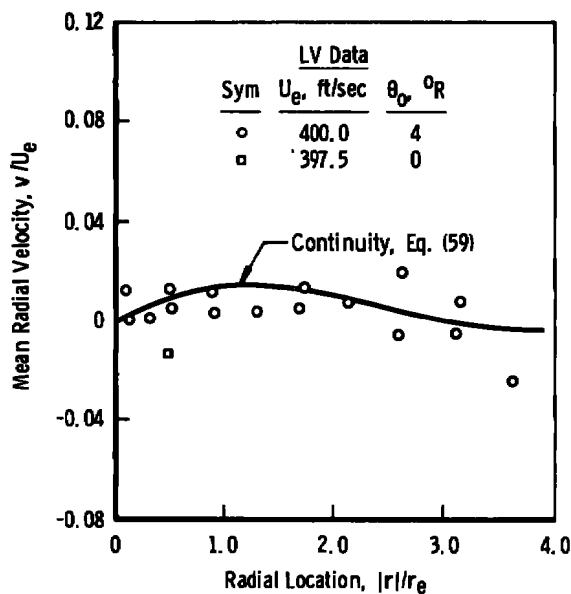


Figure 25. Radial velocity distribution in the unheated jet at $X/D = 10$.

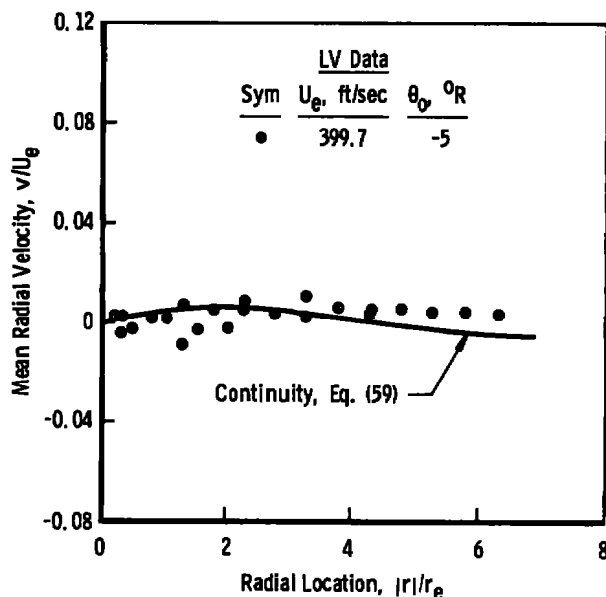


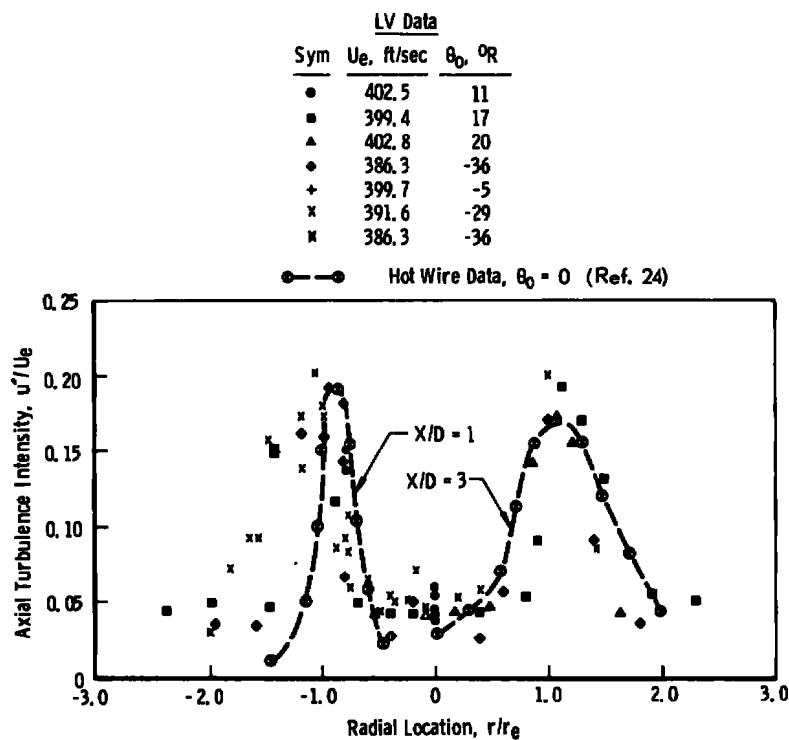
Figure 26. Radial velocity distribution in the unheated jet at $X/D = 20$.

4.3 TURBULENCE INTENSITY MEASUREMENTS

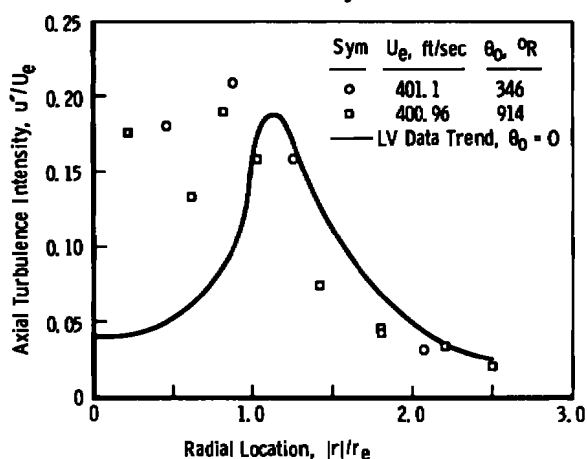
The distribution of axial turbulence intensities across a diameter of the jet for $X/D = 2$ are shown in Fig. 27. A comparison of the LV measurements to the hot-wire results of Ref. 24 shows comparable values of turbulence intensities although the LV-determined maximum shear and centerline values are somewhat higher. While differences in the experiments and particle dynamic effects could account for these differences, they are also characteristic of seeding nonuniformities (Section 3.4, Refs. 11 and 12). The scatter in the LV results for the heated flow (Fig. 27b) is contributed to by a smaller sample size and, consequently, a lower statistical confidence value (Section 2.5) than typifies the other data presented in this report. The use of smaller data sets at this station was necessary because of an extremely low data acquisition rate obtained at locations within $r/r_e < 1$. It is clear, nevertheless, that the centerline turbulence intensity is higher than obtained in the unheated flow although the results are comparable near the edge of the jet.

In Fig. 28a, the axial turbulence intensities obtained for several traverses of the unheated jet at $X/D = 5$ are compared to hot-wire data for $X/D = 6$. The data are in good agreement when the difference in axial stations is considered. The poor agreement on the centerline for one set of LV data could be due to misalignment, but as was shown in Ref. 12, nonuniform seeding of jet flows produces similar results. This leads to another

interpretation problem for the near-field heated-flow data (Fig. 27b and 28b) since the data rate was lowest near the centerline implying that the jet was nonuniformly seeded. When radial velocity data are available, this may be verified as discussed in Section 4.2, but misalignment precluded accurate radial velocity measurements. The heated jet data for $X/D < 10$ is thus of greater uncertainty near the centerline than near the jet periphery.

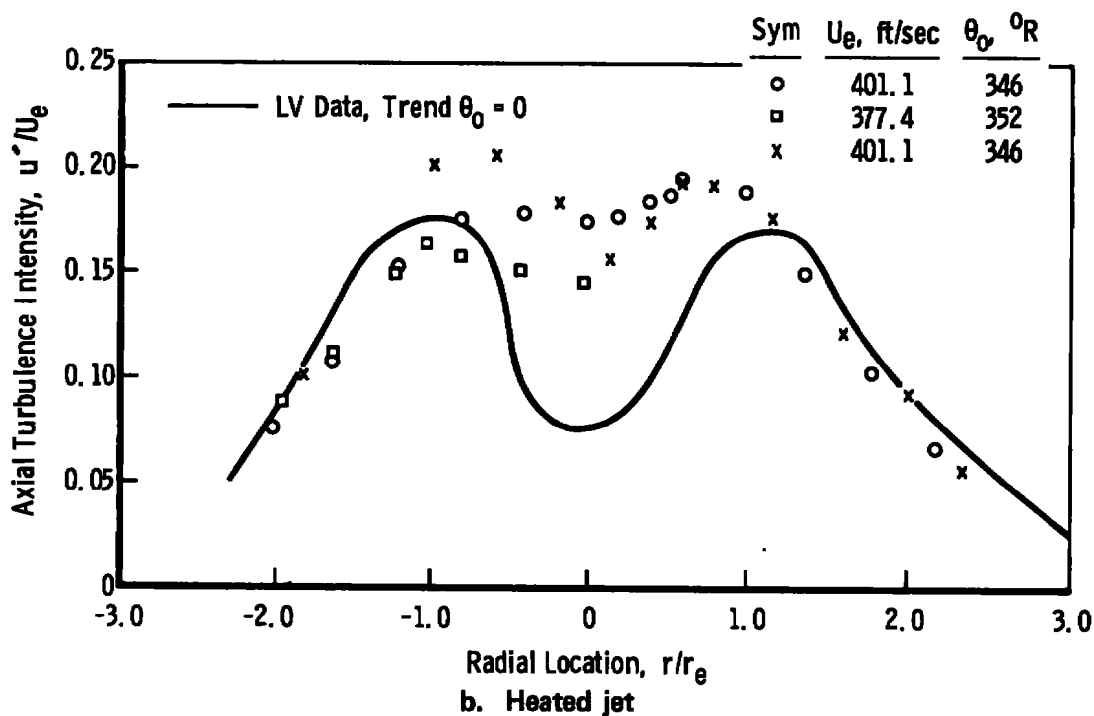
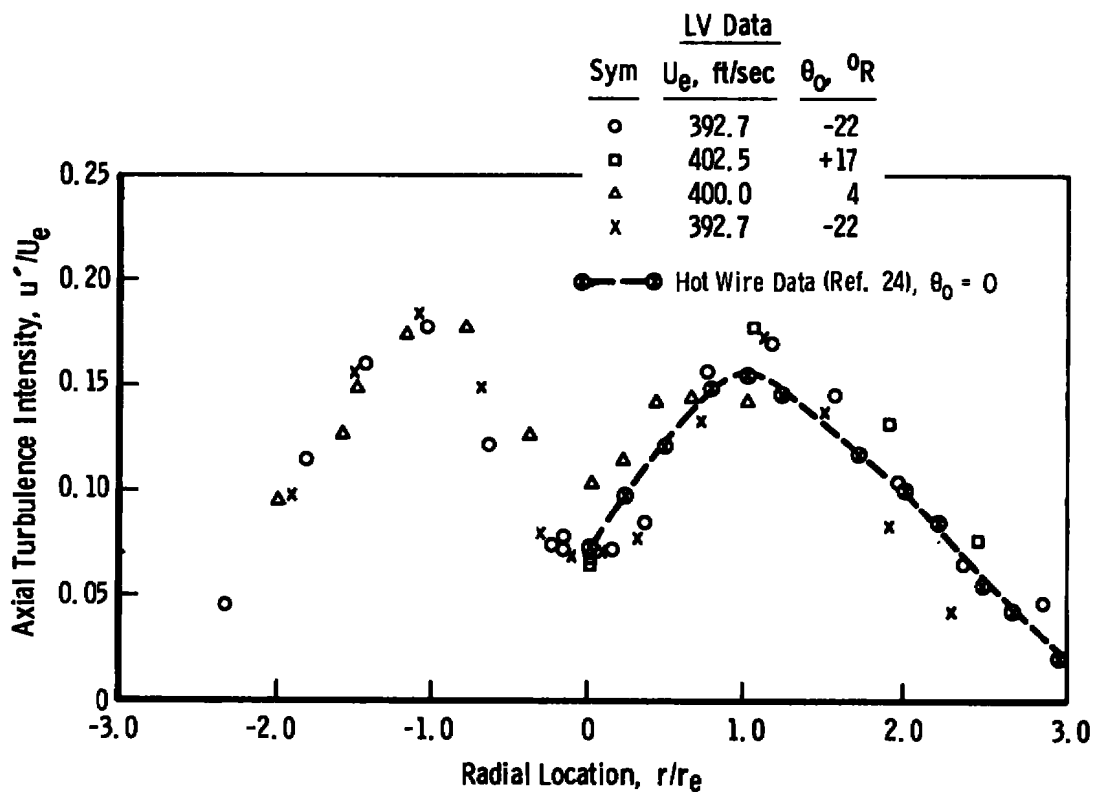


a. Unheated jet



b. Heated jet

Figure 27. Axial intensity distributions at $X/D = 2$.

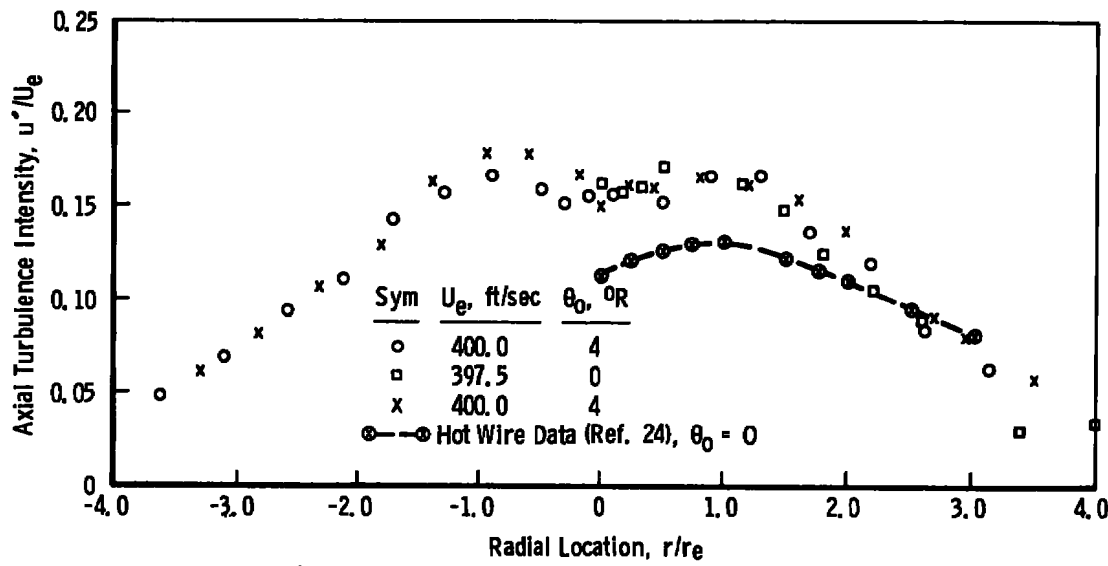
Figure 28. Axial intensity distributions at $X/D = 5$.

For $X/D = 10$ (Fig. 29), the unheated jet LV data indicate a higher axial turbulence intensity than the hot-wire data of Ref. 24 for $r/r_e \leq 2$. At this axial station, the analysis of Section 3.3 predicts that the centerline LV results should be influenced by particle dynamic broadening and overpredicts the intensity by as much as 4 percent. This is nearly the difference between the two sets of data. Also, at $X/D = 10$, the heated-flow turbulence intensities, which have been significantly higher than the cold flow near the centerline, are nearly equal to the unheated values. The axial turbulence intensities at $X/D = 20$ are compared to hot-wire data in Fig. 30. The data trends are similar to those noted at $X/D = 10$ except that the unheated jet now exhibits higher centerline intensities than the heated flow.

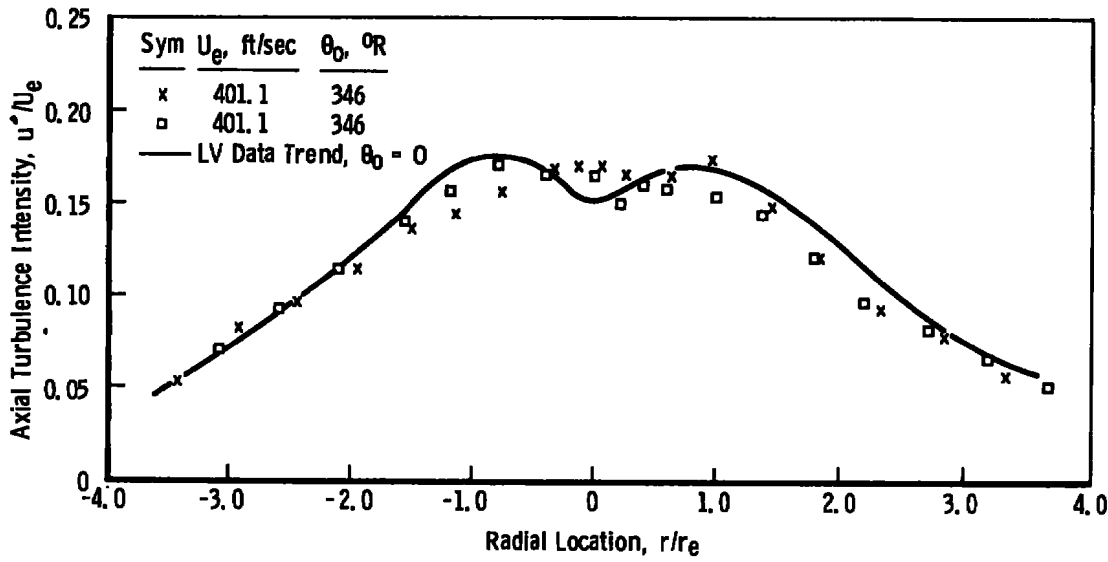
The radial turbulence intensity distributions are presented in Figs. 31 through 34 for axial stations of $X/D = 2, 5, 10$, and 20 , respectively. Detailed data for comparison to these results are not available. The trends, however, are similar to the axial results although of lower magnitude. Figures 35 through 38 present the variation of the tangential turbulence intensities at the four measuring stations. A horizontal traverse of the heated jet was not made at $X/D = 2$. In general, the tangential intensities measured for heated flows were greater than the corresponding radial intensities because of the horizontal misalignment of the LV as discussed in Section 4.1.

4.4 SHEAR STRESS

In Figs. 39 through 42, the normalized distribution of the shear stresses across the jet is presented. The unheated jet data are compared to the hot-wire data of Refs. 12 and 24. Reasonable agreement is obtained at all axial stations. Because of the extremely low data rate in the heated jet at $X/D = 2$, simultaneous data acquisition, which increases run times, was not attempted so that the shear stress could not be obtained. At $X/D = 5, 10$, and 20 , the heated and unheated jet shear stress distributions are similar in both magnitude and shape. It is somewhat surprising that these results should appear so reasonable in view of the inaccuracy in the measured turbulence intensities. It was observed in Ref. 12 that accurate shear stress values can be obtained near the centerline, although the turbulence intensity measurements are high, because the correlation $\overline{u'v'}$ approaches zero near the jet axis. Since the LV and hot-wire measurements are comparable for $r/r_e > 1$, then, in most cases a reasonable shear stress value is measured across the jet.

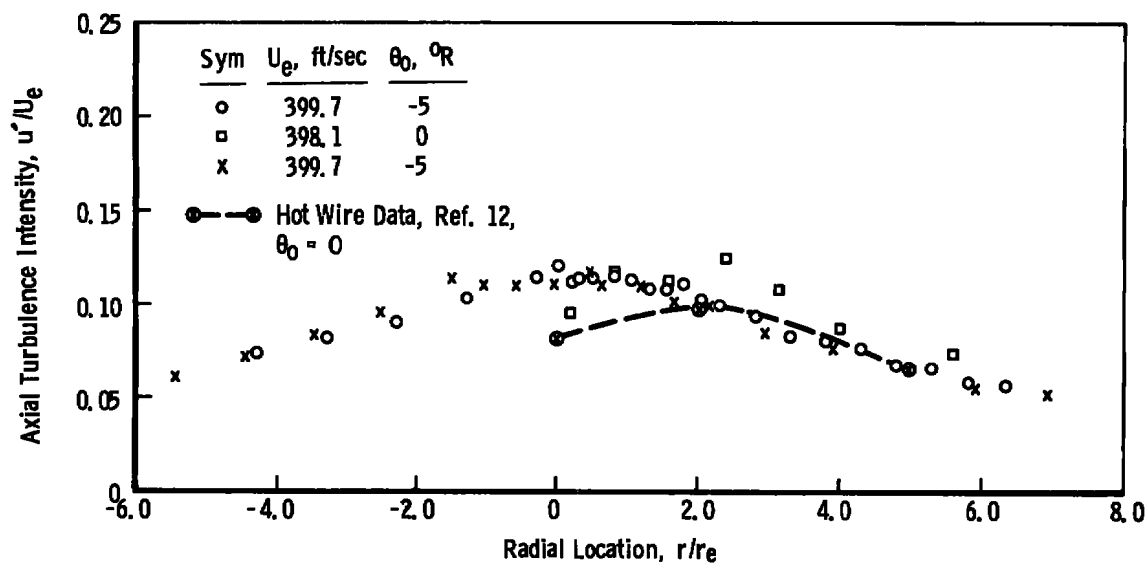


a. Unheated jet

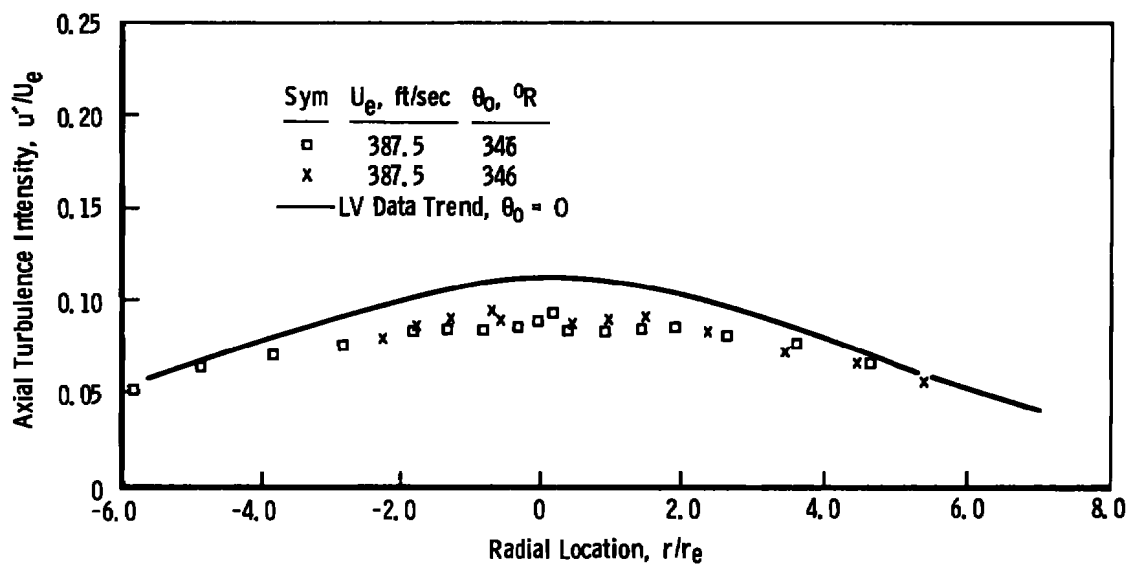


b. Heated jet

Figure 29. Axial intensity distributions at $X/D = 10$.

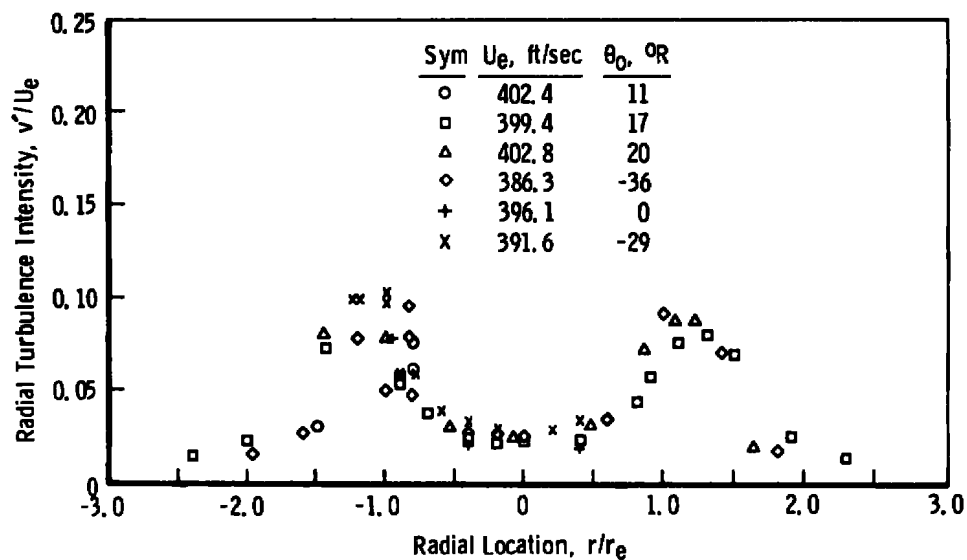


a. Unheated jet

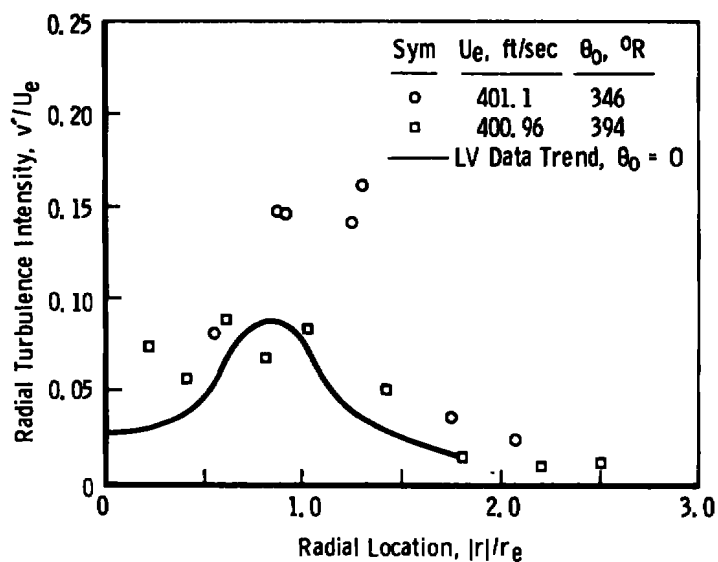


b. Heated jet

Figure 30. Axial intensity distributions at $X/D = 20$.

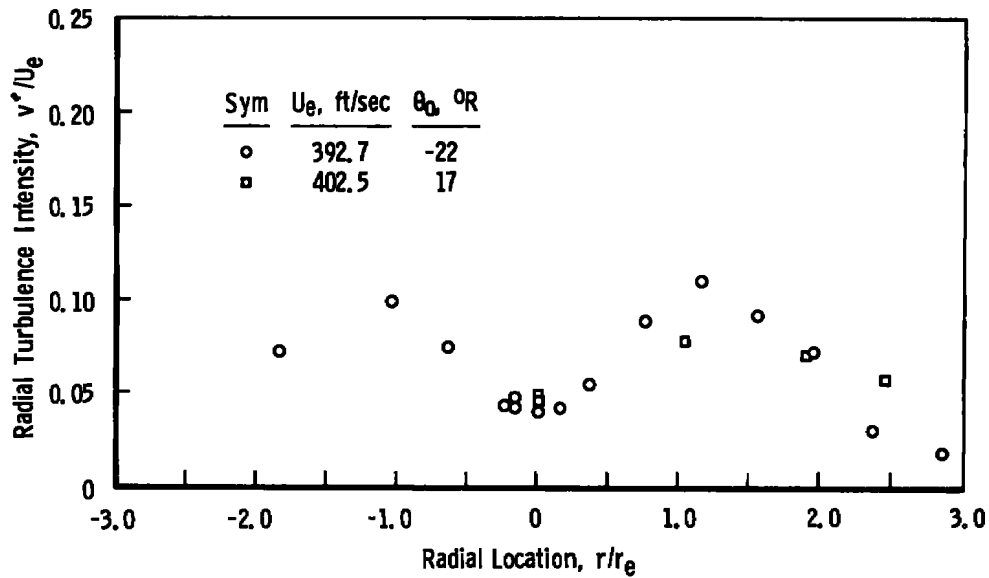


a. Unheated jet

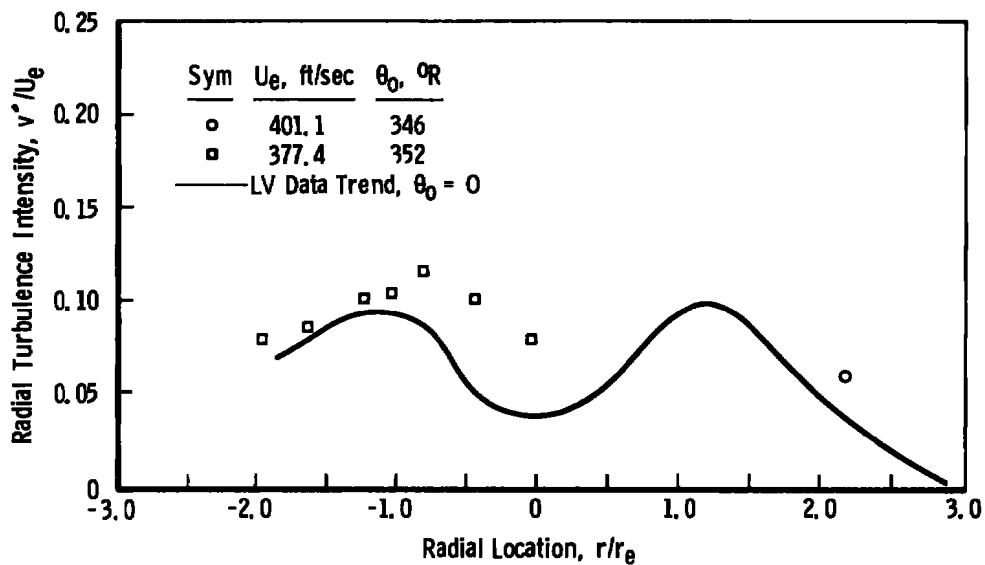


b. Heated jet

Figure 31. Radial intensity distributions at $X/D = 2$.

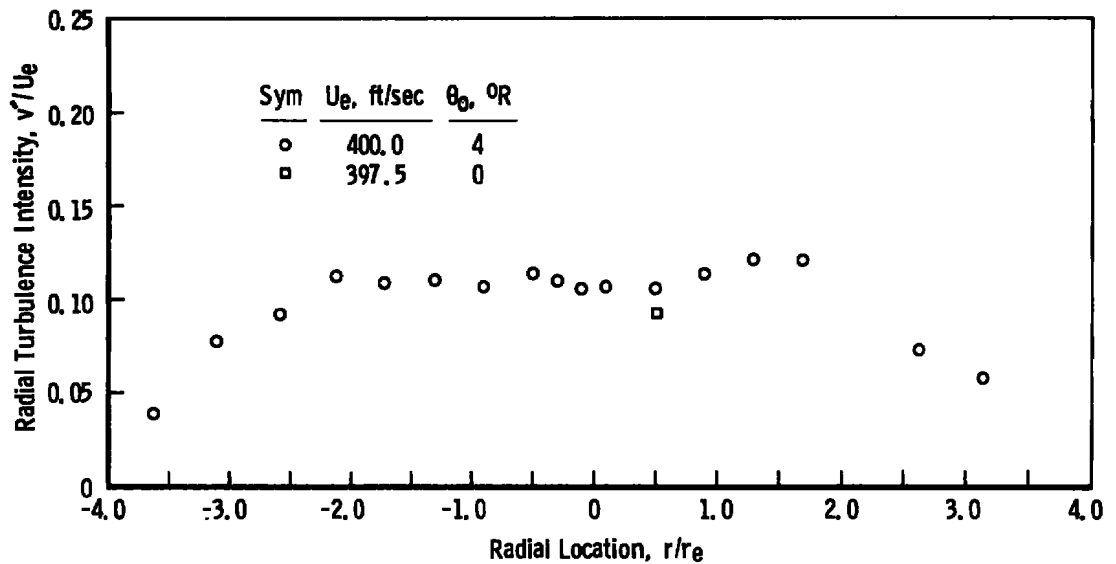


a. Unheated jet

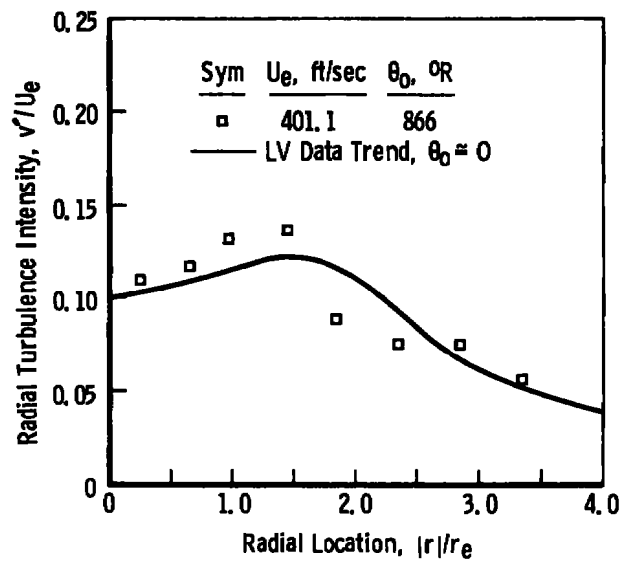


b. Heated jet

Figure 32. Radial intensity distributions at $X/D = 5$.

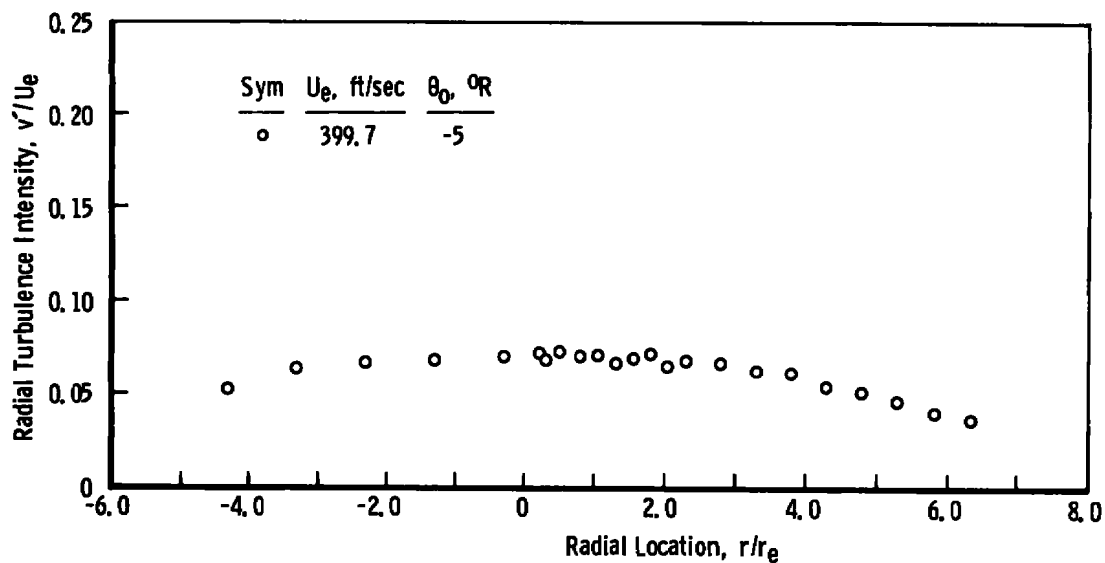


a. Unheated jet

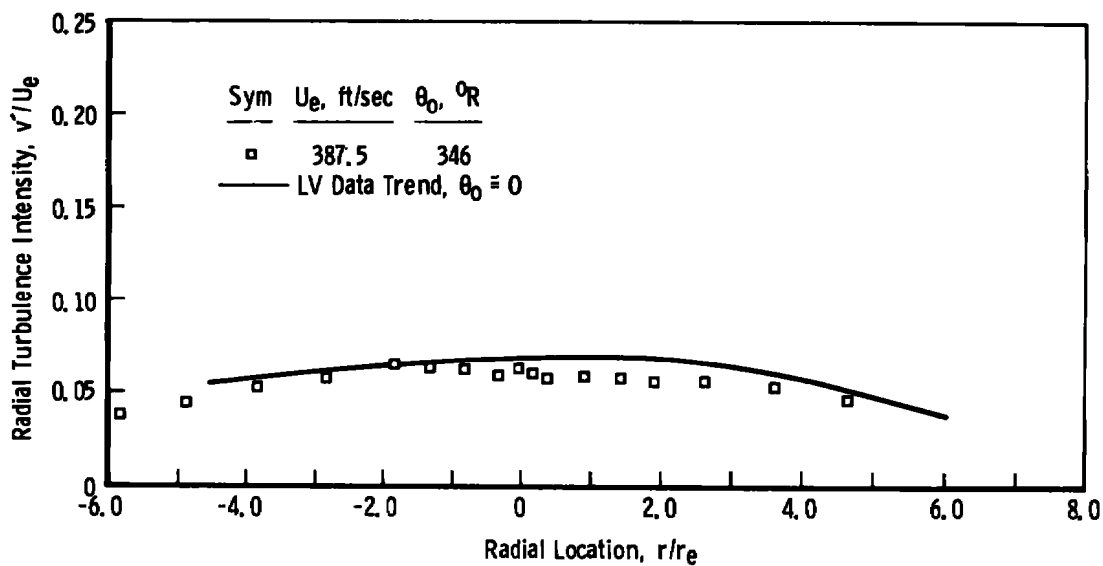


b. Heated jet

Figure 33. Radial intensity distributions at $X/D = 10$.



a. Unheated jet



b. Heated jet

Figure 34. Radial intensity distributions at $X/D = 20$.

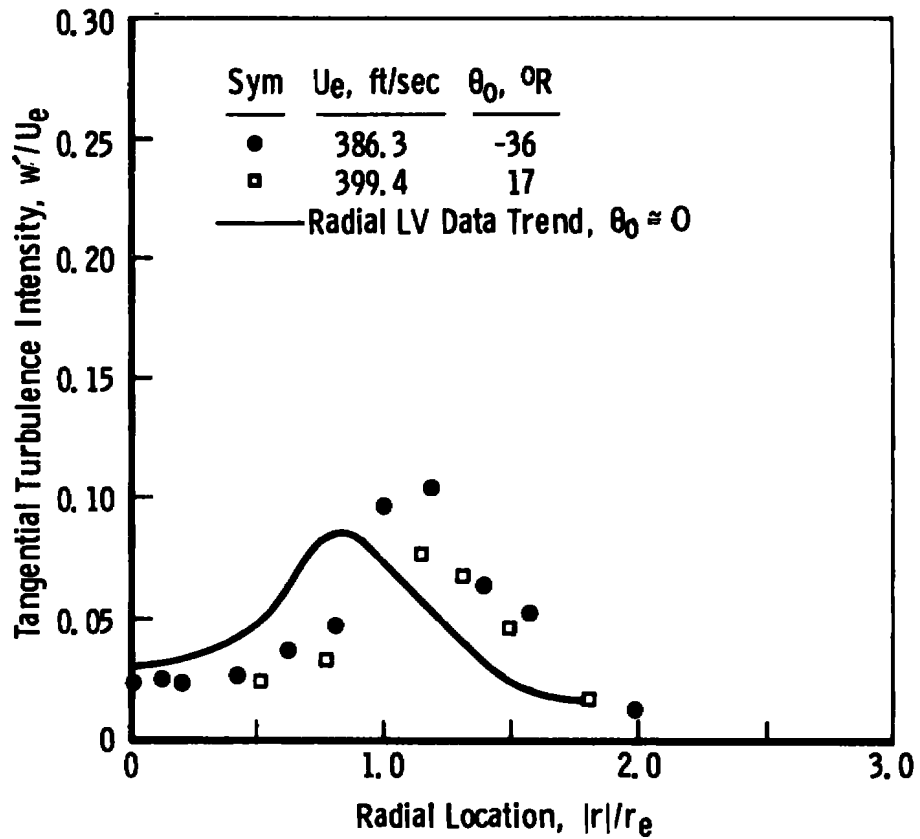
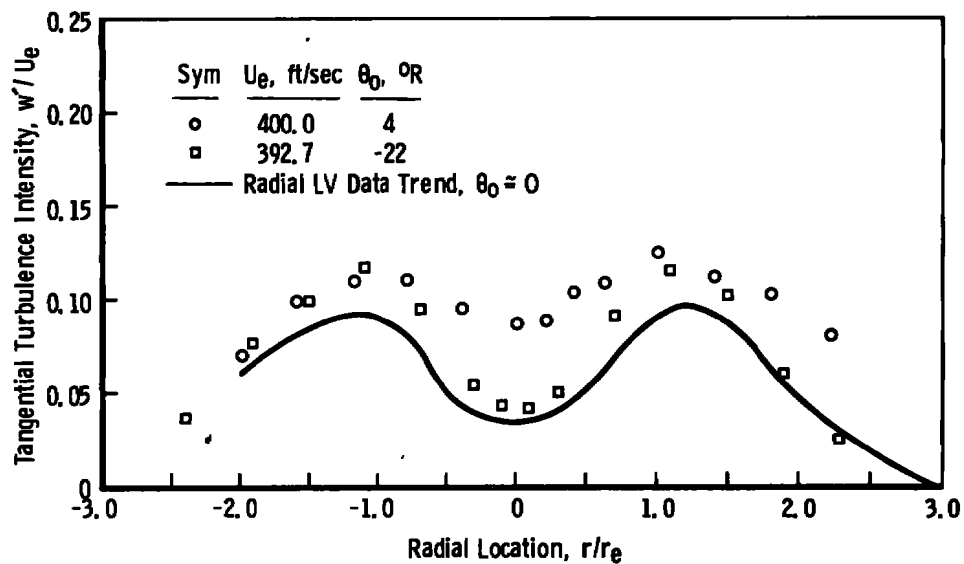
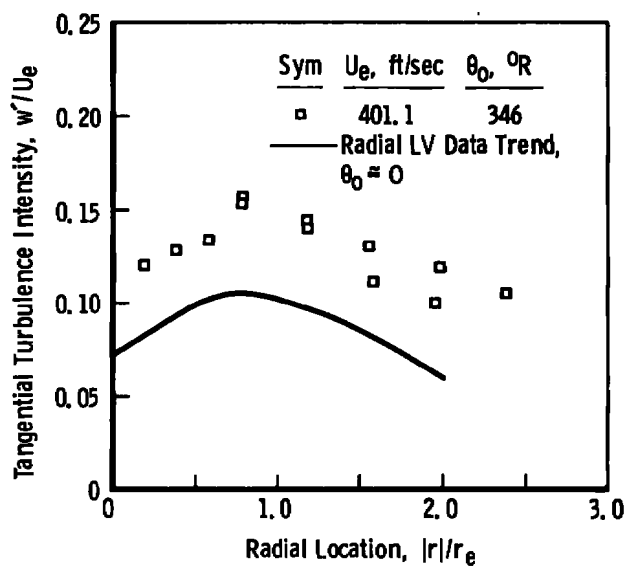


Figure 35. Tangential intensity distributions at $X/D = 2$ (Unheated).

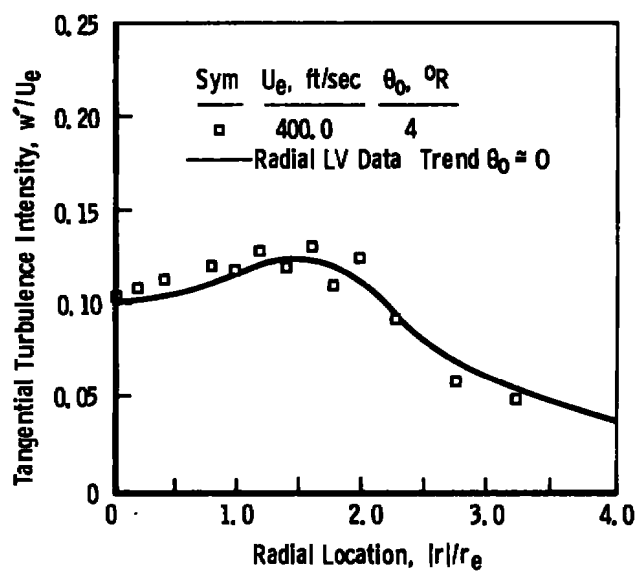


a. Unheated jet

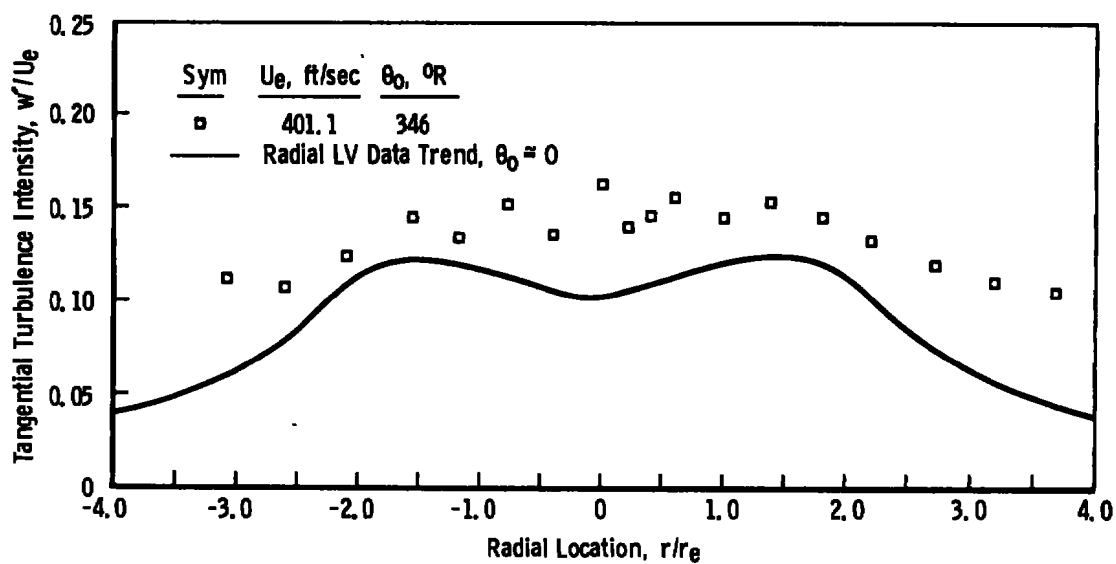


b. Heated jet

Figure 36. Tangential intensity distributions at $X/D = 5$.

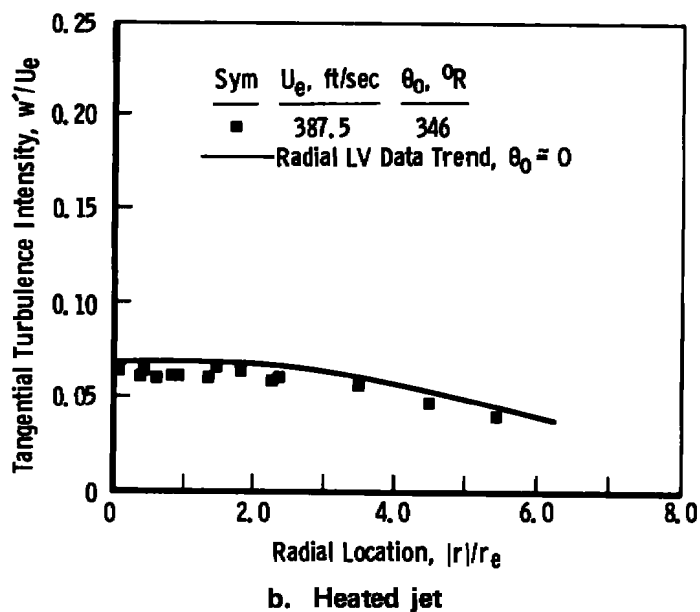
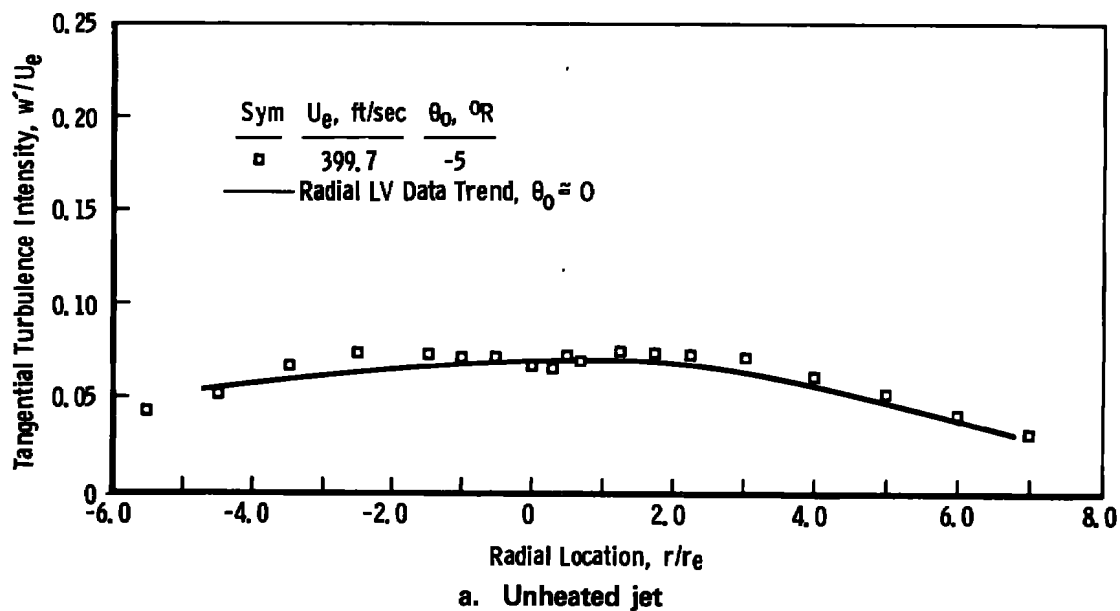


a. Unheated jet



b. Heated jet

Figure 37. Tangential intensity distributions at $X/D = 10$.

Figure 38. Tangential intensity distributions at $X/D = 20$.

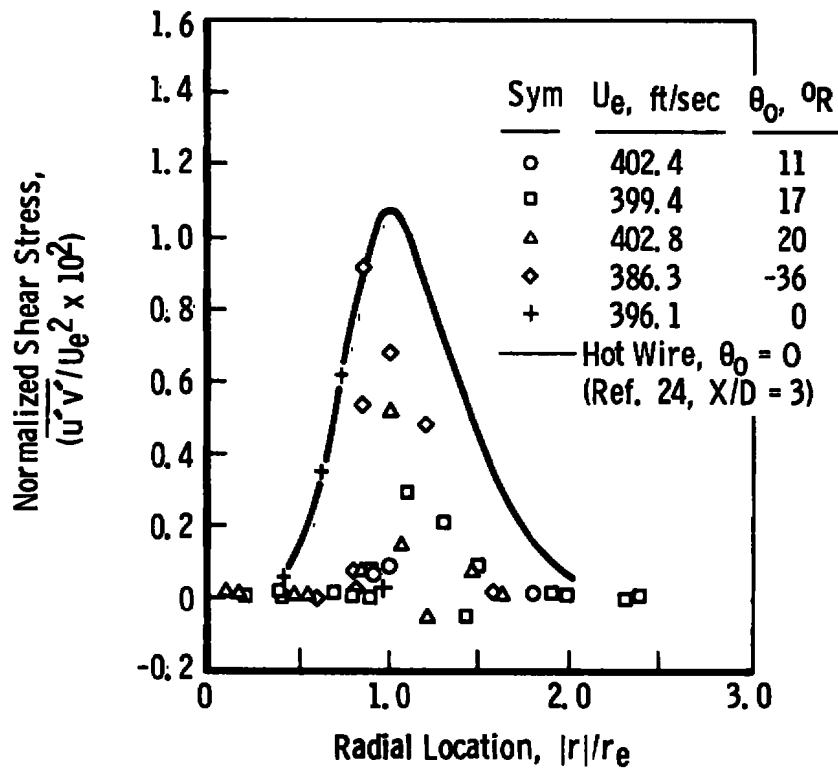
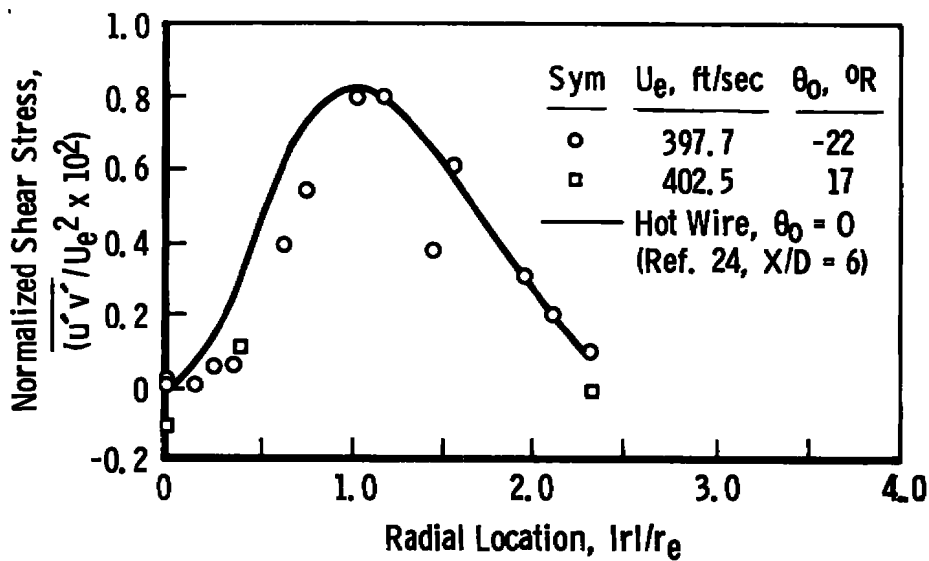
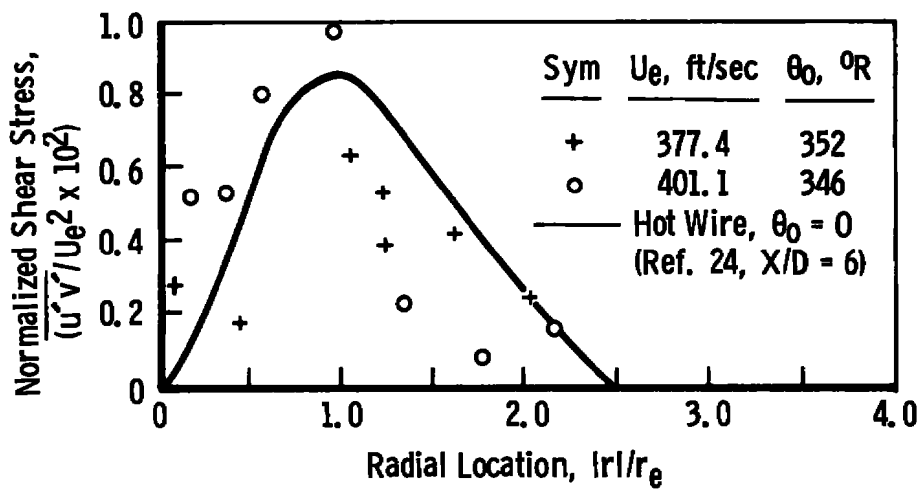


Figure 39. Shear stress distribution at $X/D = 2$ (unheated).

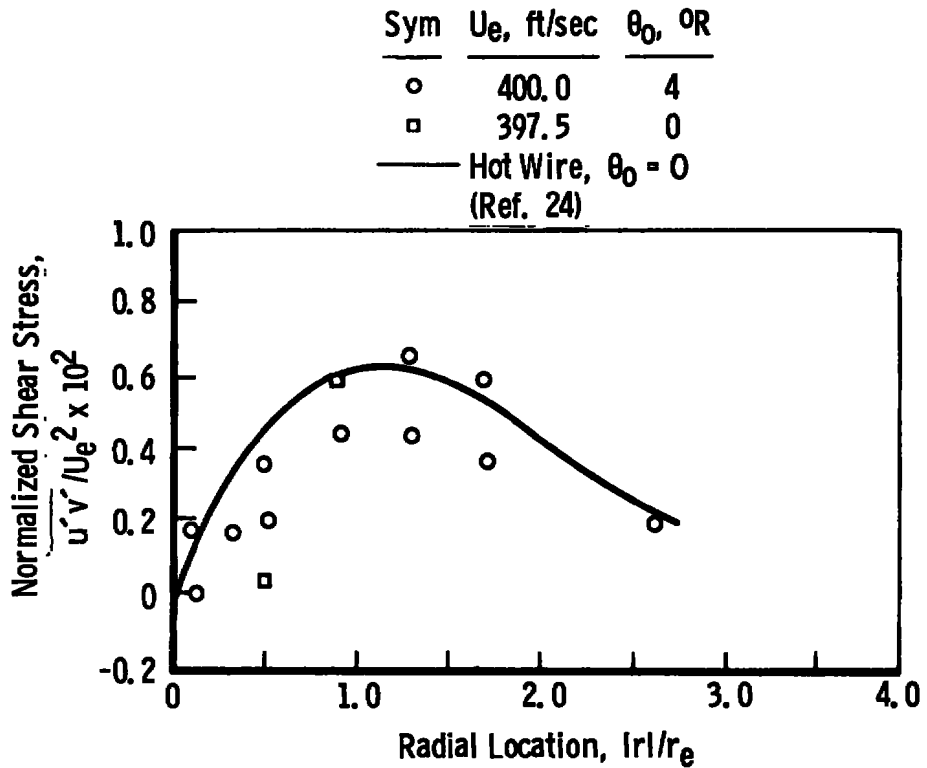


a. Unheated jet

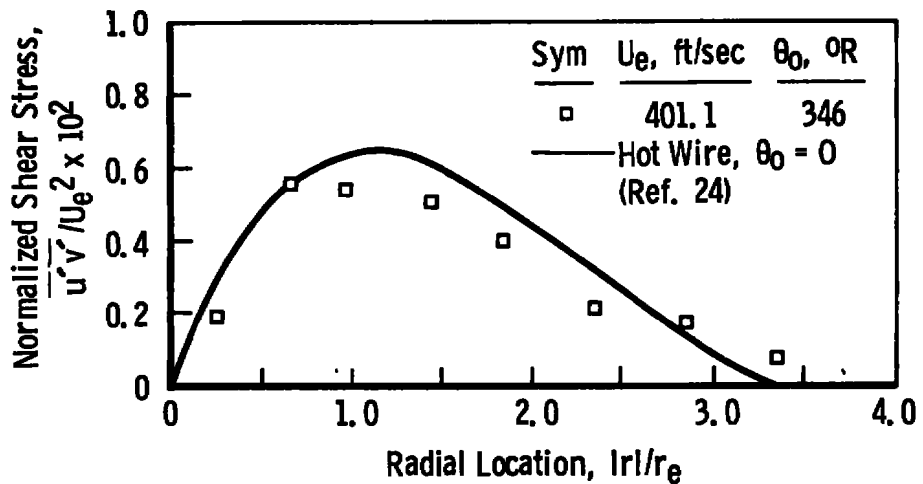


b. Heated jet

Figure 40. Shear stress distributions at $X/D = 5$.

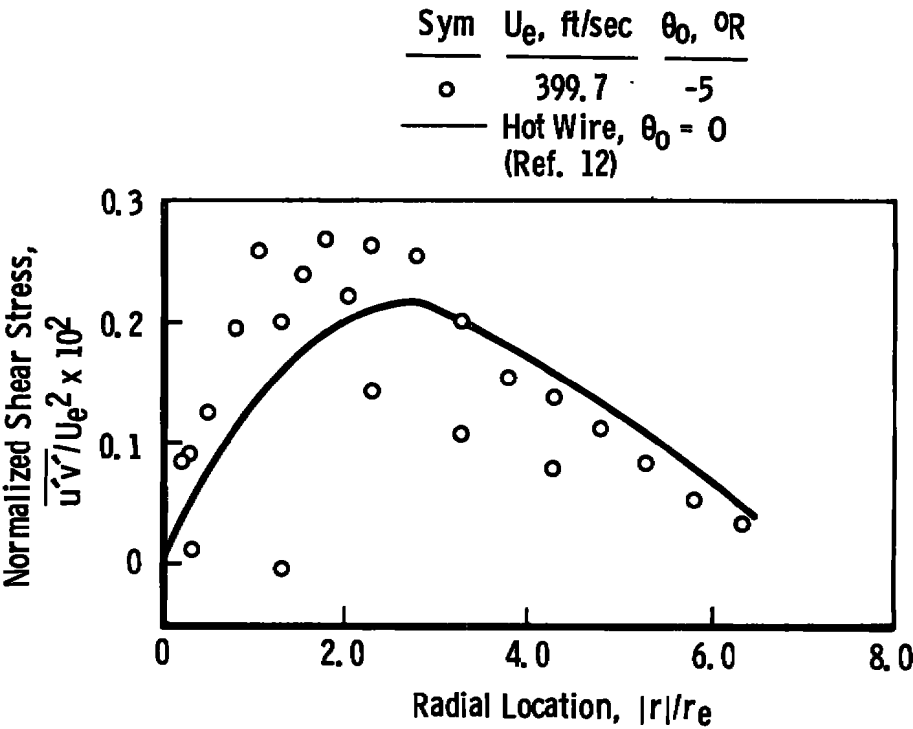


a. Unheated jet

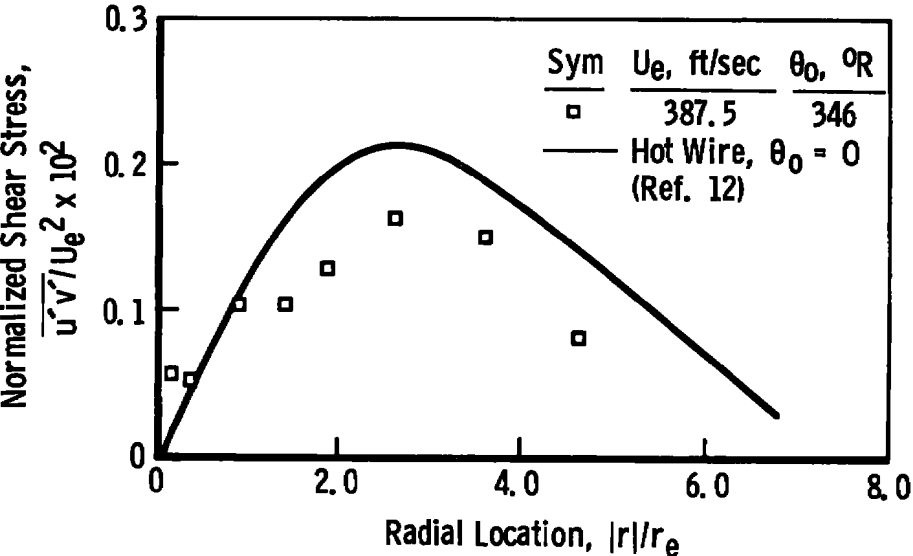


b. Heated jet

Figure 41. Shear stress distributions at $X/D = 10$.



a. Unheated jet



b. Heated jet

Figure 42. Shear stress distributions at $X/D = 20$.

4.5 VELOCITY PROBABILITY HISTOGRAMS

Histograms of LV axial velocity measurements obtained at three radial locations for $X/D = 2$ are shown in Fig. 43. These results are representative of other locations. The velocity increment (ΔU) used in forming the histograms was one-third of the measured rms velocity so that the three histograms are not similarly normalized. On the centerline, $r/r_e = 0$, the distribution of velocities is nearly Gaussian which is typical of data obtained in the core of jets. The indicated turbulence intensity (5 percent) exceeds that predicted from the particle dynamic broadening analysis (approximately 1 percent, Fig. 10) and does not exhibit the predicted skew, thus indicating the presence of velocity fluctuations not considered in the theory. Near the maximum shear location, $r/r_e = 1$, the histogram exhibits a significant broadening as would be expected because of the greatly increased turbulent mixing at that location. At the point $X/D = 2$, $r/r_e = 2$ lies beyond the boundary of the jet as determined from the pitot measurements of Fig. 19. Consequently, the mean axial velocity is nearly zero, and the distribution is Gaussian because of the nearly random particle motion at that location. The local turbulence intensity at $r/r_e = 2$ is over 600 percent of the mean velocity. The histogram clearly demonstrates the desirability of employing Bragg-diffracted LV systems in regions of high turbulence intensities since nearly half of the measurements were obtained from particles having negative axial velocity components.

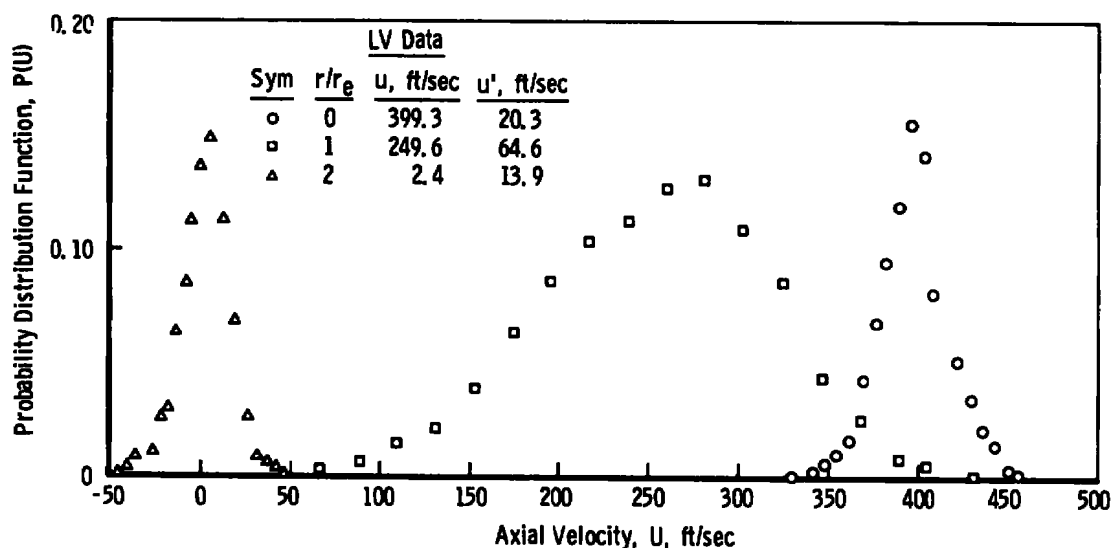


Figure 43. Velocity probability distributions at $X/D = 2$ (axial component).

In Fig. 44, the histograms at $X/D = 2$ are shown for the radial and tangential velocity data for the three radial locations. The centerline data were obtained from separate horizontal and vertical traverses of the jet and illustrate the repeatability of the results when the system could be accurately aligned with the jet centerline. At $r/r_e = 1.0$, both distributions are broad due to the increased intensity of the velocity fluctuations near the peak shear location. Near $r/r_e = 2$, both the radial and tangential velocity distributions show that the majority of the measurements were obtained from particles having negative velocities.

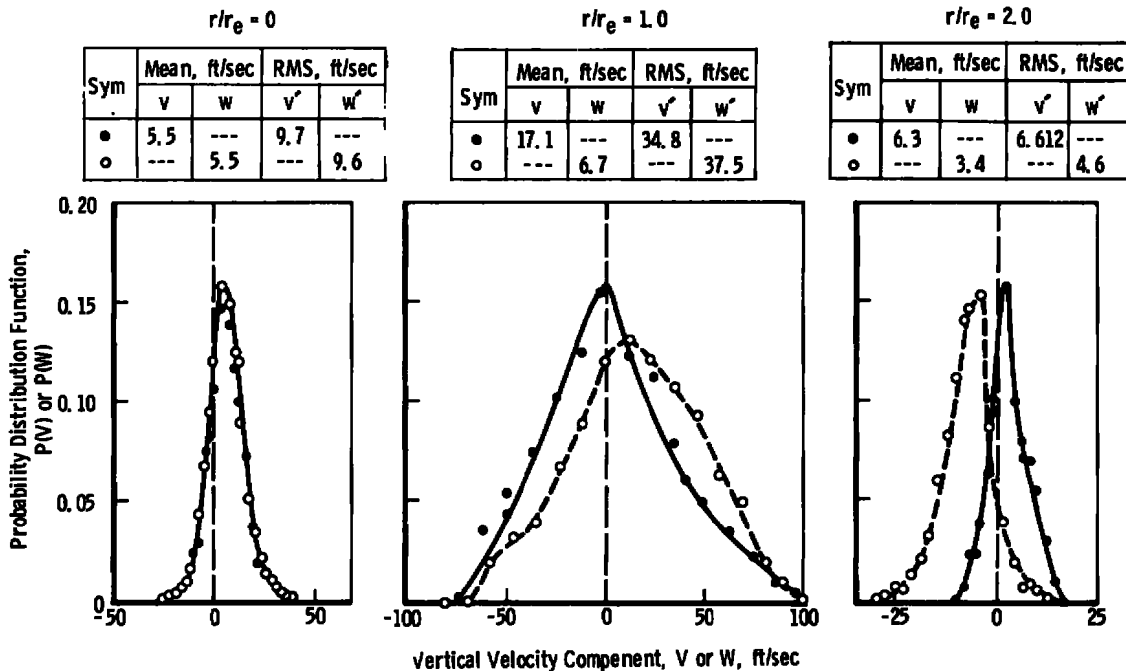


Figure 44. Velocity probability distributions at $X/D = 2$ (vertical components).

5.0 UNDEREXPANDED JET RESULTS

Pitot and LV measurements of the flow along the centerline of an essentially sonic nozzle exhausting into still air were made at values of nozzle exit-to-ambient static pressure ratios (P_e/P_∞) of 2.0, 3.0, 4.0, and 5.0 at stagnation temperatures of 500 and 1,000°R. Shadowgraphs were also made of the flow to determine the locations of the boundary shocks and Mach discs in the jet nearfield. The LV data were taken at axial stations within the range $0.25 \leq X/D \leq 5.0$. Pitot measurements could be used to compute velocities only in the region upstream of the Mach disc since no attempt was made to measure the local static pressure. An indication of the velocity downstream of

the first Mach disc was obtained, however, by matching the pitot data to the theory of Ref. 26 in the vicinity of the shock.

Figure 45 shows a shadowgraph of the flow downstream of the nozzle exit for $P_e/P_\infty = 2.0$. The rectangular obstructions seen in the photograph at the exit plane are bolts forming part of the baseplate structure. While the bolts prevented the shadowgraph system from viewing the entire flow, they did not interfere with the flow development since they were located well outside the plume boundaries. The curved shock just downstream of the exit plane occurs because of the machining irregularities in the nozzle that were noted in Section 2.1. Near $X/D = 1$, the boundary shock waves intersect, and the incipient formation of a Mach disc is seen. It may be inferred from the figure, moreover, that additional shock-wave crossings occur on the centerline near $X/D = 2.5$ and 4.0. For $P_e/P_\infty = 4.0$ (Fig. 46), a well-developed primary Mach disc occurs near $X/D = 1.73$ and a second Mach disc is seen at $X/D = 3.39$. Mach disc locations, determined from shadowgraphs, are given in Table 4 as a function of pressure ratio. For the pressure ratios that will be considered in this section, the primary shock locations are found to agree within 2 percent of those given by Ref. 42 so that the nozzle shock apparently had only a slight influence on the subsequent development of the plume.

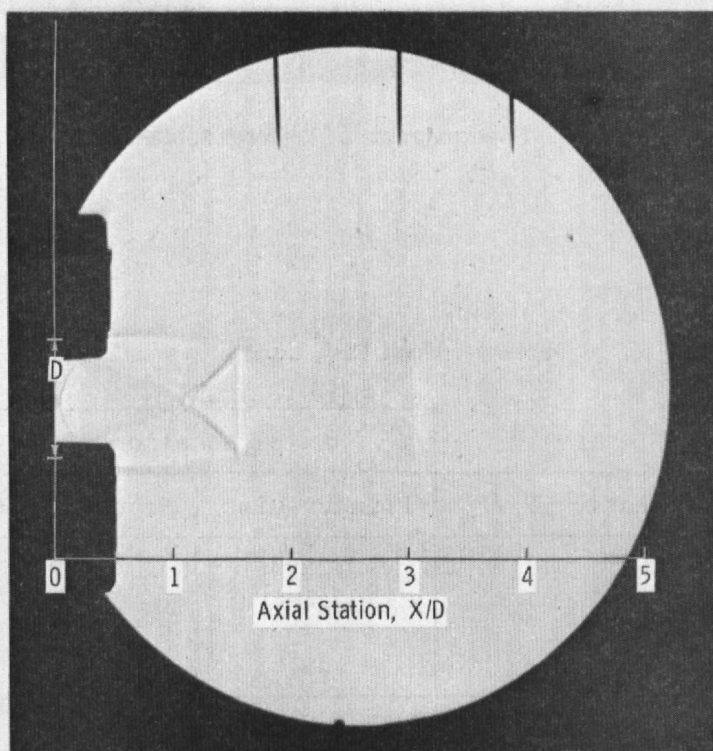


Figure 45. Shadowgraph of underexpanded jet, $P_e/P_\infty = 2$.

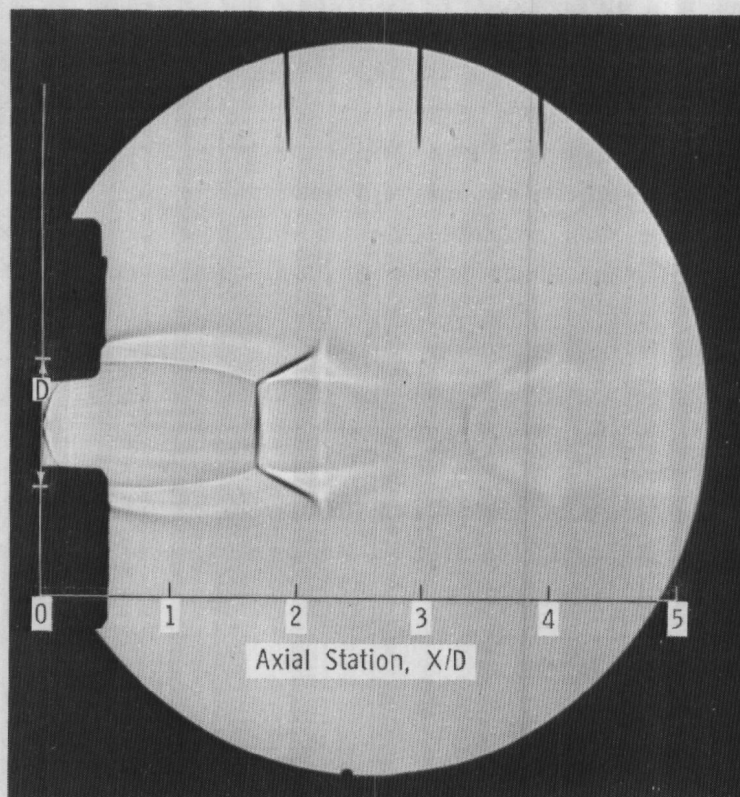


Figure 46. Shadowgraph of underexpanded jet,
 $P_0/P_\infty = 4$.

Table 4. Mach Disk Locations

Pressure Ratio, P_0/P_∞	Axial Location, X/D	
	Primary Disc	Secondary Disc
2	1.08	2.62
3	1.48	3.05
4	1.73	3.39
5	1.97	3.60

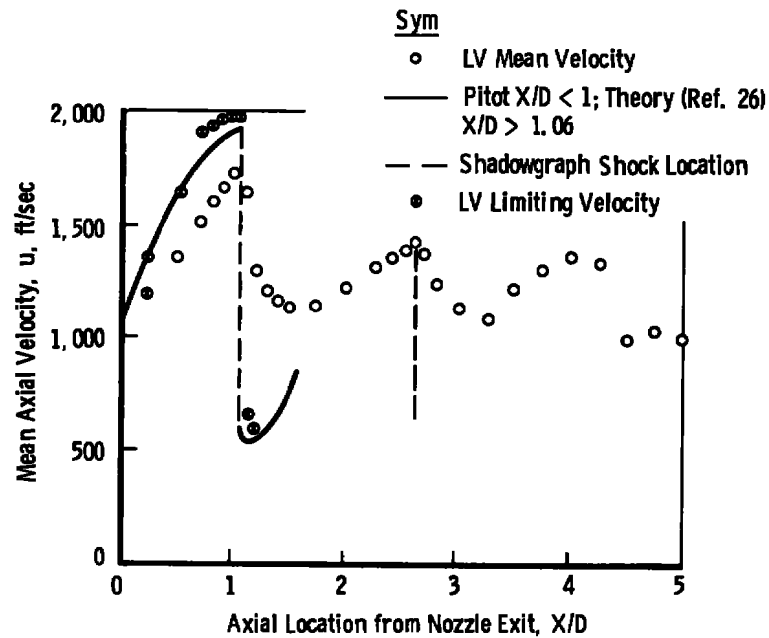
With the preceding information on shock structure and the nozzle geometry, a qualitative description of the axial-flow conditions may be deduced. In the 1.50 in. from the settling chamber to the nozzle exit, the flow is accelerated from about 5 ft/sec to Mach 1.1, where the nozzle irregularities cause a weak shock wave to form. The velocity change across the exit shock is, from one-dimensional flow considerations, about 20 percent of the local flow velocity although the total pressure recovery is near unity. Following the shock wave, the flow expands rapidly to a Mach number near 3.0 at the first Mach disc location, then decreases to a few hundred ft/sec and reaccelerates until a second Mach disc is formed. This process is repeated until dissipative mechanisms in the flow preclude further attainment of supersonic velocities. It is evident that the successive accelerations and decelerations in the underexpanded jet can produce appreciable particle lags so that this flow field provides an extremely severe test of the ability of an LV to obtain meaningful data in naturally seeded flows.

5.1 MEAN AXIAL VELOCITY

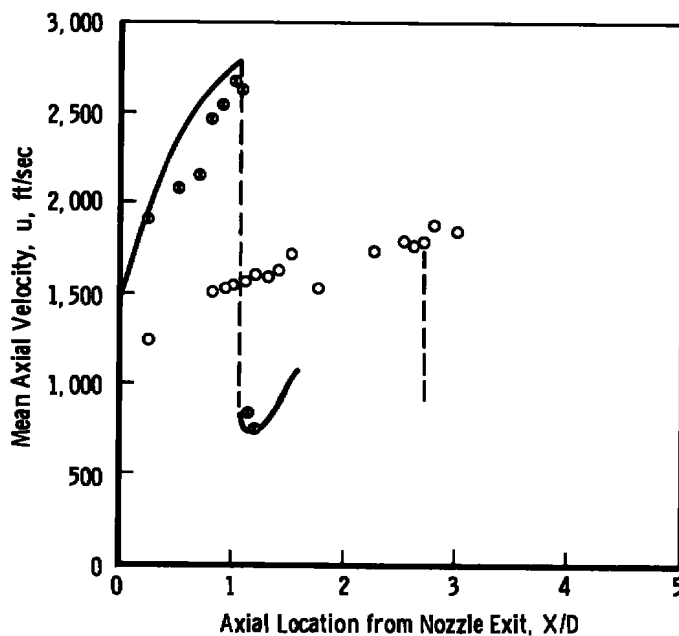
A comparison of LV mean centerline velocity measurements to the pitot/theoretical values is presented in Fig. 47 for the plume corresponding to $P_e/P_\infty = 2.0$. In the cold jet, the LV data and centerline velocity distribution have similar shapes although the magnitude of the LV measurements is clearly low ahead of the primary Mach disc location and high downstream of the shock wave. From Fig. 5, the velocity lag at the shock location corresponds to a particle having a diameter of about $2\ \mu\text{m}$ if its density is 2 g/cc. From Fig. 8, an LV having 30- μm fringe spacing will have a maximum probability of detecting a particle in the 2- to 3- μm range. The LV velocity measurements, therefore, are consistent with the results to be expected from particle dynamic effects and the present optics. It is also interesting that the LV accurately predicts the shock location in the unheated jet despite its failure to obtain the proper velocity. In the heated flow, on the other hand, the LV results show little similarity to the gas velocity field. Low signal-to-noise ratio signals obtained in the heated flows necessitated operation at an elevated trigger level thus causing the data set to be biased more toward the larger particle sizes than in the colder flow case.

Figure 48 presents the mean velocity comparisons at a pressure ratio of $P_e/P_\infty = 4.0$. Again, the LV measurements indicate lower mean velocities than those derived from pitot measurements in regions of the rapid acceleration and indicate higher velocities downstream of the shock waves. The location of a shock, however, is well-defined in both jets by the change in slope at that position. For a pressure ratio of 4.0, the primary Mach disc diameter is approximately half the nozzle diameter (Fig. 46) so that probe volume misalignment with the centerline was not sufficient to place the probe volume outside the shock cell. The second Mach disc is much smaller in diameter, however, so

that a centerline shift of 0.1 in. could cause it to be missed. Misalignment, then, may contribute to the LV-indicated location of the second shock wave in the heated jet data at $P_e/P_\infty = 4.0$.

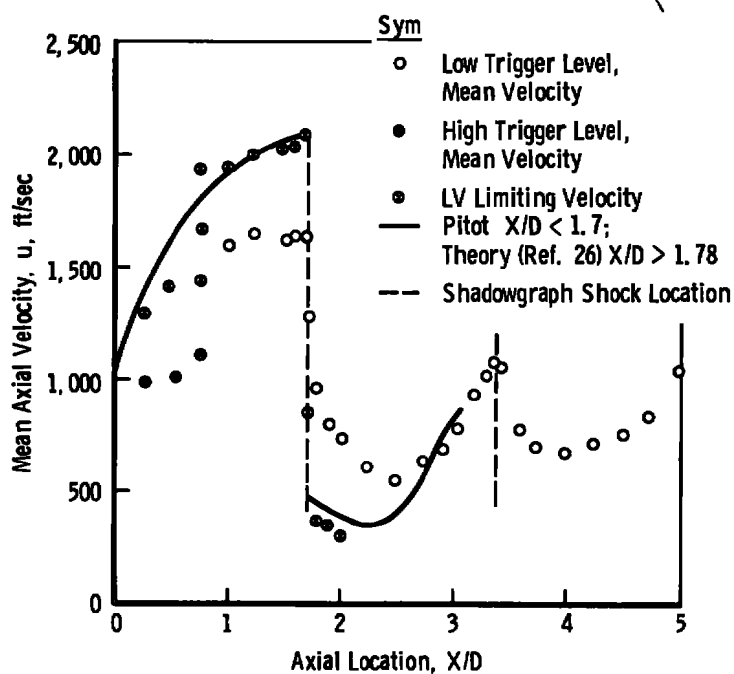


a. $T_0 = 502^\circ R$

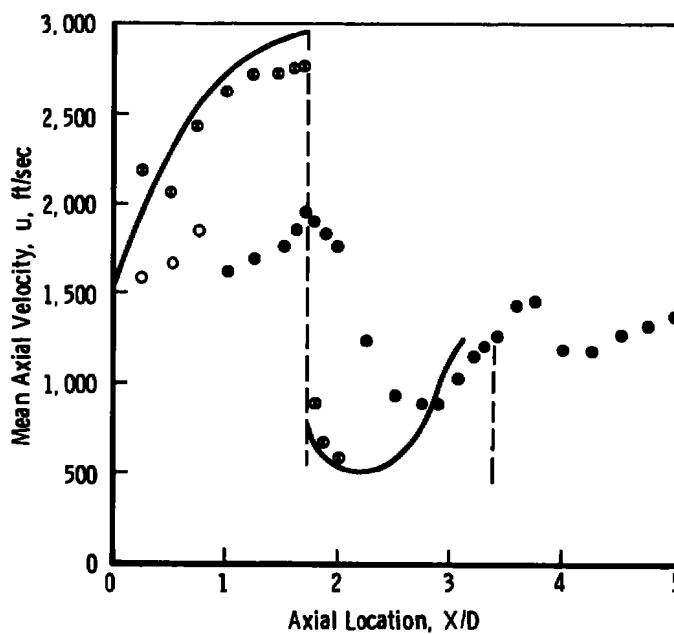


b. $T_0 = 980^\circ R$

Figure 47. Centerline axial velocity variation,
 $P_e/P_\infty = 2$.



a. $T_O = 485^\circ R$



b. $T_O = 997^\circ R$

Figure 48. Centerline axial velocity variation, $P_0/P_\infty = 4$.

The profound influence that the trigger level and, hence, minimum particle detection threshold can have is clearly illustrated in Fig. 48. Particle lag calculations for locations upstream of the primary Mach disc imply that the cold-flow results are representative of a 3- μm particle having a density of 3 g/cc. The discontinuity in the slope of the unheated jet LV velocity data at $X/D = 0.75$ is due to a reduction in trigger level that was possible at that station since reflected radiation from the nozzle baseplate was no longer interfering with the burst signals. A similar observation can be made for the heated jet except that an excessively high trigger level was maintained throughout the traverse, then the points in the vicinity of the nozzle exit plane were obtained at a lower trigger level. It is clear that the results obtained in the unheated jet could have been improved if a means existed for quantizing the trigger level or if immediate reduction of the acquired data had allowed an iteration on trigger level to allow its optimization. Both of these features are desirable for future test operations in naturally seeded flows.

In general, the mean velocity measured by the LV in naturally seeded flows provides an unsatisfactory measurement of the gas velocity if the velocity field has extremely high accelerations. It was noted in Section 3.3 that some improvement in the results would be obtained by using the mode of the velocity probability distribution as a velocity indicator. It will be seen below that this would have been very arbitrary for the present data because of the complex nature of the measured histograms. An alternate criterion suggested in Section 3.3 was to use the maximum velocity detected by the LV as a gas velocity indicator in accelerating flows and the minimum detected velocity in deceleration regions. One difficulty in this approach is that it is difficult to define the "tails" of a probability distribution without having large data sets. Furthermore, noise or turbulence may be the dominant factors in determining the value of the P.D.F. as it approaches zero. It is, nevertheless, convenient to anticipate the results of Section 5.2 to evaluate this technique. For this purpose, histograms of the data sets comprising the data points were formed in 0.1-MHz (12-ft/sec) intervals. The limit of the distribution was chosen as that velocity for which the distribution became discontinuous. That is, although higher velocities may have been indicated in an acceleration region, such velocities were separated from the main data set by velocities for which $P(U_k)$ was identically zero.

Velocities thus defined are denoted in Figs. 47 and 48 as limiting velocities for the flow. It is seen that such limiting velocities are always within 15 percent and are generally within 5 to 7 percent of the gas velocity derived from pitot measurements. The results, moreover, are much less sensitive to trigger level than is the mean (or mode) of the distribution. Use of such a technique, however, requires qualitative knowledge of the flow-field characteristics, low turbulence levels, and relatively noise-free signals. It is, therefore, not a generally acceptable substitute for measurements made with particles of known size and density.

5.2 VELOCITY PROBABILITY DISTRIBUTIONS

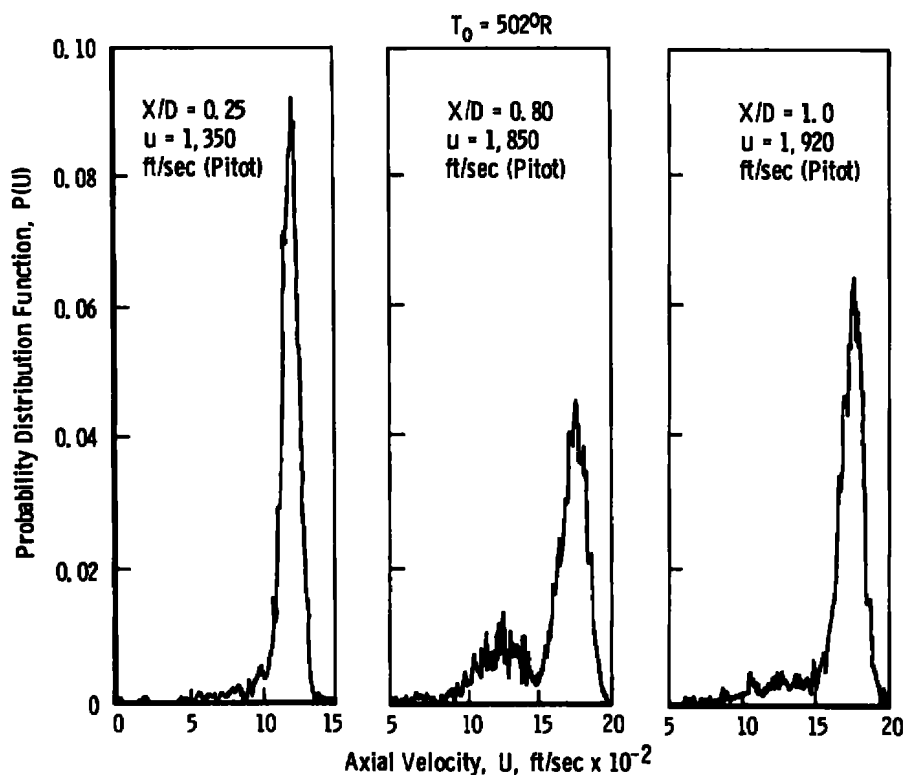
The velocity histograms for the data obtained at locations upstream of the primary Mach disc for the unheated jet at $P_e/P_\infty = 2$ are shown in Fig. 49a. Of particular interest is the tendency of the histogram toward a bimodal structure at the $X/D = 0.8$ location. The negative skew of the distribution at each axial position indicates that the flow is accelerating. Downstream of the shock (Fig. 49b), the distribution is nearly Gaussian at $X/D = 1.20$ indicating that both accelerating and decelerating particles are present. (It is assumed for this discussion that the flow is essentially laminar.) By $X/D = 1.5$, the velocity distribution is again skewed negatively implying that an acceleration region has been encountered. Immediately upstream of the second Mach disc location, $X/D = 2.5$, the histogram again tends toward a bimodal structure.

Histograms for the heated flow at $P_e/P_\infty = 2.0$ are shown in Fig. 50. The distributions in the acceleration zone ahead of the first Mach disc (Fig. 50a) are strongly bimodal at $X/D = 0.75$ and have a trimodal structure jet before the shock wave. Immediately downstream of the shock ($X/D = 1.20$, Fig. 50b), the trimodal behavior of the data set is unquestionable. Further downstream, the histograms undergo a transition to bimodal and then unimodal structure as the second shock wave is approached. Similar structure exists in the data obtained at $P_e/P_\infty = 4.0$. The histograms for the unheated jet (Fig. 51) show a unimodal or bimodal structure both upstream and downstream of the Mach disc, while those for the heated flow (Fig. 52), which have much steeper velocity gradients, are unimodal, bimodal, or trimodal at various locations.

Bimodal velocity distributions have previously been noted in LV investigations. Eggers and Jackson (Ref. 43) observed such behavior in the immediate vicinity of a Mach disc and interpreted it to be an indication that the probe volume spanned the shock wave so that measurements were being obtained both upstream and downstream of the shock. This explanation obviously is not satisfactory in the present case since the phenomenon occurs at positions removed from the shock. Durst (Ref. 38) has noted, moreover, that multimodal histograms occur in pulsating flows. For the underexpanded jet, however, the flow field ahead of the initial shock is independent of the pressure ratio so that this possibility must also be rejected.

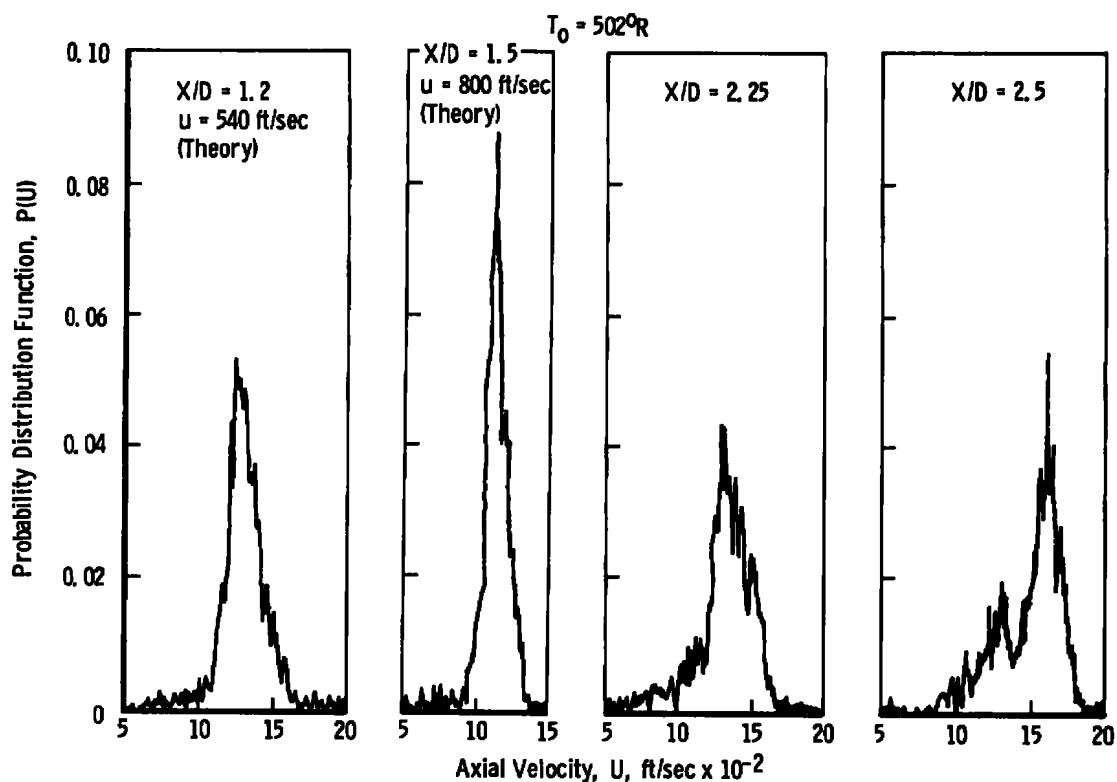
The particle dynamic analysis (Section 3.0) showed that the particle diameter and density control the response of a particle to a prescribed velocity field. One may postulate that if the particles contained in the flow were of two or three distinct types, the histograms would be characterized by velocity ranges in which the probability of detecting a velocity is relatively high compared to other regions. This contention is supported by the data taken at $P_e/P_\infty = 4.0$, where, ahead of the first Mach disc, the

velocity lag $u - U_p$ is nearly invariant when the particle velocity is taken as the mode of the individual peaks of the histogram. For example, in the unheated flow (Figs. 51), the highest velocity mode lags the gas velocity by 4 to 11 percent of the local value determined from pressure measurements, while the next mode occurs at 30 to 35 percent of the gas velocity. Although these observations are consistent with a bimodal size distribution, they are hardly conclusive. In fact, the theoretical results of Section 3.3 which are based on unimodal size and density distributions adequately predict the probability distributions measured at $X/D = 0.25$ (Figs. 51 and 52) so that one must additionally postulate some mechanism through which the particle response distribution becomes time and/or space dependent.

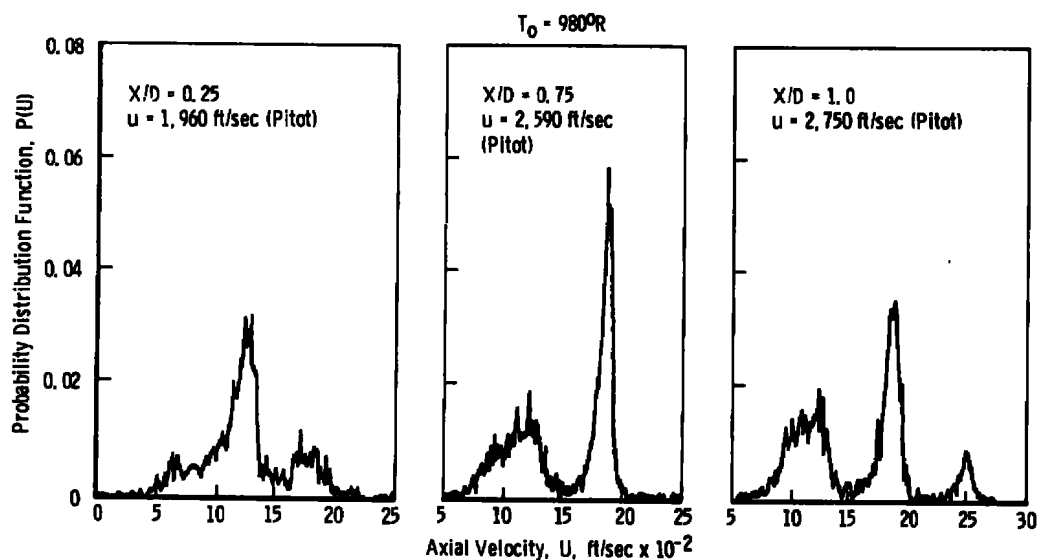


a. Upstream of first Mach disk

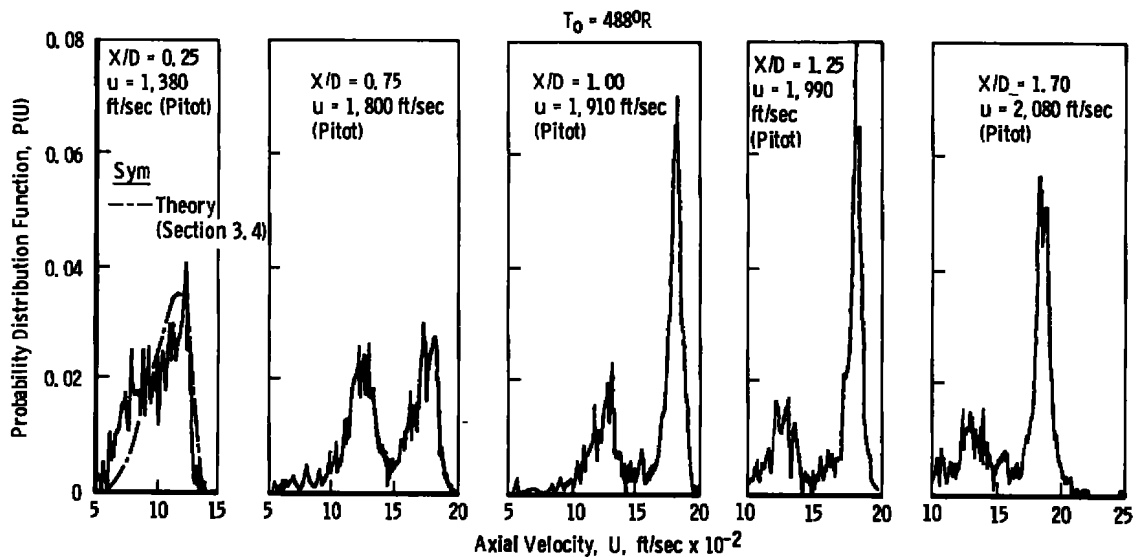
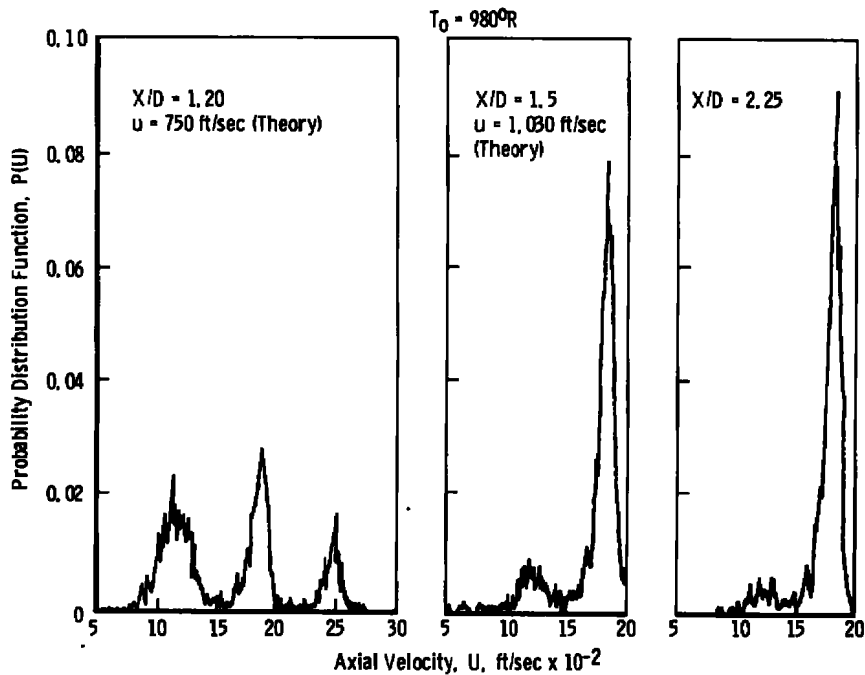
Figure 49. Velocity histograms in the unheated flow,
 $P_0/P_\infty = 2$.

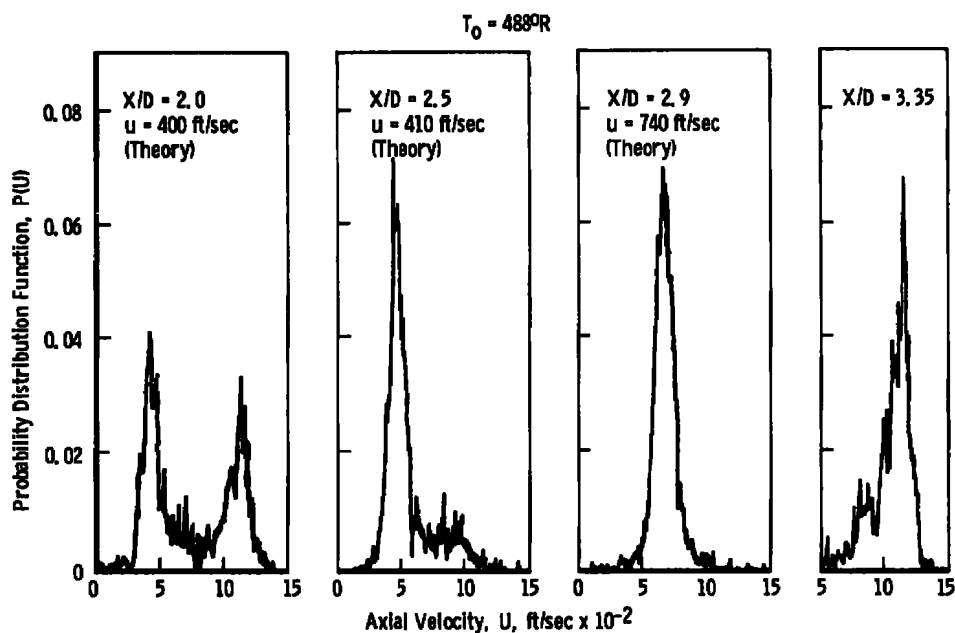


b. Downstream of first Mach disk
 Figure 49. Concluded.

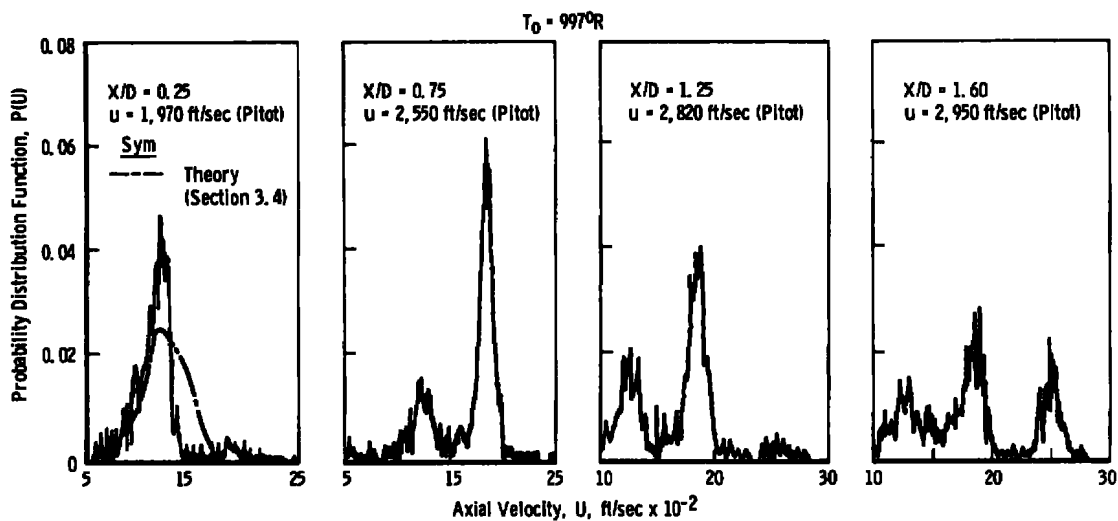


a. Upstream of first Mach disk
 Figure 50. Velocity histograms in the heated flow,
 $P_0/P_{\infty} = 2$.

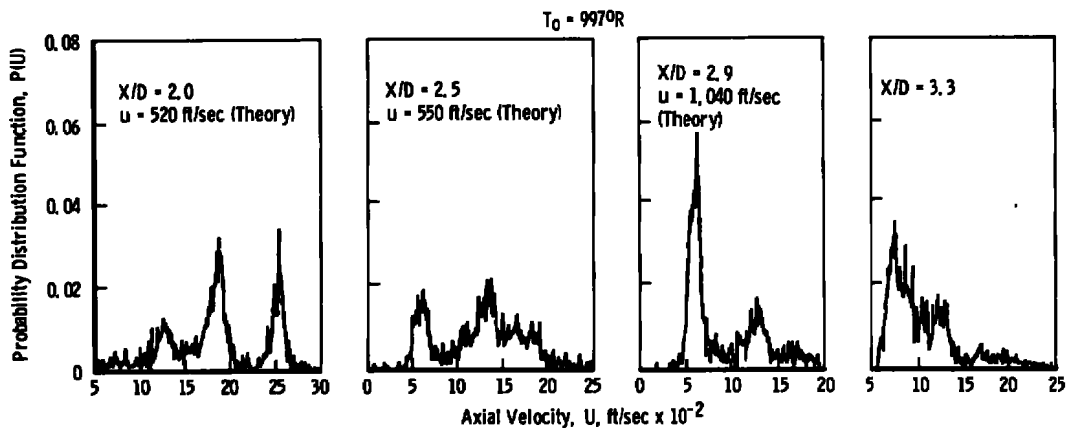




b. Downstream of first Mach disk
Figure 51. Concluded.



a. Upstream of first Mach disk
Figure 52. Velocity histograms in the heated flow,
 $P_0/P_\infty = 4$.



b. Downstream of first Mach disk
Figure 52. Concluded.

One possible process which could lead to spatial or temporal variations in particle size is the condensation of water vapor in the expansion process. Indeed, for the cold jet, this is highly probable. For a specific humidity of 1 grain H_2O/lb air ($-28^\circ F$, dewpoint) and assuming $100^\circ F$ subcooling is required for droplet formation, condensation is possible for $X/D \geq 0.25$. In the heated jet, for the same specific humidity, the vapor pressure of the liquid does not reach the saturation value until $X/D = 0.85$ and does not attain $100^\circ F$ subcooling until $X/D = 1.50$. Both stations are downstream of the point at which the heated jet data exhibit bimodal behavior. It is not possible, therefore, to conclusively attribute the multimodal behavior of the histograms to the existence of distinct particle classes.

402 A second possible explanation for multimodal histograms is that the DDP used in obtaining the data rejected samples in certain frequency (and, hence, velocity) ranges. A series of calibration tests, described in Appendix A, was conducted, and two extremely narrow-band regions (0.1 MHz centered at 19.5 and 32.5 MHz) were found for which a significant fraction of data were rejected. The velocity ranges for which low probability of detection occurred at 1,400 to 1,600 ft/sec (26.6 to 28.3 MHz) and 2,100 to 2,500 ft/sec (32.5 to 35.8 MHz). Since the processor higher dropout frequency coincides with the latter velocity range, further experiments were conducted in an effort to determine if high noise levels could (1) introduce additional ranges where dropout occurred, or (2) increase the bandwidth of the phenomenon. No evidence was found to substantiate either premise even for S/N ratios well below unity. Finally, the experiments at $P_e/P_\infty = 2$ were repeated with a second processor which yielded identical results to those obtained with the first DDP. It is concluded, therefore, that it is highly unlikely that the low values of the velocity probability distribution observed in some velocity ranges were caused by processor malfunction.

403

In Ref. 44, the Doppler ambiguity created by the simultaneous presence of several particles in the probe volume of a reference beam LV was considered. It has generally been assumed that individual realization systems do not obtain such ambiguous results since, ideally, only one particle is present in the probe volume at a given time. For a highly accelerated flow and moderate-to-high particle concentrations, this may be a poor assumption since particles of different sizes may have vastly differing velocities. Accordingly, a particle of diameter (d_1) may leave the stilling chamber at time (t_1) and arrive at the probe volume at the same time as a particle of diameter (d_o) ($d_o > d_1$) which left the plenum at an earlier time (t_o). The frequency of occurrence of such multiple particle interactions would depend on the particle size and density distributions, the flow field, the size of the probe volume, and the location at which the measurements are taken.

While such a study is beyond the scope of the present report, it is instructive to consider the nature of the signals that would result from multiple particle scattering. An analysis of the case where N scatter centers simultaneously occur in the probe volume is presented in Appendix B. For the particular case, $N = 2$, the signal perceived by the PMT would be of the form

$$\begin{aligned}
 I_d = & E_1^2 + E_2^2 + E_1 E_2 + E_1^2 \cos(\omega^* + \omega_{D_1})t + E_2^2 \cos(\omega^* + \omega_{D_2})t \\
 & + 2E_1 E_2 \cos\left(\frac{\omega_{D_1} - \omega_{D_2}}{2} t\right) \cos\left[\left(\omega^* + \frac{\omega_{D_1} + \omega_{D_2}}{2}\right)t\right] \\
 & + E_1 E_2 \cos(\omega_{D_1} - \omega_{D_2})t
 \end{aligned} \quad (60)$$

where E_1 and E_2 are the amplitudes of the electric field vectors corresponding to particles 1 and 2, while ω_{D_1} and ω_{D_2} are the respective Doppler shift frequencies. The signal to be processed, thus, consists of a pedestal voltage given by the first three terms of the equation and a time-varying component characterized by the Doppler frequencies for each particle, a beat frequency $(\omega^* + (\omega_{D_1} + \omega_{D_2})/2)$, and the difference frequencies $(\omega_{D_1} - \omega_{D_2})$ and $(\omega_{D_1} - \omega_{D_2})/2$. In several of the tests reported in this Section, it was noted that LV signal amplitudes increased dramatically (by as much as a factor of five) midway between the nozzle exit plane and primary Mach disc. Concurrent with this observation, it was noted that although the Doppler burst rate was very high (greater than 10^4 bursts/sec) the data acquisition rate was often very low which implies that, in many instances, the LV signal being processed was extremely noisy. Both of these observations are consistent with signals expected from multiple scatter centers since (1) the pedestal voltage increases in proportion to the number of particles contained in the probe volume, and (2) the presence of several time-varying signal components would

appear as noise in the zero-crossing detection of the signal. Most Doppler signals of this type would be rejected by the error rejection logic of the DDP, but since the test procedure required the data acquisition cycle to continue until a predetermined number of samples were obtained, a data set comprised of pure noise would be possible in the limit.

It is difficult to assess which of the frequencies present in the time-varying portion of Eq. (60) would be processed by the DDP. For most of the tests, the difference frequencies for the assumed particle size range would be less than 10 MHz so that these signals would be rejected by the low pass filter of the DDP range used in acquiring the data. The beat frequency, however, has a definite possibility of being processed since its coefficient $(2EE_2 \cos(\omega_{D_1} - \omega_{D_2})t/2)$ would be nearly constant over the time required to process a signal at the frequency $(\omega^* + (\omega_{D_1} + \omega_{D_2})/2)$.

The possibility of detecting beat frequencies is extremely interesting since the theoretical histograms of Fig. 6 show that, for the cold jet, the most probable velocity should occur in the 1,400- to 1,600-ft/sec range. The $X/D > 0.75$ data of Fig. 52, however, show that this velocity range is characterized by low values of the probability distribution which implies that the particle size distribution is radically different than assumed or that signals from particles in the 2- to 4- μm range are being suppressed. The latter situation could occur if particles in this size range were usually detected in combination with a larger or smaller particle and the beat frequency detected or rejected. While this premise is speculative, it must be considered as another possible explanation of the multimodal velocity histograms obtained in this study.

The LV data obtained in the underexpanded jet, therefore, agree with many of the characteristics predicted for the Doppler signals which would occur if multiple particles were present in the probe volume. Similarly, while the preliminary analyses of particle lag effects did not allow the attainment of bimodal velocity distributions, particle dynamic effects also afford a mechanism through which the multimodal behavior could occur. Either explanation emphasizes the difficulty of obtaining accurate LV measurements in naturally seeded flows since the likelihood of the occurrence of either phenomenon would be low if the particle size, density, and concentration were controlled.

6.0 CONCLUSIONS

It has been shown that adequate natural seed material exists in heated jet flows to allow the utilization of a two-component, Bragg-diffracted LV in a backscatter mode. A multiplexing arrangement (Section 2.2) used to ensure simultaneous acquisition of data from both the horizontal and vertical fringe systems proved, moreover, to offer a great improvement over a "master-slave" system used previously (Ref. 12). Simultaneous data

acquisition was not possible, however, at axial velocities exceeding 2,000 ft/sec because the Doppler shift frequencies obtained exceeded the ranges of the present signal separation electronics. The study suggests, additionally, that (on-line) immediate data reduction is desirable in future tests to allow optimization of threshold level settings during an experiment.

On the basis of the results obtained, it is concluded that an LV of the present design can provide only qualitative information on the turbulence structure of naturally seeded flows. The accuracy of the results is dependent on several factors that are related to particle dynamic phenomena rather than the inherent accuracy of the instrument. One fundamental accuracy limitation, discussed in Section 3.0, is particle dynamic broadening of the velocity distributions measured by laser velocimeters. It was shown, that broadening of the data is dependent on the accelerations occurring in the flow field, the sensitivity of the LV to certain particle sizes, and the distribution of particle sizes and densities in the seed material. A second limitation on the accuracy of such LV measurements is the effect of seeding nonuniformities on measurements of radial velocities and turbulence intensities in jet flows. It was also inferred that lack of control over the seed material concentration in the flow can lead to either multiple particle scattering from the probe volume when the seed concentration is high or intolerably long data acquisition times when the seed concentration is low. All of the above effects can be minimized or eliminated with a properly designed seeding system. With such a system, the major source of error in LV measurements of gas velocities would be due to the limitations of the selected particle to follow the flow and the fundamental limitations of the system electronics.

In applications where seeding is not feasible, a reasonably accurate method for estimating mean velocities in accelerating flows is to define the mean velocity as the limiting velocity measured by the LV (Section 5.1). The use of this technique, however, requires knowledge of whether the flow is accelerating, positively or negatively, and its accuracy is affected by turbulence and system noise.

Two electronic modifications to the present LV were also suggested by the results as being of potential value in naturally seeded flows. These are the use of upper threshold detectors to limit the data obtained to particles whose diameters are less than a limiting value (Ref. 36) and the particle sizing interferometer (Ref. 37) to simultaneously measure particle size and velocity.

Finally, it is noted that the analysis presented for particle dynamic broadening of LV data may be effectively inverted to yield the size or density distribution of particles in a rapidly accelerating flow field. The use of this technique, however, requires low turbulence levels and knowledge of the gas velocity in the flow.

REFERENCES

1. Bradshaw, P. An Introduction to Turbulence and Its Measurement. Pergamon Press, New York, 1971.
2. Stevenson, W. H. and Thompson, H. D., Editors. "The Use of the Laser Doppler Velocimeter for Flow Measurements." Project SQUID Report, Jet Propulsion Center, Purdue University, West Lafayette, Indiana, November 1972.
3. McLaughlin, D. and Tiederman, W. G., Co-Directors. "Theory and Application of the Laser Doppler Anemometer." Oklahoma State University Laser Doppler Anemometer Workshop, Oklahoma State University, Stillwater, Oklahoma, June 1973.
4. Stevenson, W. H. and Thompson, H. D., Editors. Proceedings of the Second International Workshop on Laser Velocimetry. Engineering Experiment Station Bulletin No. 144, Purdue University, West Lafayette, Indiana, March 1974.
5. Eckert, E.R.G., editor. Minnesota Symposium on Laser Anemometry, Proceedings. "University of Minnesota, Minneapolis, October 1975.
6. Rudd, M. J. "A Self Aligning Laser Doppler Velocimeter." Optical Instruments and Techniques. 1969, pp. 158-166.
7. Lennert, A. E., Brayton, D. B., and Crosswy, F. L. "Summary Report of the Development of a Laser Velocimeter to be used in AEDC Wind Tunnels." AEDC-TR-70-101 (AD871321), July 1970.
8. Brayton, D. B., Kalb, H. T., and Crosswy, F. L. "A Two-Component[†] Dual-Scatter Laser Doppler Velocimeter with Frequency Burst Signal Readout." Applied Optics, Vol. 12, No. 6, June 1973, pp. 1145-1156.
9. Asher, J. A. "Laser Doppler Velocimeter System Development and Testing." General Electric Technical Information Series Report No. 72CRD295, Corporate Research & Development Distribution, Schenectady, N. Y., October 1972.
10. Crosswy, F. L. and Hornkohl, J. O. "Signal-Conditioning Electronics for a Vector Velocity Laser Velocimeter." AEDC-TR-72-192 (AD755842), February 1973.
11. Barnett, D. O. and Giel, T. V., Jr. "Application of a Two-Component, Bragg-Diffracted LV to Turbulence Parameter Determination in an Isothermal, Subsonic Jet." pp 146-183 of Ref. 5.

12. Barnett, D. O. and Giel, T. V., Jr. "Application of a Two-Component, Bragg-Diffracted Laser Velocimeter to Turbulence Measurements in a Subsonic Jet." AEDC-TR-76-36 (ADA025355), May 1976.
13. Cline, V. A. and Bentley, H. T., III. "Application of a Dual-Beam Laser Velocimeter to Turbulent Flow Measurements." AEDC-TR-74-56 (AD785352) September 1974.
14. Abernethy, R. B., et al., Pratt and Whitney Aircraft, and Thompson, J. W., Jr., ARO, Inc. "Handbook of Uncertainty in Gas Turbine Measurements." AEDC-TR-73-5 (AD755356), February 1973.
15. Barnett, D. O. and Bentley, H. T., III. "Statistical Bias of Individual Realization Laser Velocimeters." Proceedings of the Second International Workshop on Laser Velocimetry, Engineering Experiment Station, Bulletin No. 144, Purdue University, West Lafayette, Indiana, March 1974.
16. Hinze, J. O. Turbulence. McGraw-Hill, New York, 1957.
17. Berman, N. S. "Particle-Fluid Interaction Corrections for Flows Measurements with a Laser Doppler Flowmeter." NASA-CR-124254, 1972.
18. von Stein, H. D. and Pfeifer, H. J. "Investigation of the Velocity Relaxation of Micron-Sized Particles in Shock Waves Using Laser Radiation." Applied Optics, Vol. 11, No. 2, 1972, pp. 305-307.
19. Maxwell, B. R. and Seasholtz, R. G. "Velocity Lag of Solid Particles in Oscillating Gases and in Gases Passing through Normal Shock Waves." NASA TND-7490, 1974.
20. Hsieh, T. "Analysis of Velocity Measurements about a Hemisphere-Cylinder Using a Laser Velocimeter." Journal of Spacecraft and Rockets.
21. Cadle, R. D. Particles in the Atmosphere and Space, Reinhold, New York, 1966.
22. Fennelly, P. F. "The Origin and Influence of Airborne Particulates." American Scientist, Vol. 64, January - February, 1976, pp. 46-56.
23. Langmuir, I. and Blodgett, K. B. "A Mathematical Investigation of Water Droplet Trajectories." Army Air Force Technical Report No. 5418, February 1946.
24. Sami, S. "Velocity and Pressure Fields in a Diffusing Jet." Ph.D. Dissertation, University of Iowa, 1966.

25. Wagnanski, I. and Fiedler, H. "Some Measurements in the Self-Preserving Jet." Journal Fluid Mechanics, Vol. 38, Part 3, 1969, pp. 517-612.
26. Fox, J. H., "On the Structure of Jet Plumes." AIAA Journal, Vol. 12, No. 1, Jan. 1974, pp. 105-107.
27. Bendat, J. S. and Piersol, A. G. Measurements and Analysis of Random Data. John Wiley and Sons, Inc., New York, 1966.
28. Farmer, W. M. and Brayton, D. B. "Analysis of Atmospheric Laser Doppler Velocimeters." Applied Optics, Vol. 10, No. 10, October 1971, pp. 2319-2321.
29. Brayton, D. B. "An Analysis of the Data Acquisition Rate of an Atmosphere Backscatter Laser Doppler Velocimeter." Presented in Ref. 2.
30. Farmer, W. M. "The Interferometric Observation of Dynamic Particle Size, Velocity, and Number Density." Ph.D. Dissertation, University of Tennessee, 1973.
31. Love, T. J. "A Simplified Scheme for Estimates of Light Scattered by a Single Particle in the Design of Detector Geometry for LV Applications." Presented in Ref. 3.
32. Wells, H. S. "Results of the AEDC/VKF Airflow Contamination Investigation: Assessment of Particulate Contamination Characteristics and Turbine Engine Ingestion Effects." AEDC-TR-77-13.
33. Melling, A. "Scattering Particles - Specification." Lecture notes from International Short Course on Laser Velocimetry, Purdue University, March 1974.
34. Lo, C. F. "Transonic Flow Field Measurements Using a Laser Velocimeter." Proceedings of Minnesota Symposium on Laser Anemometry, University of Minnesota, Minneapolis, October 1975.
35. Cline, V. C. and Lo, C. F. "Application of Dual-Scatter LV in Transonic Flow Research." Proceedings of AGARD Symposium on Non-Obtrusive Instrumentation Techniques, May, 1976.
36. Pfeifer, H. J. "A Method for Recognition of Big Particles." ISL-Report 37/73, 1973.
37. Roberds, D. W. "Electronic Instrument for Interferometric Particle Sizing." Ph.D. Dissertation, University of Tennessee, Knoxville, December 1975.

- 38. Durst, F. "Application of Laser Doppler Anemometers in Gas and Liquid Flows." Lecture notes from International Short Course on Laser Velocimetry, Purdue University, March 1974.
39. Webber, D. P. "Turbulent Velocity Field Structure in a Round Jet and its Relation to Fluctuating Pressure Fields." Ph.D. Dissertation, Nuclear Engineering Program, University of Illinois, Urbana, Illinois, 1974.
40. Corrsin, S. and Uberoi, M. S. "Further Experiments on the Flow and Heat Transfer in a Heated Turbulent Air Jet." NACA-TN-1865, April 1949.
- 41: Rouse, H., Editor. Advanced Mechanics of Fluids. John Wiley and Sons, Inc., New York, 1963.
42. Love, E. S., Grigsby, C. E., Lee, L. P., and Woodling, M. J. "Experimental and Theoretical Studies of Axisymmetric Free Jets." NASA-TR-R-6, 1959.
- 43. Eggins, P. L. and Jackson, D. A. "Laser-Doppler Velocity Measurements in an Underexpanded Free Jet." Journal Physics D:Applied Physics, Vol. 7, pp 1894-1906, 1974.
44. George, W. K. and Lumley, J. L. "The Laser Doppler Velocimeter and Its Application to the Measurement of Turbulence." Journal Fluid Mechanics, Vol. 60, Part 2, 1973, pp. 321-362.

APPENDIX A

LIMITS ON THE ACCURACY OF THE MODEL 8 DATA PROCESSOR

Some LV data obtained in the studies of an underexpanded free jet (Section 5.0) exhibited histograms typified by a low probability of occurrence of certain velocities. While this behavior could be explained by particle lag effects, the possibility was also considered that the AEDC-developed Model 8 Doppler Data Processor (DDP) was rejecting signals in certain frequency ranges. In studying the latter possibility, experiments were conducted which give some insight into the accuracy of this instrument.

To test the data acceptance characteristics of each processor, a sweep signal generator was used in conjunction with a ramp function generator to provide a continuous sinusoidal signal having a frequency that varied linearly in time. A pulse generator was used to simulate a 1- μ sec-duration A-gate pulse which caused the processor to sample the input signal each millisecond. The frequency measured by the DDP for each sample was then stored in an HP 2100 minicomputer for later analysis. A diagram of the instrumentation and the frequency-time variation is shown in Fig. A-1 where F_1 and F_2 correspond to the lower and upper frequency limits of the processor range under investigation.

If data from such an experiment are presented in the form of a frequency histogram, the number of samples (δN_i) to be found in each bin of width (δf_i) is given by the relation:

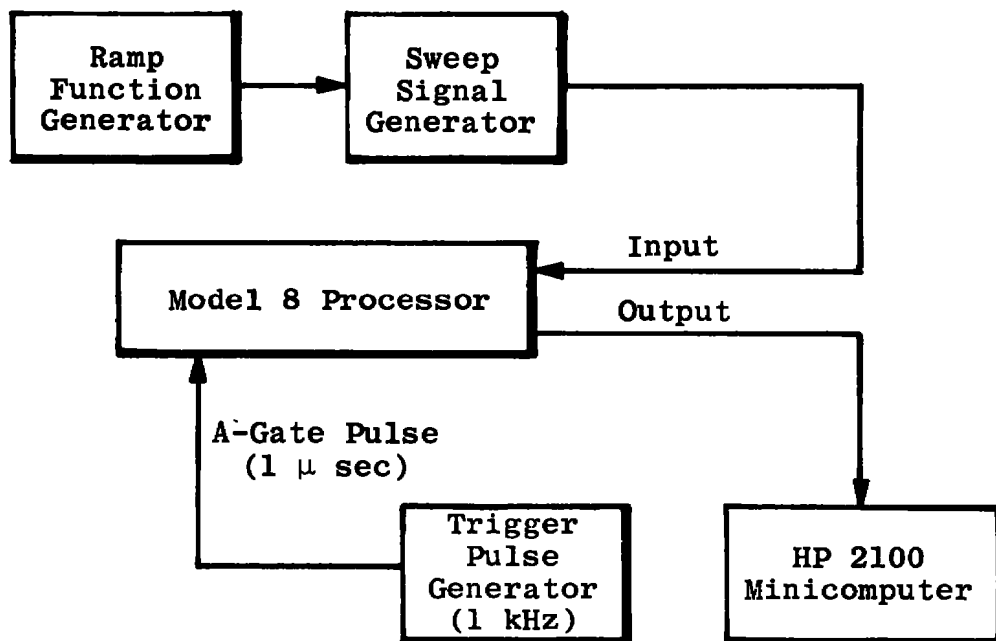
$$\delta N_i = N \frac{\delta f_i}{F_2 - F_1} \quad (A-1)$$

where N is the total number of samples in the data set. It should be noted that if the bin width is a constant (δf) the number of samples in each bin will also be constant since from Eq. (A-1)

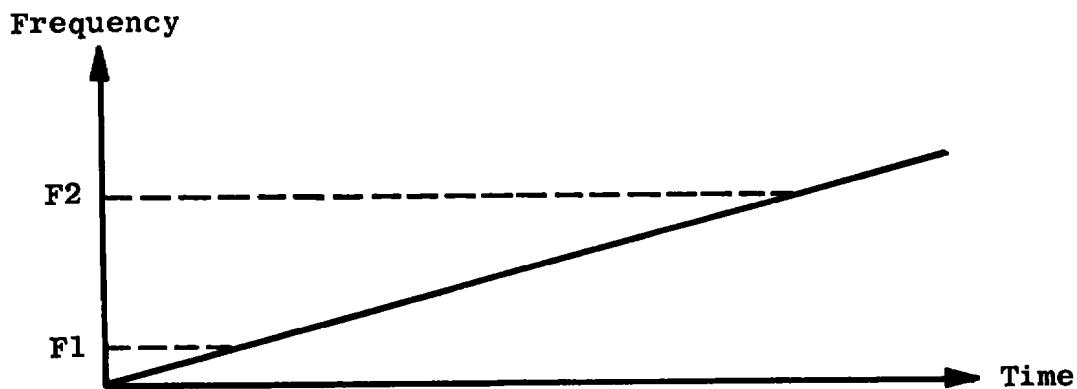
$$\delta N = N \frac{\delta f}{F_2 - F_1} \quad (A-2)$$

These relations may be used, moreover, to evaluate the round-off error of a given processor if it is assumed that such errors are simply manifested as contractions or expansions of the bin width. Accordingly for a round-off error ($\pm \epsilon$) in the measured period (τ), it may be shown that the apparent bin width is

$$\delta f_i = \frac{\delta f \pm 2\epsilon f_1 f_2}{1 \mp \epsilon [\delta f = \epsilon f_1 f_2]} \quad (A-3)$$



a. Instrumentation schematic



b. Input signal frequency history
Figure A-1. Calibration test instrumentation.

where f_1 and f_2 are the prescribed lower and upper frequencies of a bin of width

$$\delta f = f_2 - f_1$$

Then from Eqs. (A-1), (A-2), and (A-3), the permissible variation in the observed number of samples in a given bin of the histogram due to a round-off error (ϵ) is

$$\delta N_i = \delta N \left[\frac{1 \pm 2\epsilon \frac{f_1 f_2}{\delta f}}{1 \mp \epsilon (\delta f \pm \epsilon f_1 f_2)} \right] \quad (A-4)$$

It may be concluded from these relations that an experiment such as that described will, for constant prescribed bin width, yield a uniform distribution of samples as predicted by Eq. (A-2) unless there is a round-off error. In that case, the number of samples observed must be within the bounds given by Eq. (A-4). Any variations outside these limits are due to a malfunction of the processor or experimental inaccuracy.

In Figs. A-2 through A-4, the histograms obtained for DDP 1, which was used to measure axial velocities in the free-jet studies, are presented for three frequency ranges of the processor. It is seen from Fig. A-2 that all data from the calibration tests for the 0.1- to 0.5-MHz range fall within the tolerance limits given by Eq. (A-4) for an uncertainty of $\epsilon = \pm 0.5$ nsec. Since the resolution of the processor in this range is 1 nsec, it is concluded that the variation in the number of samples observed in each bin is due to the 1-nsec resolution limit. For the 4- to 20- and 10- to 50-MHz ranges, the Model 8 DDP employs a 100:1 pulse stretcher which increases the resolution of the instrument to 0.01 nsec. Figures A-3 and A-4 show that the variation in the observed samples in each bin of the histograms lie within ± 0.005 -nsec tolerance bands so that, again, DDP 1 has an accuracy comparable to its resolution limit. It is noted, incidentally, that the high pass filter for the 4- to 20-MHz range has a 4.2-MHz cutoff rather than the specified 4.0 value.

The results of calibration tests on DDP 2, which was used for measuring vertical velocities and to spot check results for DDP 1, are shown in Figs. A-5 through A-7. As for the first processor, the results for the 0.1- to 0.5-MHz processing range (Fig. A-5) lie within the ± 0.5 -nsec tolerance limits, thus indicating that the processor accuracy is set by its resolution limit (1 nsec). In the pulse stretched ranges (Figs. A-6 and A-7), however, DDP 2 is less accurate with the data lying within a ± 0.05 -nsec tolerance band. It must be concluded then that DDP 2 only has a capability of resolving signal periods to 0.1 nsec. In an effort to determine the cause of the different levels of accuracy for apparently identical units, a number of system checks were performed. Replacement of pulse stretcher and emitter-coupled-logic (ECL) circuit boards, as well as utilization of a

redesigned transmission line between the ECL board and zero-crossing detector, had no significant effect on the histograms obtained for DDP 2. It is noted, however, that the 0.1-nsec uncertainty is less than the rise and fall time of the logic gates on the ECL board so that any irregularities in logic waveforms caused by internal reflections could induce the results obtained.

In performing these calibration tests, the histograms were found to be highly repeatable with respect to the number of samples observed in a given histogram bin which suggests that the round-off errors are not truly random and may be eliminated or reduced during data reduction. No attempt was made, however, to randomize the calibration experiments so that this finding may be a consequence of the test procedure.

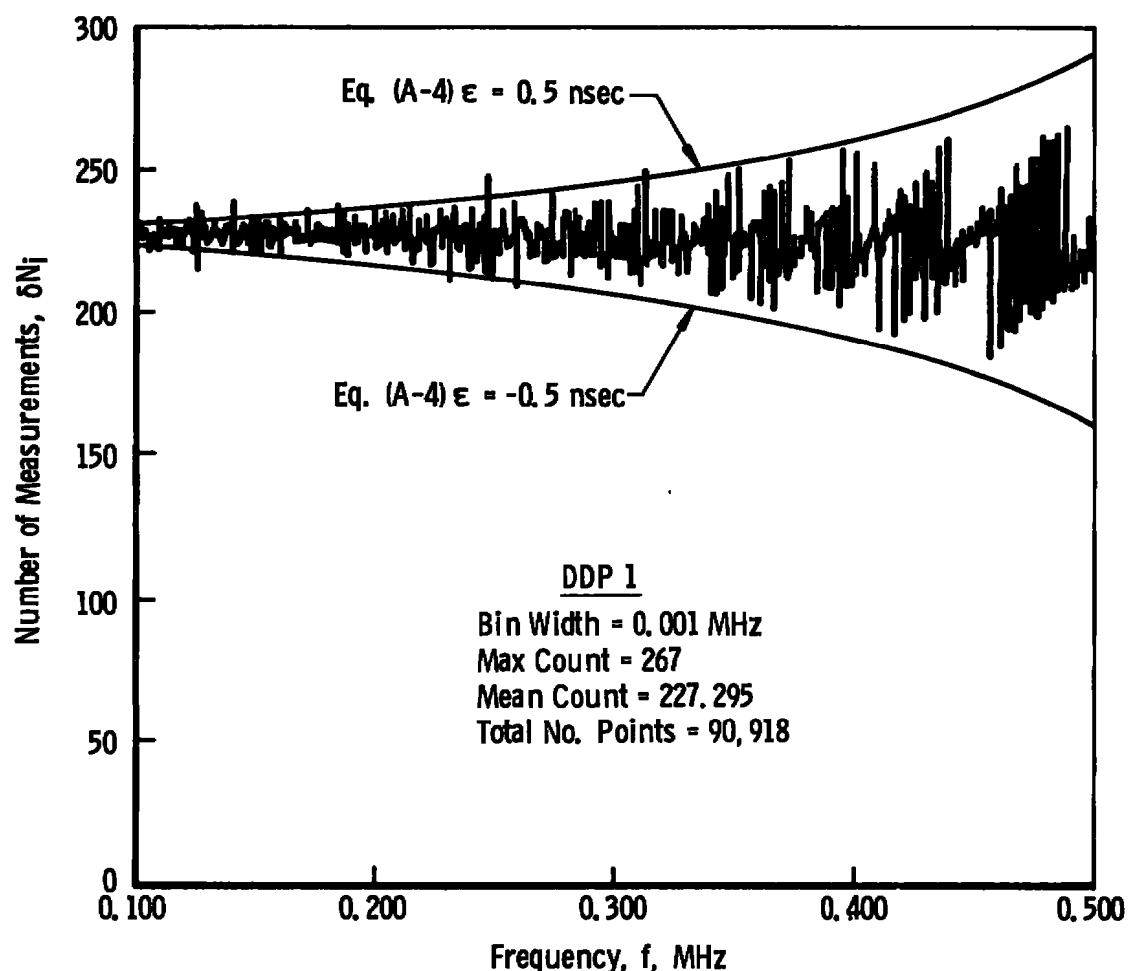


Figure A-2. Frequency histogram for axial processor, 0.1 to 0.5 MHz.

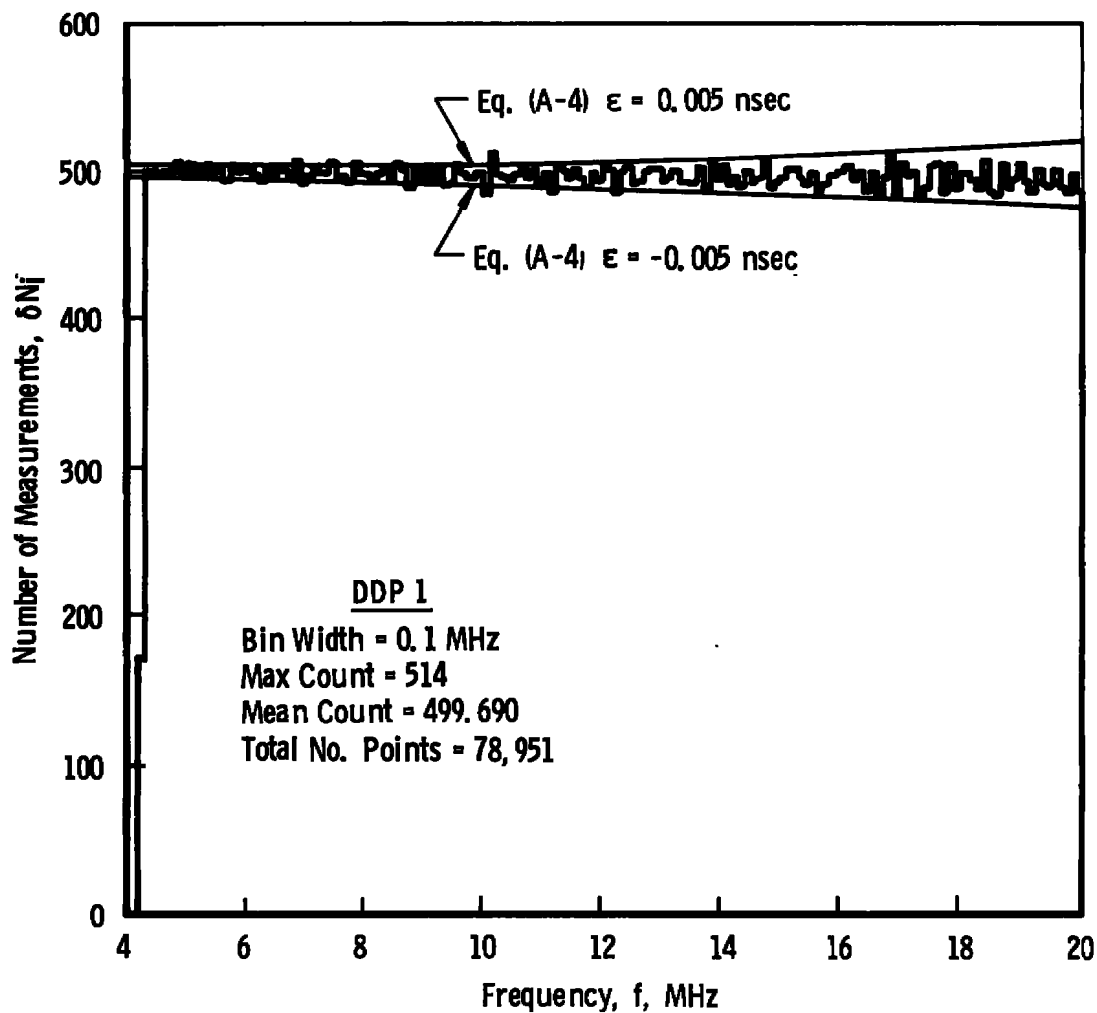


Figure A-3. Frequency histogram for axial processor,
4 to 20 MHz.

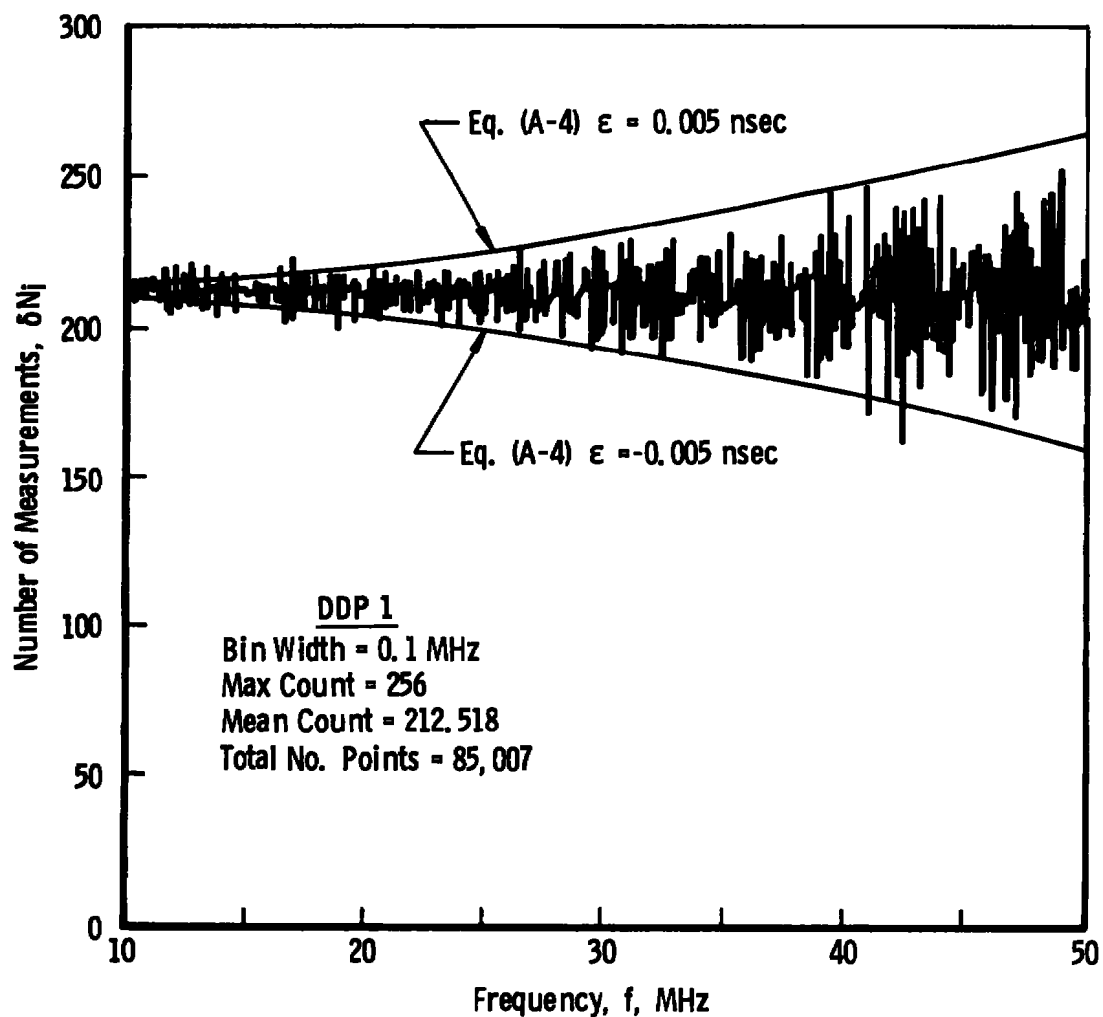


Figure A-4. Frequency histogram for axial processor, 10 to 50 MHz.

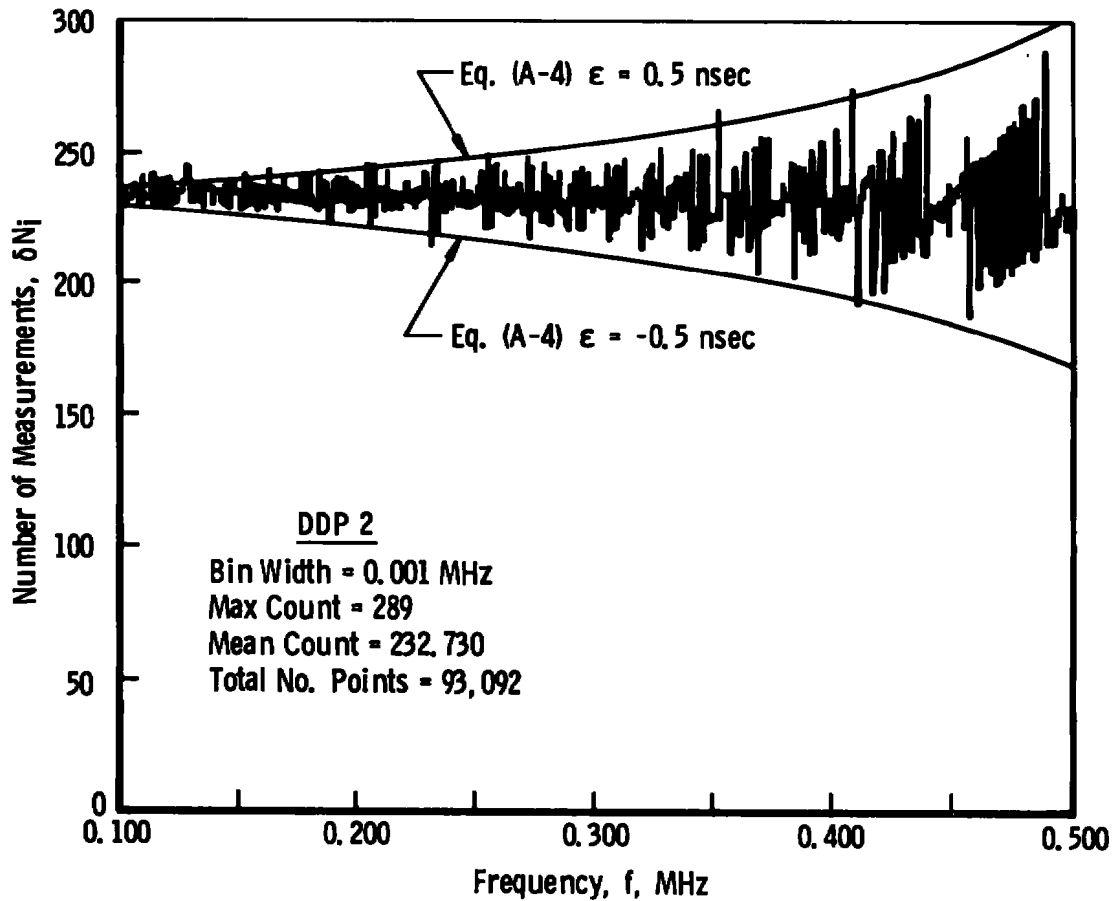


Figure A-5. Frequency histogram for vertical processor, 0.1 to 0.5 MHz.

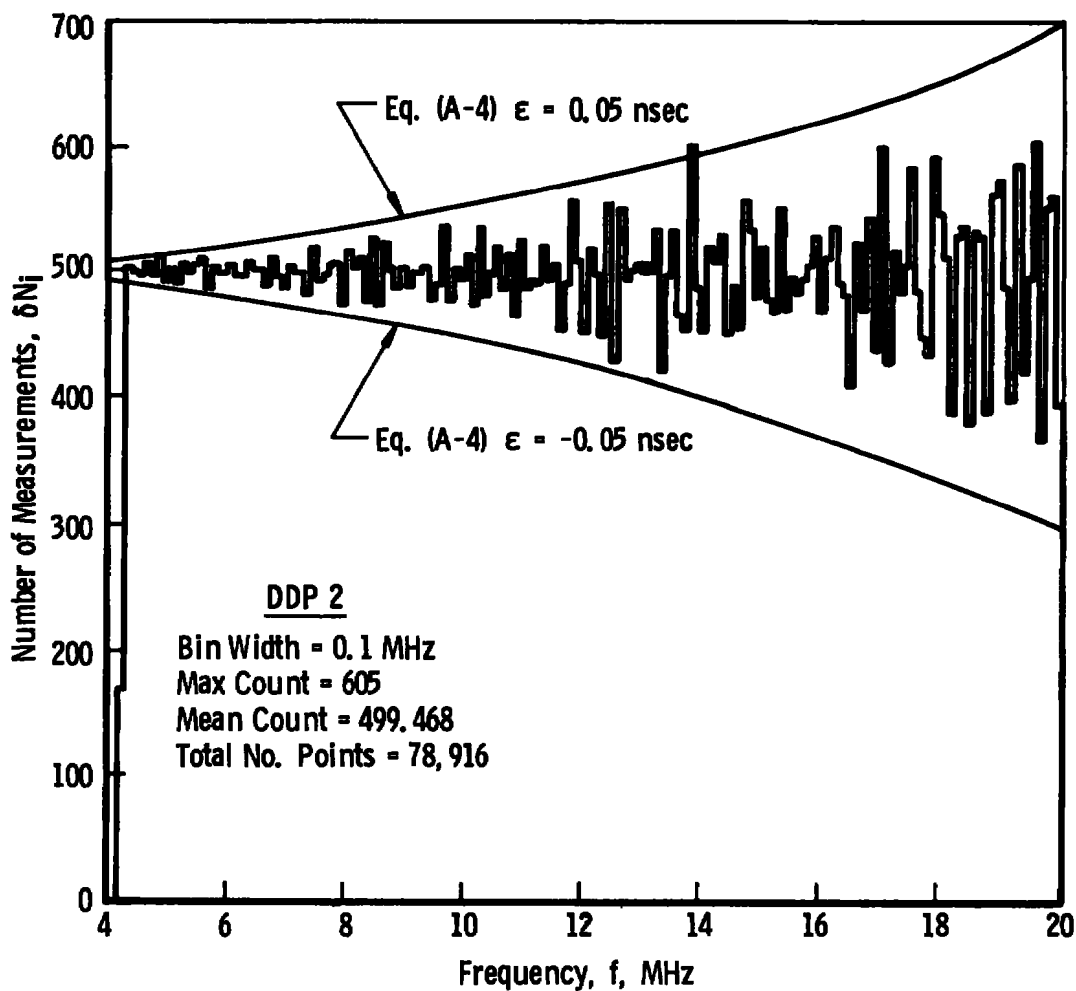


Figure A-6. Frequency histogram for vertical processor, 4 to 20 MHz.

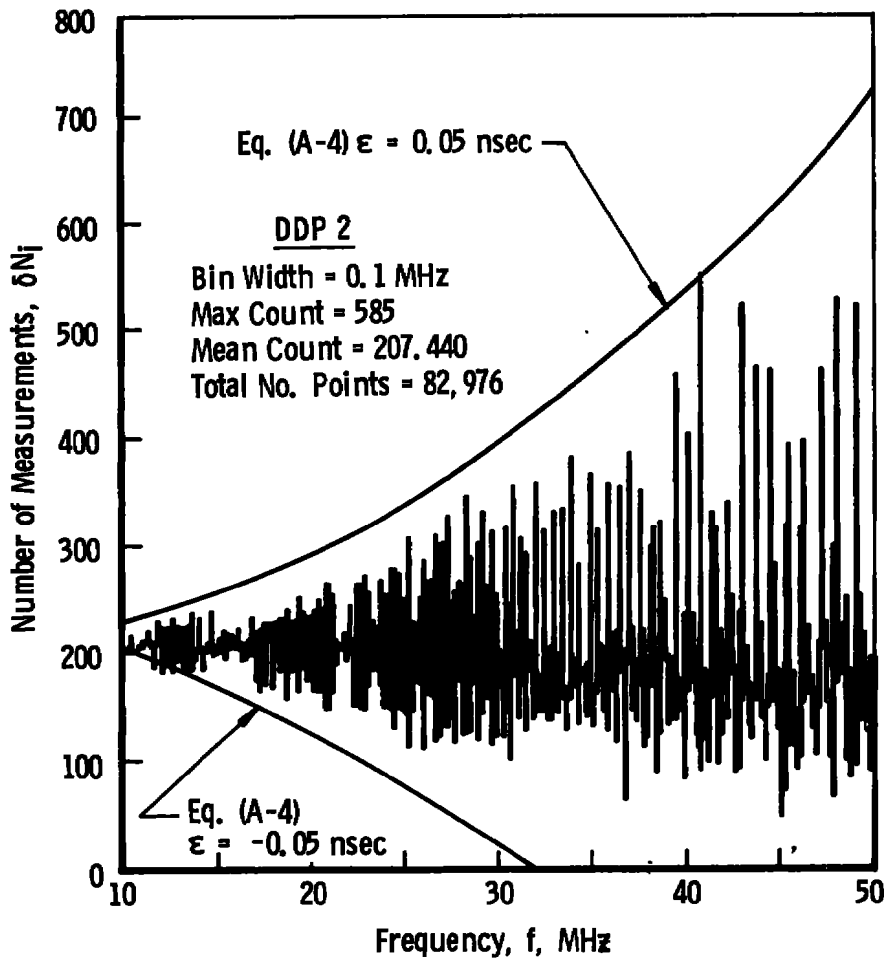


Figure A-7. Frequency histogram for vertical processor, 10 to 50 MHz.

APPENDIX B

MULTIPLE PARTICLE SIGNAL ANALYSIS

Consider $2N$, parallel electromagnetic waves that are so aligned that they impinge normally on an optical homodyne detector. The total electric field vector is given by

$$E_T = \sum_{i=1}^{2N} E_i \cos(\omega_i t) \quad (B-1)$$

where E_i is the amplitude of an individual wave and ω_i is its frequency. If each electric field has the same polarization, the intensity of the radiation to which the photomultiplier responds would be the square of the electric field which is given by

$$E_T^2 = \sum_{i=1}^{2N} E_i^2 \cos^2(\omega_i t) + \sum_{i=1}^{2N-1} \sum_{j=i+1}^{2N} E_i E_j \cos[(\omega_i + \omega_j) t] + \sum_{i=1}^{2N-1} \sum_{j=i+1}^{2N} E_i E_j \cos[(\omega_i - \omega_j) t] \quad (B-2)$$

The detector will, in general, have the capability of responding to the different frequencies between incoming waves but will not respond to the instantaneous value of signals at optical frequencies (Ref. 7). The first two terms of Eq. (B-2) will, therefore, only contribute their average value to the photodetected signal. Performing the indicated averages, one obtains the detector response as

$$I_d = \frac{1}{2} \sum_{i=1}^{2N} E_i^2 + \sum_{i=1}^{2N-1} \sum_{j=i+1}^{2N} E_i E_j \cos[(\omega_i - \omega_j) t] \quad (B-3)$$

Now each pair of waves ($E_{2k-1} \cos(\omega_{2k-1} t)$ and $E_{2k} \cos(\omega_{2k} t)$) where $k = 1, 2, \dots, N$ corresponds to the light scattered by one of N scatter centers. If the diameter of these particles is much less than the fringe spacing and paraxial scattering is assumed, the amplitude of the waves may be approximated by $E_{2k-1} = E_{2k}$. By using this assumption and the identity,

$$\cos A + \cos B = 2 \cos \frac{A+B}{2} \cos \frac{A-B}{2} \quad (B-4)$$

allows Eq. (B-3) to be rewritten as

$$\begin{aligned}
 I_d = & \sum_{k=1}^N E_{2k-1}^2 + \sum_{k=1}^N E_{2k-1}^2 \cos(\omega_{2k-1} - \omega_{2k})t \\
 & + 2 \sum_{k=1}^{N-1} \sum_{s=k+1}^N E_{2k-1} E_{2s-1} \cos \left[\frac{(\omega_{2k-1} + \omega_{2k}) - (\omega_{2s-1} + \omega_{2s})}{2} t \right] \\
 & \times \cos \left[\frac{(\omega_{2k-1} - \omega_{2k}) + (\omega_{2s-1} - \omega_{2s})}{2} t \right] \\
 & \times \cos \left[\frac{(\omega_{2k-1} - \omega_{2k}) - (\omega_{2s-1} - \omega_{2s})}{2} t \right]
 \end{aligned} \tag{B-5}$$

It is noted that

$$\omega_{2r-1} - \omega_{2r} = \omega^* + \omega_{D_r} \tag{B-6}$$

and

$$\omega_{2r-1} + \omega_{2r} = 2\omega_o + \omega^* + \omega_{D_r} \tag{B-7}$$

where ω^* is a frequency shift imparted by the Bragg cell, ω_{D_r} is the Doppler shift for the r^{th} particle, and ω_o is the frequency of the incident radiation. Substituting Eq. (B-6) and Eq. (B-7) into Eq. (B-5) gives

$$\begin{aligned}
 I_d = & \sum_{r=1}^N E_r^2 + \sum_{r=1}^N E_r^2 \cos(\omega^* + \omega_{D_r})t + 2 \sum_{r=1}^{N-1} \sum_{s=r+1}^N E_r E_s \cos^2 \left[\frac{\omega_{D_r} - \omega_{D_s}}{2} t \right] \\
 & + 2 \sum_{r=1}^{N-1} \sum_{s=r+1}^N E_r E_s \cos \left(\frac{\omega_{D_r} - \omega_{D_s}}{2} t \right) \cos \left(\omega^* + \frac{\omega_{D_r} + \omega_{D_s}}{2} t \right)
 \end{aligned} \tag{B-8}$$

Since

$$\cos A \cos B = 1/2 [\cos(A+B) + \cos(A-B)] \tag{B-9}$$

Eq. (B-8) may be rewritten

$$\begin{aligned}
 I_d = & \sum_{r=1}^N E_r^2 + \sum_{r=1}^{N-1} \sum_{s=r+1}^N E_r E_s + \sum_{r=1}^N E_r^2 \cos \left[(\omega^* + \omega_{D_r}) t \right] \\
 & + \sum_{r=1}^{N-1} \sum_{s=r+1}^N E_r E_s \cos \left[(\omega_{D_r} - \omega_{D_s}) t \right] \\
 & + 2 \sum_{r=1}^{N-1} \sum_{s=r+1}^N E_r E_s \cos \left[\left(\frac{\omega_{D_r} - \omega_{D_s}}{2} \right) t \right] \cos \left[\left(\omega^* + \frac{\omega_{D_r} + \omega_{D_s}}{2} \right) t \right]
 \end{aligned} \tag{B-10}$$

The signal is seen to be composed of a pedestal given by the first two summations and a time-dependent function containing the Doppler frequencies of the individual particles $(\omega^* + \omega_{D_r})$, the beat frequencies $(\omega^* + (\omega_{D_r} + \omega_{D_s})/2)$, and the difference frequencies $(\omega_{D_r} - \omega_{D_s})$.

NOMENCLATURE

A	Area, ft^2 ; coefficient, Eq. (40)
C_D	Drag coefficient, Eq. (21)
$C()$	Cummulative distribution function, C.D.F.; Eq. (39)
c_p	Specific heat at constant pressure, $\text{Bru/lb-}^\circ\text{R}$
D	Nozzle exit diameter, $2 r_e$, ft
d_p	Particle diameter, μm
E	Electric field vector amplitude, Eq. (60)
e	Constant irrational number, 2.71828...
F_i	Limiting frequencies of processor ranges, Appendix A
f	Frequency, Hz
$f()$	Probability density function (p.d.f.), Section 3.0
G	Gain, Eq. (32)
g	Acceleration of gravity, ft/sec^2
$g(), g_i$	Mie scattering function, Eq. (33)
h	Planck's constant, 6.63×10^{-39} joule-sec
I_d	Intensity of light collected by PM tube (Section 5.0)
K_U, K_V	Fringe spacing, $\text{ft} \times 10^{-6}$
M	Mach number; total number of samples comprising a data point
m	Number of samples in intervals $U \pm 1/2 \Delta U$; exponent Eq. (40)
N	Particle concentration, ft^{-3}
n	Index of refraction; number
P	Pressure, lb/ft^2 , or power, w

$P()$	Probability distribution function, P.D.F., Section 3.0
$P_D(d_p)$	LV detection P.D.F., Eq. (38)
$P_N(d_p)$	Particle Size P.D.F., Eq. (41)
$P_{ND}(d_p)$	Joint Probability Function, Eq. (42)
$Q(), Q_i$	Particle scattering efficiency
Re	Reynolds number
r	Radial measure, ft
\vec{r}	Position vector, ft, Section 3.0
T_o	Jet total temperature, °R
t	Time, sec
U	Axial velocity component, ft/sec
\bar{u}	Measured mean velocity, ft/sec (Section 3.5)
$\langle u \rangle$	Actual mean velocity, ft/sec (Section 3.5)
U^*	Reference velocity (axial component), ft/sec
u	Axial mean velocity component, ft/sec
u'	Axial fluctuating velocity component, ft/sec
$\overline{u'v'}$	Shear stress correlation
V	Visibility function; vertical or radial velocity component, ft/sec
\vec{V}	Velocity vector, ft/sec, Section 3.0
v	Vertical or radial mean velocity component, ft/sec
v'	Vertical or radial fluctuating velocity component, ft/sec
W	Tangential velocity component, ft/sec
w	Tangential mean velocity component, ft/sec

w'	Tangential fluctuating velocity component, ft/sec
X	Axial location, ft
(α, β, γ)	Error coefficients, Eq. (1)
γ	Ratio of specific heats; particle response parameter, Eq. (13)
Δ	Uncertainty or increment
δ	Indicates small or infinitesimal change; LV fringe spacing, μm
ϵ	Round-off error
η	PM tube quantum efficiency; dimensionless location Eq. (58), velocity ratio (Section 3.4)
θ	Probe volume convergence angle
θ_0	Temperature difference ($T_0 - T_\infty$), $^\circ\text{R}$
Λ	Constant, Eq. (59)
λ	Wavelength of incident light, 514.5 nm
μ	Fluid viscosity, lb/ft-sec
ν	Kinematic viscosity, ft^2/sec
ξ	Particle concentration ratio, Eq. (48)
ρ	Density, lb/ft^3
σ	Scattering cross section of particles, ft^2 , local turbulence intensity
τ	Period of Doppler frequency, sec; Reynolds stress, Table 3
ϕ	Solid scattering angle; fringe orientation angle, Section 2.7
ψ	Fringe orientation angle, Section 2.7
χ_i	Parameter, $\pi d_{p_i}/\delta$
ω	Frequency, rad/sec

SUBSCRIPTS

D	Based on nozzle exit diameter; Doppler shift; detection probability
e	Exit conditions
(i, j, k)	Individual indices
L	Laser parameter
m	Along measurement axis
min	Minimum
N	Particle size probability
o	Referenced to oscillator; or total conditions, or incident conditions
p	Particle
(r,s)	Indices
U,V	Pertaining to axial or verticle measurement
1, 2	Limiting values; or values from a particular stream; upstream and downstream of shock
∞	Ambient conditions

SUPERSCRIPT

*	Throat or reference condition
----------	-------------------------------